Numerical modelling of remanence carriers and remanence acquisition in marine sediments

Dissertation
zur Erlangung des Doktorgrades
am Fachbereich Geowissenschaften
der Universität Bremen

vorgelegt von
Anne Witt
Bremen, Mai 2005

Contents

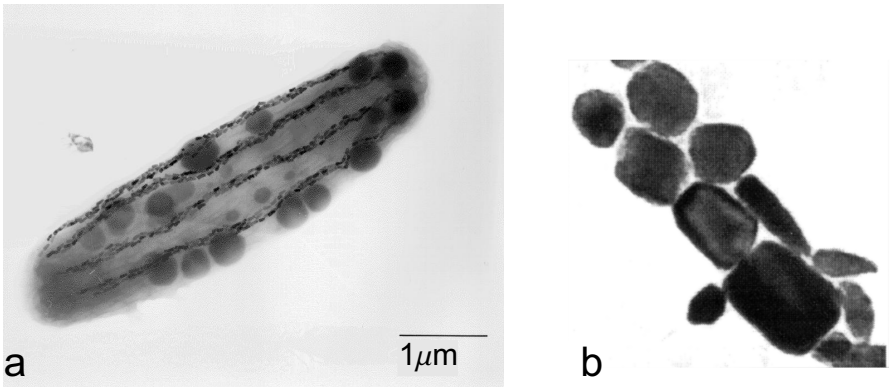

Figure 1: Magnetotactic bacteria produce magnetite particles which are used to navigate through the water column. Different bacteria generate different shapes of magnetite particles which are deposited in the sediment after the bacteria dies ((a) Hanzlik (1999), (b) Petermann (1994)).

Introduction

Sediments, sedimentary rocks and lava flows act as recording media for changes in the earth's magnetic field. Ocean sediments with a high deposition rate are used to study recent reversals of the earth's magnetic field. Highly resolved paleomagnetic records from these sediments give detailed insight into secular variations and excursions of the earth's magnetic field which in turn provide information about the geodynamo. Records which date back more than 175 Ma (Dunlop and Özdemir 1997) are found in continental sediments, sedimentary rocks or lava flows. These records serve to reconstruct continental drift or field reversals that occurred before the mid-Jurassic. Today, the use of magnetic records in reconstructing the earth's paleofield or continental drift is an established method in the earth's sciences.

The magnetic parameter on which paleomagnetic studies are based is the natural remanent magnetization (NRM). The interpretation of NRMs from marine sediments requires a detailed knowledge of recording mechanisms, magnetization structure and composition of the magnetic minerals carrying the paleomagnetic signal.

An application of the field of micromagnetics is the investigation of magnetization structure of grains. The ability of a grain to carry a stable magnetic signal depends on its magnetization structure which in turn depends on factors like size and shape. Thermally stable grains with uniform magnetization structure are the most reliable carriers of magnetic signals. Therefore, the knowledge of the size range of uniform magnetization structure is fundamental to the interpretation of NRMs. Micromagnetic calculations have proved to be an effective tool in investigating magnetization structures (Williams and Dunlop 1989; Williams and Wright 1998; Fabian *et al.* 1996; Newell 2000). These studies focused on rectangular magnetite particles. However, naturally occurring magnetite is usually not rectangular in shape, euhedral magnetite is octahedral and magnetic grains used by some bacteria to navigate have a wide variety of shapes, Fig. 1. There are discrepancies between the rectangular micromagnetic models and experimentally observed behavior which explains the need for models which take into account the natural shape of magnetic grains.
Magnetotactic bacteria serve as one example for differences in experimentally observed and

numerically predicted behavior. These bacteria reside in the ocean using chains of magnetite magnetosomes (Fig. 1) to navigate through the water column to reach their preferred oxygen environment. In the northern hemisphere, magnetotactic bacteria swim north and downwards since they are microaerophilic and wish to avoid aerobic surface water. Their counterparts in the southern hemisphere swim south and downwards. For optimum navigation, the magnetic grains inside the bacteria should exhibit a uniform magnetization since this maximizes magnetic moment per unit mass. Nevertheless, magnetic grains from magnetotactic bacteria found in marine sediments are in size beyond the size range of uniform magnetization predicted by previous micromagnetic calculations for rectangular particles. Micromagnetic calculations taking into account the natural forms should aid in deciding whether this discrepancy is a feature of particle shape.

Another important subject in the interpretation of sedimentary records are the physical mechanisms which influence the formation of a depositional remanent magnetization (DRM) and stable post-depositional remanent magnetization (PDRM) (Tauxe 1993). In reconstructing the earth's paleofield from marine records it is assumed that sediment NRM is acquired parallel to the external magnetic field and that normalized remanent magnetization and paleofield are proportional to each other. Thus, each sedimentary factor influencing the degree of particle alignment alters the magnetic signal and therefore the reconstruction of the past geomagnetic field.

Sedimentary factors influencing the acquired remanence are usually microscale factors acting on a geological timescale (ka). This makes it hard to observe such long term factors experimentally. Influencing effects like particle-aggregation in the water column and Brownian motion have been investigated theoretically by Collinson (1965), Stacey (1972) and Katari and Bloxham (2001). Shcherbakov and Shcherbakova (1987) provided a continuum theoretical description of the properties and mechanisms of PDRM acquisition. Other investigations of PDRM and its influencing mechanisms were mainly based on laboratory sediment redeposition experiments (Kent 1973; Blow and Hamilton 1978; Levi and Banerjee 1990). Here, numerical models which take into account large assemblages of interacting particles are used to obtain a basic understanding of some DRM and PDRM influencing factors.

The advantage of numerical sediment models is that they can be used to investigate the influence of a single process upon remanence acquisition. It is, for example, possible to observe the influence of particle aggregation on acquired magnetization with no contributions from other sedimentary processes. Likewise, the influence of particle shape, external field strength and compaction can be investigated. Once a basic understanding of single processes is achieved, they can be combined to make a step towards a more realistic model. A model sediment with a known error in recorded inclination can for instance be used to investigate the possibility of mistaking erroneous inclinations for non-dipole components of the geomagnetic field.

In the future, further developed numerical models of DRM and PDRM acquisition could even be helpful in understanding 'ghost images' of magnetization reversals as found by Bleil and von Dobeneck (1999).

The first chapter of this thesis states some magnetic basics behind the processes which were numerically modelled. The second chapter focusses on micromagnetic calculations

and a new program for calculating magnetization structures of irregularly shaped particles. The third chapter deals with DRM and PDRM acquisition processes. The discrete element method (DEM) is used to investigate the influence of pressure and external magnetic field strength on PDRM and the influence of van der Waals forces on the sediment fabric. A further study deals with magnetic particles in a fluid and investigates the relaxation behavior of magnetic particles in a fluid by laboratory experiments in comparison to a numerical simulation of this process. The fourth paper again makes use of the DEM to investigate the influences of particle bonds like van der Waals forces on the DRM. In the fourth chapter, the DEM is used to investigate inclination shallowing and its possible implications for paleomagnetism.

1 Basic magnetics

Magnetization and remanence

A magnetic field **H** originating from magnetic material can be quantified using magnetic dipoles. While a single magnetic dipole is associated with an individual atom, the magnetization **M** of a particle is regarded as the sum of its dipole moments μ averaged over the particle's volume. In free space, the magnetic induction **B** is parallel to **H**:

$$\mathbf{B} = \mu_0 \mathbf{H} \tag{1.1}$$

where μ_0 is the permeability of free space (Wagner 1977).
Magnetic materials which are exposed to a magnetic field acquire a magnetization. In a sufficiently high field, the sample magnetization approaches its saturation magnetization M_S. The field strength required to approximately saturate a sample depends on temperature and sample material. For magnetite at room temperature, a field of 300 mT is sufficient. Magnetic materials which retain a magnetization after the field is removed are said to hold a remanence. The maximum remanence which remains after the sample acquired its saturation magnetization is referred to as saturation remanence M_{rs}. According to magnetic properties, a magnetic material can be classified as diamagnetic, paramagnetic, ferromagnetic, ferrimagnetic or antiferromagnetic and only the last three types are able to hold a remanence (Gerthsen 1995).
Magnetite and hematite are important examples of magnetic minerals which carry a remanence and as such they can act as carriers of magnetic information within sediments.

Magnetic domains

Large ferromagnetic grains may contain regions with different directions of magnetization which are called domains. In a grain with uniform magnetization structure, poles inside the grain will cancel out each other, therefore there will only be a charge distribution at the particle's surface, Fig. 1.1. Due to repulsion between adjacent charges, north and south poles of atomic moments at the particle's surface will produce a magnetostatic energy. Dividing the grain into magnetic domains reduces the size of the area with equal and adjacent poles at the surface. This in turn reduces the magnetostatic energy. However, it also requires energy to set up the domain walls between regions of different magnetization. Therefore, there is an optimum number of domains which depends on grain size. Accordingly, there is a size range in which uniform magnetization without domain walls is energetically most favorable. Grains within this size range are called single domain (SD) grains.

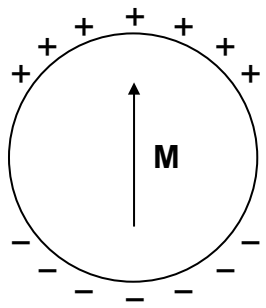

Figure 1.1: Sphere with uniform magnetization **M**. The surface charges are denoted by + and −

The SD size range depends on several factors like shape and saturation magnetization (Butler 1998). Beyond the SD size range, grains start to form domains. Grains with two or more

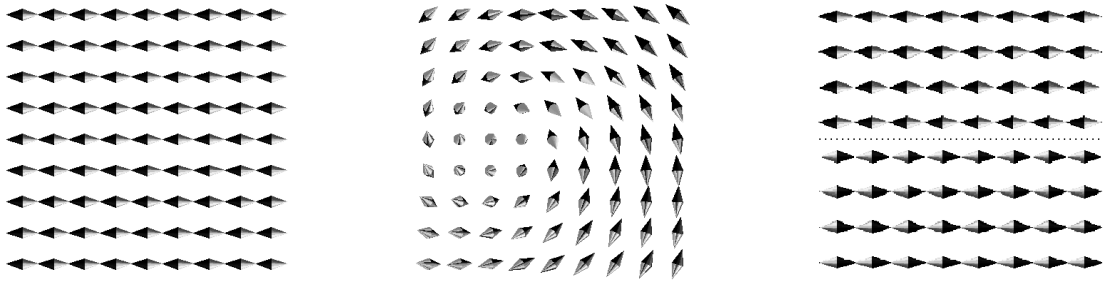

(a) uniform magnetization structure (b) vortex structure (c) two domain structure

Figure 1.2: Magnetization structure of different particle sizes. (a) represents a structure corresponding to a uniformly magnetized SD grain. (b) is a vortex structure which is transitional between SD and MD. (c) is a grain with two magnetic domains.

domains are called multi-domain (MD) grains, Fig. 1.2. Ideal SD grains which change magnetization by coherent rotation of their atomic moments can be extremely stable carriers of magnetic remanence. Observations and calculations show that MD grains are less stable remanence carriers since their domain walls may move during heating or within an external magnetic field (Hubert and Schäfer 1998).

However, there is no sharp boundary between SD and MD particles, Fig. 1.3. Small MD grains exhibit a mixture of MD and SD like properties. Some of them occur in a meta-stable SD state and are almost as stable as SD particles in recording a remanence. Particles with magnetic properties between SD and MD grains are called pseudo-single domain (PSD) grains. PSD behavior is important since the most common magnetic grains size range in natural samples is PSD. SD grains below a critical size become super-paramagnetic (SP). An SP grain cannot carry a stable remanence as thermal activation frequently reverses its moment (Hubert and Schäfer 1998).

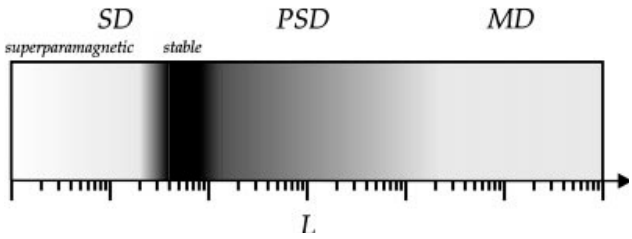

Figure 1.3: Size dependence of magnetization structure (Fabian and Hubert 1999). In this rock magnetic qualitative particle size classification with respect to remanence, the logarithmic length scale ranges from approximately 1 nm on the left side to 1 mm on the right side in the case of magnetite. High remanence is indicated by dark regions and low remanence by light regions.

The recording mechanism needed for geomagnetic investigations must be stable over geological time scales. Equidimensional magnetite grains with an edge length of 28 nm lose remanence within less than a minute. In contrast, cubic grains with an edge length of 37 nm can keep the remanence for more than a billion years (Dunlop and Özdemir 1997). Depending on their shape, the maximum SD size range for magnetite particles lies between 70 nm and 200 nm.

2 Micromagnetics

The recording quality of magnetic grains depends on material, size and shape. Paleomagnetic investigations of marine sediments rely on the proper recording of the paleofield by magnetic grains. Therefore, sediments with a grain size distribution covering magnetic SD particles are more suitable for paleomagnetic studies than sediments with a high content of MD particles. Sediment-magnetic investigations provide information about particle size and mineralogy of a sample. Still, it is essential to know the size range of SD particles in order to decide whether the magnetic grains are stable carriers of magnetization or not. Micromagnetic calculations give insight into the question how large a magnetic particle can be and still remain a stable carrier of a magnetic signal.

The evidence that there are magnetic grains which are stable in recording magnetic signals in terms of geological time scales was first provided by the theoretical descriptions of small magnetic grains by Néel (1949). The micromagnetic structure of a grain which generates a magnetic signal provides information about the stability of the magnetic record. The magnetic energy of a particle is described by micromagnetic equations which date back to Brown (1963) who first formulated them following the work of Landau and Lifshitz (1935) and Kittel (1949). Since the domain structure of a grain corresponds to an energy minimum, this structure can be detected by finding a configuration which yields a minimum in the micromagnetic equations. In most cases, the micromagnetic equations are not solvable analytically and a numerical routine has to be applied. The first three-dimensional micromagnetic calculations were carried out in the material sciences by Schabes and Bertram (1988) and in rock magnetism by Williams and Dunlop (1989).

In the study of magnetotactic bacteria as well as in most other geomagnetic applications, the interest lies in finding the size below which grains are stable carriers of magnetization and above which the recorded signal becomes less stable. Magnetite is the most important carrier of paleomagnetic information and occurs in many natural rocks. Therefore, in the geosciences, micromagnetic calculations usually focus on magnetite grains.

The size boundaries of magnetic grains are also of interest for the recording media industry. In this field, the interest lies more on how small a magnetic particle can get and still be a stable carrier of magnetic signals since hard disks should have as much memory as possible and consume as little space as possible.

Micromagnetic energy terms

The free magnetic energy of a particle is the sum of different energy terms, including anisotropy energy, demagnetizing energy, exchange energy and external field energy. All these energies vary as functions of the particle's magnetization structure and which energy term dominates the other terms is a function of particle size.

The *anisotropy energy* E_a is caused by the coupling of spins to the particle's crystal lattice. Magnetization in a particle points along preferred directions, called the easy axes of the particle. The energy difference in saturating an unmagnetized sample in a chosen direction to saturating the same unmagnetized sample in direction of the easy axis is a

measure for the particle's anisotropy. In a cubic crystal,

$$E_a = \int_V [K_1(m_x^2 m_y^2 + m_y^2 m_z^2 + m_z^2 m_x^2) + K_2 m_x^2 m_y^2 m_z^2] dV \tag{2.1}$$

m_x, m_y and m_z are the direction cosines of magnetization with respect to the crystal's cubic axes, V is the sample volume and K_1 and K_2 are the temperature dependent cubic anisotropy constants.
The field $\mathbf{H}_d$ due to interactions of all magnetic dipoles of a particle opposes the parallel alignment of dipoles by aligning them with their own magnetic field. It is the gradient of a scalar potential,

$$\mathbf{H}_d = -\text{grad}\,\phi \tag{2.2}$$

where

$$\phi(r) = \frac{M_S}{4\pi}\left[\int_V \frac{-\text{div}\,\mathbf{m}(\mathbf{r}')}{|\mathbf{r}-\mathbf{r}'|}\,dV' + \int_S \frac{\mathbf{m}(\mathbf{r}')\cdot\mathbf{n}(\mathbf{r}')}{|\mathbf{r}-\mathbf{r}'|}\,dS'\right]. \tag{2.3}$$

S the surface and $\mathbf{n}$ is the outward surface normal. The effect of this field is described by the *demagnetizing energy* E_d,

$$E_d = -\frac{1}{2}\mu_0 M_S \int_V \mathbf{m}\cdot\mathbf{H}_d\,dV. \tag{2.4}$$

The quantum mechanical coupling of spins between neighboring atoms generates the *exchange energy* E_e. It favors a parallel alignment of spins thus acting against the demagnetizing energy,

$$E_e = A\int_V (\text{grad}\,\mathbf{m})^2\,dV. \tag{2.5}$$

The exchange constant A determines the coupling strength between neighboring spins.
The energy E_h caused by the presence of an *external field* $\mathbf{H}_e$ aligns spins to the external field.

$$E_h = -\mu_0 M_S \int_V \mathbf{m}\cdot\mathbf{H}_e\,dV \tag{2.6}$$

The total magnetic energy E_t of the particle as considered here is the sum of these four energy terms.

$$E_t = E_a + E_d + E_e + E_h \tag{2.7}$$

Micromagnetic computations

Solving the micromagnetic equations for a minimum will lead to the magnetization and thus domain structure of the respective particle. The computationally most challenging energy term is the demagnetizing energy. It requires the calculation of the influence of all magnetizations upon all other magnetizations within the particle. The first micromagnetic programs used the demagnetizing energy calculation according to Rhodes and Rowlands (1954). More recent programs, e.g. Fabian *et al.* (1996), are based on concepts of Berkov *et al.* (1993a) and make use of a Fast Fourier Transform to accelerate the calculation of

E_d. In calculating the exchange energy, the difficult part is the micromagnetic boundary conditions which requires that the derivative of **m** normal to the surface vanishes at the surface. This can easily be accomplished for rectangular particles but is more difficult to realize for arbitrarily shaped surfaces. The advantage of the presented new micromagnetic program over existing programs is that arbitrarily shaped particles can be investigated.

Three-dimensional micromagnetic calculations for naturally shaped magnetite: Octahedra and magnetosomes

Anne Witt, Karl Fabian and Ulrich Bleil

Universität Bremen, FB Geowissenschaften, Postfach 330440, 28334 Bremen, Germany, Tel. +49-421-218-3933, Fax +49-421-218-7008, Email witt@informatik.uni-bremen.de

Abstract

A three dimensional micromagnetic algorithm for modelling naturally shaped particles is presented. It uses a FFT accelerated calculation of the demagnetizing energy. Exchange energy calculation directly takes into account the micromagnetic boundary condition. A rectangular grid enclosing the particle is chosen to economically fit the shape. After verifying that the new program reliably reproduces previous calculations, the program is used to determine room temperature magnetization structures and single domain to vortex transition sizes. These calculations are performed for octahedral magnetite and magnetosomes of different elongations. The least energy magnetization structures of octahedral particles are similar to the flower and vortex states found for cubic particles. The critical size d_0 above which an inhomogeneous magnetization structure has lower energy than the homogeneous flower state as well as the grain-size dependence of M_{rs}/M_s closely resemble cubic particles. However, meta-stable flower states persist up to much larger grain size in octahedral magnetite. This explains previous observations of large TRM/ARM peaks in hydrothermal magnetite. In realistic magnetosome geometries, the SD-PSD transition is shifted towards larger grain sizes as compared to previous estimates based on elongated rectangular grains. For substantially elongated grains this is a result of the alignment of the particles' long edge with the crystallographic easy axis. For more equi-dimensional grains, the rounded ends of magnetosomes reduce spin deflection at the top and bottom edges. Thereby, the formation of nucleation centers is effectively inhibited even without additional stabilization by magnetostatic interaction within a magnetosome chain.

Keywords: rock magnetism; micromagnetics; magnetosomes

In Press, Earth and Planetary Science Letters

Introduction

Naturally shaped particles

The interpretation of natural remanent magnetization (NRM) in paleomagnetic studies as well as the understanding and predicting of the magnetic behavior of natural rocks in environmental magnetism requires detailed knowledge of domain state and composition of the magnetic minerals involved.

Fine grains of magnetite are abundant as natural carriers of paleomagnetic information. To gain a basic physical understanding of their magnetization structures as a function of grain size micromagnetic calculations have been increasingly used in the last years (Williams and Dunlop 1989; Fabian *et al.* 1996; Williams and Wright 1998; Newell and Merrill 2000).

These studies focussed, however, on rectangular particle shapes for which the demagnetizing energy can be calculated fast and efficiently (Berkov *et al.* 1993b; Fabian *et al.* 1996; Wright *et al.* 1997).

Attempts to model more irregular particle shapes have to cope with several problems. If the rectangular grid is replaced by an irregular grid, the demagnetizing energy has to be calculated on this grid either in an inefficient way leading to quadratic increase of computation time with the number of cells or by using a vector potential approximation which may not converge to the correct demagnetizing energy value with decreasing cell size. The latter approach is currently extensively followed in the material sciences especially for magnetically hard materials (Schrefl 1999; Fidler and Schrefl 2000). On the other hand, using a rectangular grid can be inefficient in terms of grid-to-particle volume ratio (Williams and Wright 1998). It increases the inevitable discretization error and complicates exchange energy calculation which in advanced models uses many grid cells to approximate the second derivatives of the magnetization function (Fabian *et al.* 1996; Wright *et al.* 1997).

Yet, there is good reason to apply micromagnetic modelling to irregular particle shapes. Micromagnetic models of cubic or rectangular magnetite particles have steadily advanced during the last decade. Nevertheless, there are still discrepancies between calculated and experimentally observed magnetic properties. An especially well documented example is the existence of bacterial magnetosomes with sizes beyond the maximal single-domain range as calculated by micromagnetic models of rectangular particles (Petersen *et al.* 1989; Fabian *et al.* 1996).

Since biomineralization of magnetite in magnetotactic bacteria is supposed to be extremely efficient and since SD particles are optimal remanence carriers, the calculations of Fabian *et al.* (1996) either indicate that some magnetosome SD states are stabilized only by magnetostatic interaction within a magnetosome chain, or that the assumed rectangular particles do not fit the real situation.

Here it is argued that the difference between observation and micromagnetic modelling in Fabian *et al.* (1996) is exclusively due to the difference in shape between naturally occurring magnetosomes and the modelled rectangular prisms. The here presented calculations for more realistic magnetosome shapes indicate that single bacterial magnetosomes allow for meta-stable SD states at much larger grain sizes than the corresponding rectangular particles. It is therefore proposed that the existence of a meta-stable SD state is a characteristic feature

of single non-interacting magnetosomes in magnetotactic bacteria.

In addition, particle shape is assumed to be of considerable importance for the so called pseudo-single domain moment (Stacey 1961; Fabian and Hubert 1999), but its influence on magnetic properties has not yet been systematically investigated. Specially shaped grains which have been considered in rock magnetic applications of micromagnetic modelling are a squeezed octahedron, a cubo-octahedron and an imperfect cube (Williams and Wright 1998) as well as cross-shaped particles (Tauxe *et al.* 2002) .

The here presented new code for three-dimensional micromagnetic calculations is used to determine magnetization structures and critical transition sizes of euhedral magnetite (octahedral shape). Their equilibrium magnetization states turn out to have essentially the same grain size dependence of M_{rs}/M_s as cubic grains. Yet, meta-stable single domain magnetization structures can exist in a considerably larger grain size region.

Micromagnetic Algorithm

The new program consists of two parts. The first (GRID) constructs a grid representation of the irregular particle and is used once for each grid resolution and particle shape.

Each grid obtained this way can be used for an arbitrary number of micromagnetic energy minimizations for varying particle sizes or material constants. These calculations are performed in the second part, the micromagnetic minimization routine (MMR).

Since some operations of GRID are easier to understand on the basis of the MMR algorithms, these are discussed first.

The micromagnetic minimization routine

MMR is a considerably enhanced version of the three-dimensional micromagnetic algorithm of Fabian *et al.* (1996). It minimizes exchange, anisotropy, external field and demagnetizing energy on a cubic grid. The magnetization within each grid cell is assumed to be constant. Details of the basic algorithms for anisotropy, exchange and demagnetizing energy are described in Fabian *et al.* (1996). Only those parts which have been adapted to carry out micromagnetic calculations for irregular convex particles are discussed more explicitly here.

The non-cuboid shape of the particle P is accounted for by weighting the magnetization $m_{i,j,k}$ of each cubic grid cell $C_{i,j,k}$ with the volume fraction $v_{i,j,k}$ of the intersection between grid cell and particle, $v_{i,j,k} = \mathrm{vol}(P \cap C_{i,j,k})/\mathrm{vol}(C_{i,j,k})$, and $v_{i,j,k} \in [0,1]$. Using this notation and d being the length of a cubic grid cell, the actual volume of the grid cell that is taken up by the particle is $V_{i,j,k} = v_{i,j,k}\, d^3$. The weighting of the magnetizations explains the need for calculating the grid cells' volume fractions.

The next important step where particle shape comes into place is the calculation of the exchange energy density and its gradient. These calculations involve the evaluation of the Laplace operator:

$$E_{ex} = A \int (\nabla \mathbf{m})^2 dV = -A \int \mathbf{m} \Delta \mathbf{m}\, dV. \tag{2.8}$$

The second equality uses $\mathbf{m}^2 = 1$ which yields $-\mathbf{m}\Delta\mathbf{m} = (\nabla\mathbf{m})^2$. The discrete version therefore is

$$E_{ex} = -A \sum_{i,j,k} V_{i,j,k}\, \mathbf{m}_{i,j,k}\, \Delta\mathbf{m}_{i,j,k}. \tag{2.9}$$

With an infinitesimally fine grid, the boundary condition of vanishing normal derivatives at the particle's boundary should automatically be fulfilled. This is not necessarily the case with a coarser grid. In order to meet this boundary condition even with a coarser grid, the condition $\partial\mathbf{m}/\partial\mathbf{n} = 0$ at the particle's surface is artificially enforced during the exchange energy calculation. Following an idea of A. Hubert (personal communication), the best way to accomplish this is by reflecting the interior magnetization of cells within a two grid cell layer at the particle's surface (Gibbons *et al.* 2000).
This leads to quadratic approximations across the boundary with vanishing normal derivative at the boundary.
The required mirror images of magnetizations $\mathbf{m}^*_{i,j,k}$ at places (i,j,k) outside the particle are obtained by reflecting the respective outer cells' centers at the particle's boundary into the inside of the particle. At these inner points $(i,j,k)^*$, the corresponding magnetizations are interpolated using the surrounding cells' magnetizations $\mathbf{m}_{i',j',k'}$:

$$\mathbf{m}^*_{i,j,k} \;=\; \sum a^{i,j,k}_{i',j',k'} \mathbf{m}_{i',j',k'}. \tag{2.10}$$

where $a^{i,j,k}_{i',j',k'}$ are the interpolation coefficients. This explains the need for mirror images of magnetizations as well as volume fractions with regard to the cubic grid. These are the most time consuming parts of the GRID routine. When only cubic particles are considered, these calculations do not bear any problem as there are no volume fractions to be calculated.
Since the parameters $a^{i,j,k}_{i',j',k'}$ and $V_{i,j,k}$ are independent of particle volume (grid size) and invariant during the micromagnetic energy minimization, these computations have to be carried out only once for each particle geometry. For each box, the information whether it is completely inside, partially inside or outside the particle is stored in a file. Volume fraction as well as interpolation coefficients, if needed, are also written to this file. This GRID output file is read by the MMR and contains all information to perform the energy minimization.

The calculation of the demagnetizing energy and its gradient uses a highly efficient FFT routine (Frigo and Johnson 1998) which requires less memory and considerably accelerates the code in comparison to previously used FFT routines.

Magnetostriction is not taken into consideration because the size of the modelled magnetite particles is far below the characteristic length of 5.4 μm (Fabian *et al.* 1996; Hubert 1988) above which magnetostrictive self-energy starts to dominate the domain structure. External stress is also not considered here, even though it can easily be included.

MMR allows to choose between several energy minimization methods. Either simulated annealing can be used to search for globally optimal minima or a much faster conjugate gradient method may be applied for local minimization (Williams and Dunlop 1989; Fabian *et al.* 1996). Alternatively, it is possible to use a modified downhill search algorithm (Berkov *et al.* 1993b).

The GRID routine for convex particle representation

Starting from a geometric description of particle shape in terms of vertex coordinates, the initial routine (GRID) generates a grid representation of the particle together with the interpolation coefficients and volume fractions as needed by MMR.

GRID starts by producing about 186600 spherical rotations $P_i = R_i P'$ of the original particle P', where R_i denotes the i-th rotation matrix. For each of them it finds the minimal enclosing box B_i with edges parallel to the coordinate axes. Among them, it chooses the optimally rotated particle $P = P_i$ with maximal ratio $\mathrm{vol}(P_i)/\mathrm{vol}(B_i)$.

From the rotation matrix R_i together with the initial crystallographic coordinate system of P', the anisotropy energy matrix and its gradient can be computed.

In a second step, the vertex representation of the rotated polyhedral particle P is transformed into a representation by linear inequalities, each representing a half space which contains P and corresponds to one of the polyhedral faces. This transformation relies on the Quickhull algorithm for convex hull computation and uses the corresponding program qhull (Barber *et al.* 1996) which returns a matrix A and a vector b such that $x \in P$ is equivalent to $Ax \leq -b$. Using this inequality representation, it is easy to determine for each grid cell $C_{i,j,k}$ whether it lies completely inside the particle, completely outside, or whether it intersects the particle's boundary.

This is done by checking whether all eight grid cell vertices fulfill the particle inequalities. For cells at the boundary of P the inequalities are fulfilled by only one to seven vertices. For these cells $C_{i,j,k}$, another algorithm of qhull is used to compute the respective volume fractions $v_{i,j,k}$ (Barber *et al.* 1996). This algorithm requires an inner point $p \in P \cap C_{i,j,k}$ as additional input. GRID tries to locate such a p by successively shifting the vertices of $C_{i,j,k}$ within $P \cap C_{i,j,k}$ by a minute distance towards the center of $C_{i,j,k}$.

In most cases, this method is successful, yet there are extreme configurations where $P \cap C_{i,j,k}$ either contains no vertex of $C_{i,j,k}$ at all, or no inner point of $P \cap C_{i,j,k}$ lies on the connection of the inner vertex with the center of $C_{i,j,k}$. Since such cases occur very rarely and the respective volume $v_{i,j,k}$ is negligible with respect to the discretization errors of the energy calculation, further treatment of these special cases has been omitted by setting $v_{i,j,k} = 0$. The next version of GRID will first determine all vertices $q_k,\ k = 1, \ldots, K$ of $P \cap C_{i,j,k}$ and then use the center of gravity $p = 1/K \sum q_k$ as inner point. However, this considerably increases the computational effort.

In calculating the exchange energy, the boundary condition $\partial m/\partial n = 0$ has to be accounted for. This boundary condition is fulfilled if the outer cells that lie within a distance of two cells away from the particle's boundary contain mirror images of the inner magnetizations, as sketched in Figure 2.1. Each mirror image is obtained by first reflecting the cell center of the outer cell at the particle faces into the particle's interior. Then, trilinear interpolation coefficients with respect to the surrounding boxes are computed. These interpolation coefficients are used to determine the mirror image in terms of the inner magnetizations.

For cells that cannot be reflected easily at a particle's face, the mirror image is interpolated

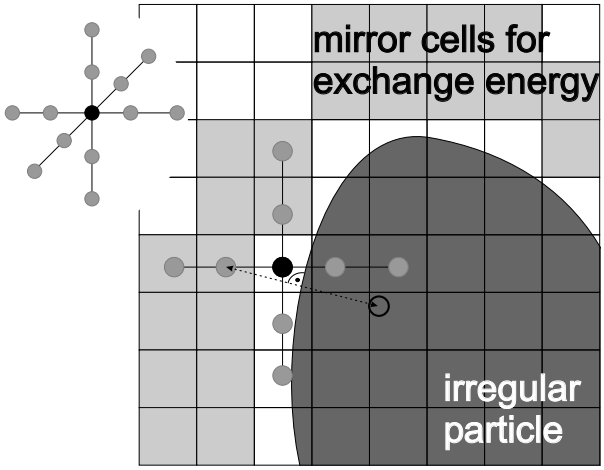

Figure 2.1: The three-dimensional five point approximation of the Laplace-operator (top left) uses the magnetizations of 12 surrounding cells to estimate the second derivatives in the center (black). The required virtual magnetizations in outer cells of the particle's grid representation (light gray) are obtained by interpolating the magnetizations of their mirror images inside the particle. Thereby it is possible to directly include the condition $\partial m/\partial n = 0$ at the particle boundary into the exchange energy calculation.

from the surrounding cells mirror images.
The program finally returns the rotation matrix for the particle, the optimal dimensions of the rectangular box, the interpolation coefficients, and the volumes $V_{i,j,k}$.

Program Verification

Cubic Particles

Both routines, GRID and MMR, contain newly developed algorithms and all parts from previous programs are transferred to C++. To test the new program, the SD-PSD transition of cubic magnetite particles is calculated and compared to literature data (Fabian *et al.* 1996; Wright *et al.* 1997). The calculation uses the same material parameters as these previous studies: $M_s = 4.8 \cdot 10^5$ A/m, $K_1 = -1.25 \cdot 10^4$ J/m^3 (Fletcher and OReilly 1974) and $A = 1.32 \cdot 10^{-11}$ J/m (Moskowitz and Halgedahl 1987; Heider *et al.* 1988).

To compare SD-PSD transitions of differently shaped particles, all size dependent quantities are evaluated as a function of the spherical diameter d which is the diameter of a sphere with the same volume as the particle. In Figure 2.2, results obtained from different minimization runs for cubic magnetite particles are shown by plotting energy density versus spherical diameter. The first minimization run starts with cubes of $d \approx 40$ nm, homogeneously magnetized along a cube diagonal which is an easy anisotropy axis. After minimization, the magnetization structure is a flower-state. Its edge magnetizations slightly bend outward partially aligning with the intense stray-field produced by the largely homogeneous magnetization. Subsequent minimizations in this run stepwise increase particle size d. The initial state at each minimization is the optimal magnetization state of the previous run.

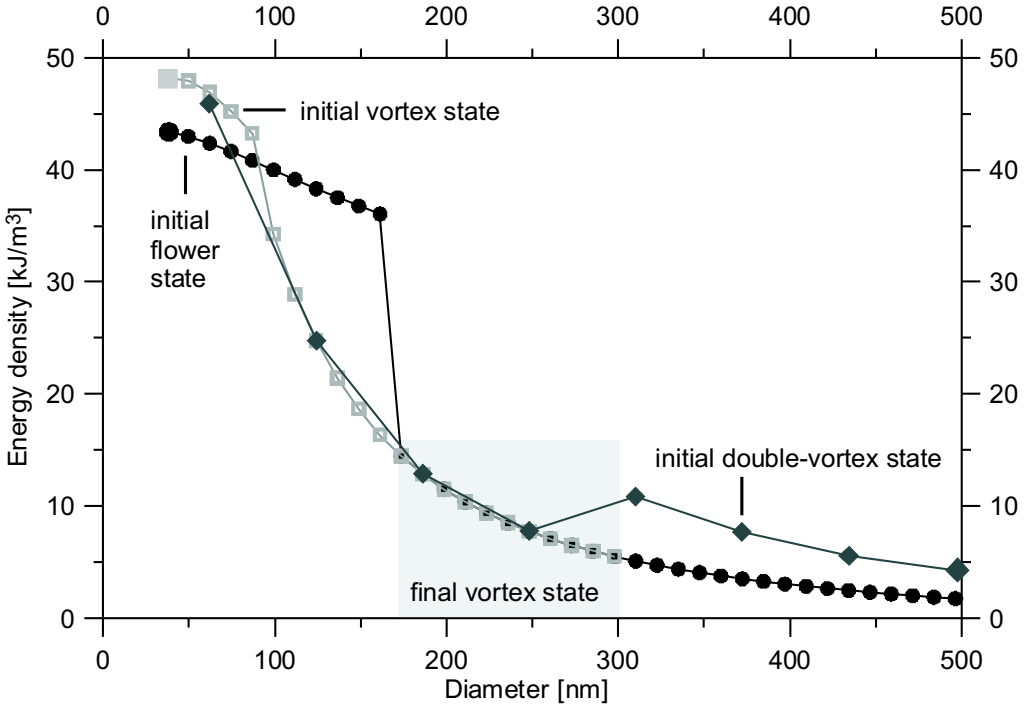

Figure 2.2: Energy density of various magnetization structures as a function of spherical diameter for cubic particles. Each symbol represents a stepwise minimization run which starts at either minimal or maximal grain size (big symbols) in a prescribed initial magnetization state. At each grain size step the final result of the previous minimization is used as the new initial model. The first minimization run (black circles) starts with small particles homogeneously magnetized along a cube diagonal which is an easy anisotropy axis. The second minimization run (dark diamonds) starts with a double vortex at maximal particle size, while the third run (light squares) starts again at small particles, but with a vortex initial-state. The grid resolution of the particle used for these calculations is 15^3, while the total grid resolution including outer cells for exchange energy calculation is 19^3. Inside the light shaded region, only vortex states occurred as final magnetization structures.

This process gradually yields the sequence of black circles in Figure 2.2. The most prominent feature of this graph is the discontinuity at $d \approx 160$ nm. At this point, the minimum energy drops from 38 to 15 kJ/m^3 marking a spontaneous change of magnetization structure from a nearly homogeneous flower-state into a non-homogenous vortex state of considerably lower energy.

A second minimization run starting with a vortex initial-state at $d \approx 40$ nm shows that this state for small d is energetically less favorable than the flower state (light squares in Figure 2.2). However, above a critical diameter of $d_0 \approx 87$ nm, the vortex state requires less energy than the flower state. This result coincides with an equivalent previous study (Fabian *et al.* 1996) where the critical edge length obtained is 68 nm, corresponding to a critical diameter of $d_0 \approx 84$ nm. In Muxworthy *et al.* (2003) a critical edge length of 64 nm is reported, amounting to $d_0 \approx 79$ nm. The position of the discontinuity in the first graph (solid circles in Fig. 2.2) approximately indicates the grain size at which the flower state ceases to be a local energy minimum. An exact determination of this position requires the calculation of the energy barrier between flower and vortex state. Although there are

methods to reliably estimate this barrier (Winklhofer *et al.* 1997; Muxworthy *et al.* 2003), the upper stability limit has not yet been determined. Our result of $d \approx 160$ nm is in between the values of Muxworthy *et al.* (2003) ($d \approx 119$ nm) and Fabian *et al.* (1996) ($d \approx 174$ nm). These estimates, however, depend on details of the minimization routine used. Routines which are able to overcome minor energy barriers lead to smaller transition sizes than routines which exclude this possibility.

The same difficulties apply to the question whether double vortex states are meta-stable or unstable (Muxworthy *et al.* 2003). In our calculations, starting with initial flower states, the minimized magnetization structure changes from a flower state directly into a vortex state between 161 nm and 174 nm. However, this change occurs only if either the computational accuracy is restricted to single-precision or if the conjugate gradient minimization is restarted twice in each minimization. In both cases, the algorithm is able to step over tiny energy barriers, which either are artificially produced by the discrete model, or otherwise are related to real physical barriers. Therefore, the currently available data do not allow to exactly delimit the region of stability of double vortex states.

A third minimization run (diamonds in Fig. 2.2) starts at large particle sizes of $d \approx 500$ nm with an initial double vortex state. Here, a stepwise decrease of d indicates that the double vortex remains a meta-stable energy minimum down to $d \approx 300$ nm. Below this point, it collapses into the energetically favorable vortex state. This result does not prove that the double vortex state is a local energy minimum for cubic magnetite above $d \approx 300$ nm. It does compare well though with the more rigorous finding that in uniaxial cubic particles, double vortex states in a small range of material parameters even occur as absolute energy minima (Rave *et al.* 1998).

Applying the new algorithm to cubic particles, the bi-logarithmic plot of M_{rs}/M_s as a function of d yields a straight line with slope -3.06. The slope for synthetically grown magnetite crystals of approximately -0.6 (Dunlop 1995) is considerably different. This might partly be due to residual stress present even in ideally grown crystals. Another reason could be the shape irregularity which according to Fabian and Hubert (1999) tends to increase the residual remanence.

Results for Octahedral Magnetite and Magnetosomes

Having tested the new routines reliability, the following subsections present transition sizes and characteristic magnetization structures calculated for special natural particle shapes. The first subsection deals with magnetite octahedra at room temperature (Fig. 2.3a), the second with different elongations of an exemplary realistic magnetosome geometry (Fig. 2.3b). In both cases, the modelled anisotropy energy agrees with the natural crystallographic system in relation to particle geometry as shown in Figures 2.3a and 2.3b.

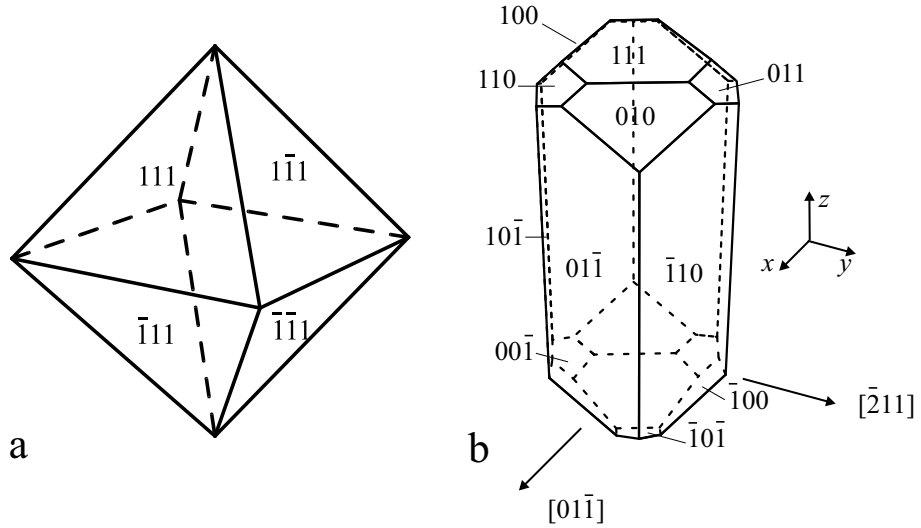

Figure 2.3: (a) Crystallographic orientation of a natural magnetite octahedron. (b) Crystal morphology of a typical magnetosome as inferred from electron microscopic images (Mann 1985). Different elongations are modelled by changing the length along the [111]-direction.

Octahedral Particles

The investigation of magnetite octahedra is of special interest in rock magnetism since euhedral magnetite assumes this shape. Different argumentations can be put forward as to whether shape effects in this case increase the SD-PSD transition size or influence the slope of M_{rs}/M_s as a function of d. On one hand, a homogeneously magnetized octahedron has the same demagnetizing tensor N as a sphere or a cube, which indicates that the SD-PSD transition size should be comparable. On the other hand, in uniaxial octahedra containing a single domain wall, the non-cuboid shape should strongly influence the size dependence of M_{rs}/M_s. To test these presumptions, we used our program to determine the optimal magnetization states of octahedral magnetite particles.

As in the case of cubic particles, we started the first minimization run with an initial state of homogeneous magnetization along an easy anisotropy axis. This evolved into a flower state which in turn was used as the initial state for the next minimization at slightly increased d. Repeating this procedure led to the plot of energy density versus spherical diameter indicated by black circles in Figure 2.5. Above the critical diameter $d_0 \approx 88$ nm, the octahedral vortex state requires less energy than the flower state. This nearly perfectly coincides with the corresponding value for cubic particles, although the energy density of octahedral flower states is about 10% lower than the energy density in cubic flower states of the same volume (Figure 2.2). This difference is mainly due to exchange energy. The comparison of exchange and demagnetizing energy density in Figure 2.4 indicates that flower states in small cubic grains require more small scale spin deflections and accordingly more exchange energy than flower states in octahedral grains of the same size. The latter show strong bending only in the vicinity of the octahedron vertices. Anisotropy energy is not important in both particle geometries.

The total energy of the flower state in octahedra is lower than in cubic particles of the

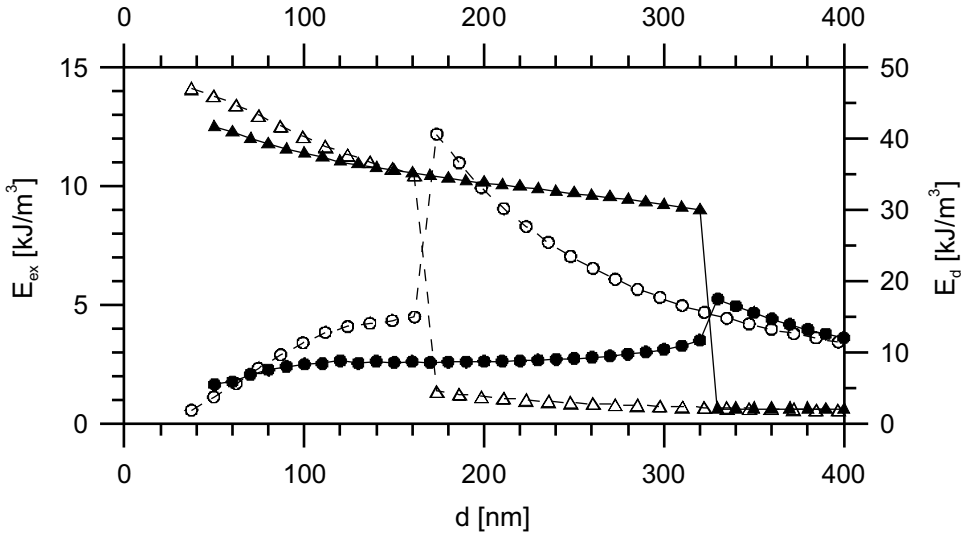

Figure 2.4: Exchange (circles) and demagnetizing (triangles) energy densities as a function of spherical diameter for octahedral (solid symbols) and cubic (open symbols) particles. While above a diameter of 70 nm the flower state requires less exchange energy in octahedral than in cubic particles, the situation is opposite for the vortex state beyond 330 nm. Note the different energy scales.

same volume. Even though this provides no dependable information about the energy barrier between flower and vortex states, it still is probably related to the observed substantial enlargement of the region where a meta-stable flower state persists. Only above a spherical diameter of 320 nm the flower state becomes unstable and, by itself, switches into a vortex state (Figure 2.5).

An important implication of the high stability of meta-stable flower states in octahedral magnetite concerns a pronounced peak in TRM/ARM. This peak was experimentally found by Dunlop and Argyle (1997) for PSD magnetite with sizes below about 500 nm. It is much higher than explicable by classical theories of TRM and ARM (Stacey and Banerjee 1974; Shcherbakov and Shcherbakova 1977). Micromagnetic calculations for rectangular magnetite particles reveal that in the peak grain size region, the same particle can support two extremely different meta-stable magnetization states: a high remanence flower state and a low remanence vortex state. The TRM/ARM anomaly in this grain size region therefore appears to be connected to a systematic difference in magnetization states carrying the remanence. High TRM in the peak region can be attributed to high temperature SD states which evolve during the cooling process into a meta-stable flower state with remanence M_F. On the other hand, ARM acquisition more effectively forces the particle into a low energy vortex magnetization state with dramatically lower remanence M_V (Fabian 1998). As shown on the left in Figure 2.6, remanence ratios M_F/M_V between meta-stable states obtained by minimizing initial flower or vortex states in rectangular particles can in principle reproduce the TRM/ARM anomaly.

However, it is astonishing that synthetic hydrothermally grown particles display a more pronounced TRM/ARM anomaly than crushed particles (Dunlop and Argyle 1997), whereas the rectangular micromagnetic models show highest peaks in M_F/M_V for elongated particles

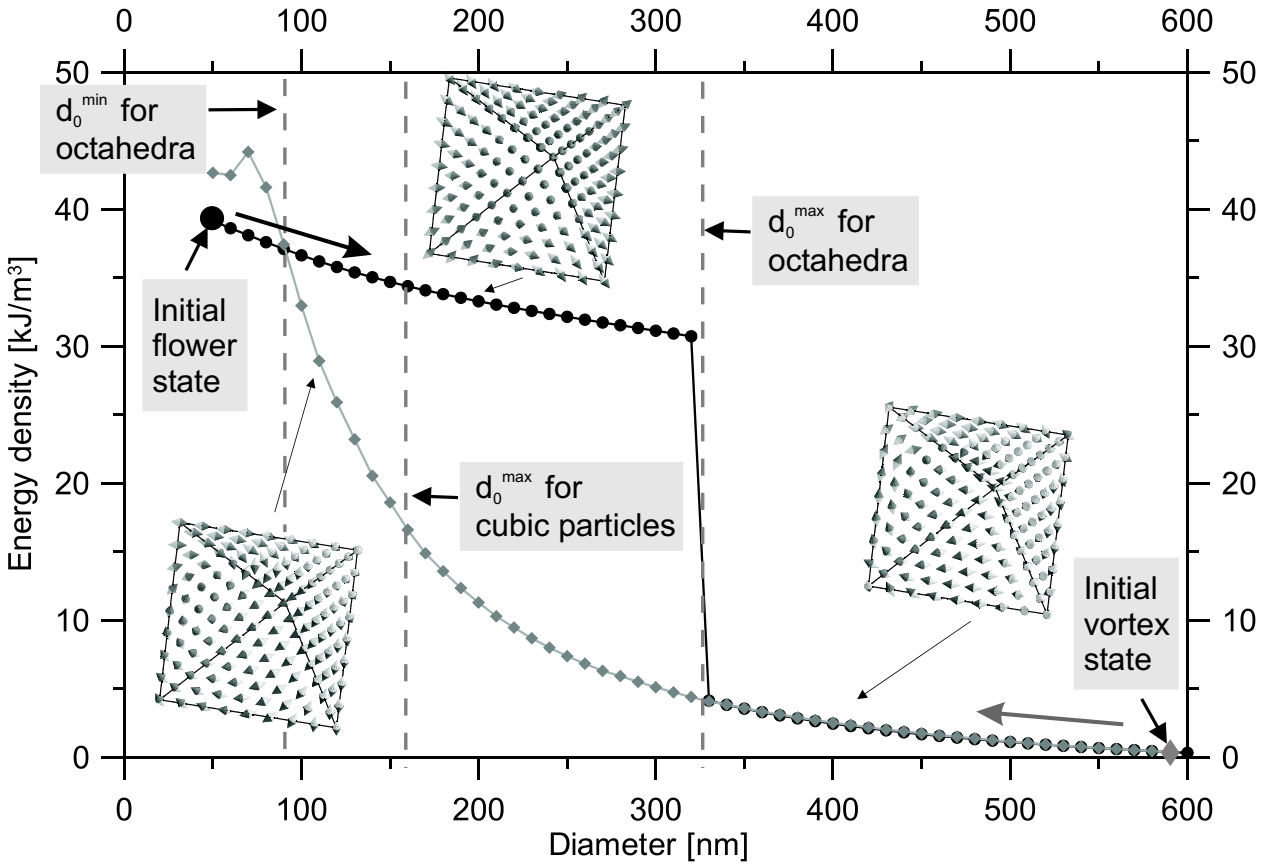

Figure 2.5: Total micromagnetic energy density as a function of grain size for octahedral magnetite. Grain size is defined as the diameter $D = (6V/\pi)^{1/3}$ of a sphere with the same volume V. The first minimization run starts with small particles in SD-state with magnetization pointing along the particle's easy axis. The second minimization run starts with big particles in a double vortex state, proceeding to smaller particles. The third minimization run again starts with big particles but in a vortex state. The resolution of the particle grid is $16 \times 15 \times 16$, while the resolution of the numerical grid is $20 \times 19 \times 20$.

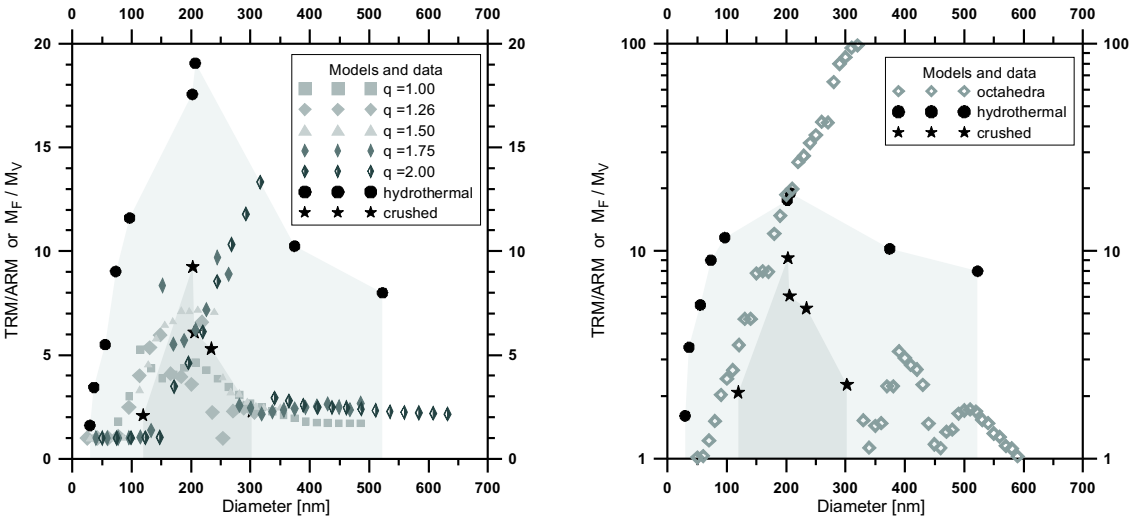

Figure 2.6: Ratio of TRM/ARM in synthetic samples as compared to M_F/M_V obtained from micromagnetic calculations of either rectangular particles with different width-to-length ratios q (left), or octahedral particles (right). Experimental results are plotted after Dunlop and Argyle (1997) using data from Dunlop and West (1969),Dunlop (1973) and Levi and Merrill (1978). Micromagnetic results for rectangular data are taken from Fabian (1998).

(Fig. 2.6). Our calculations for octahedral magnetite lead to an unexpected explanation of this observation. The ratio of M_F/M_V in octahedral particles can assume values up to ≈ 100 (Fig. 2.6), which is considerably larger than any value found for rectangular grains. This high ratio results from two effects: The extreme grain size range where meta-stable flower states persist and the efficient reduction of remanence in the octahedral vortex.

The region where the flower state is the absolute energy minimum is about the same for octahedral and cubic magnetite particles (Fig. 2.5). This is contrary to the much more extended region of meta-stable flower states in octahedra. Still, it supports the above stated intuitive argument that cube, sphere and octahedron should have comparable SD-PSD transition sizes. Also, the bilogarithmic representation of M_{rs}/M_s as function of spherical diameter yields a straight line with about the same slope as obtained for cubic particles.

Elongated Particles and Magnetosomes

After the discovery of magnetotactic bacteria by Blakemore (1975), many different species of this type have been found in marine, lacustrine and soil environments (Blakemore 1982; Petersen *et al.* 1986; Vali *et al.* 1987; Petersen *et al.* 1989; Fassbinder *et al.* 1990; Petermann and Bleil 1993). Identifiable relics of magnetosome chains have been detected in many sedimentary rocks. A current discussion centers around the question of biogenic origin of magnetite minerals found in the martian meteorite ALH84001 (Thomas-Keprta *et al.* 2000).

There is convincing evidence that bacterial magnetite particle chains are efficiently produced to optimize magnetic moment and coercivity. Their use for magnetotaxis requires an often substantial chain moment to produce a magnetic torque which counteracts the viscous drag of the bacterial body and keeps it aligned with the external field (Hanzlik *et al.* 1996).

If several chains are present, they may also act as a magnetic skeleton which stabilizes the bacterial shape (Hanzlik *et al.* 1996). The optimality request holds best if the magnetosomes adopt an – at least meta-stable – SD state inside the chain. Tests of this assumption commonly use the stability diagram of Butler and Banerjee (1975), which is based on a one-dimensional domain wall model for finite grains (Amar 1958). A refined version of this diagram has been obtained using a numerical three-dimensional micromagnetic model for rectangular magnetite particles (Fabian *et al.* 1996). The left panel of Figure 2.7 shows the results of these computations in comparison with aspect ratios of microscopically observed magnetosomes. Apparently, a fraction of the bacterial magnetosomes lies outside the region where the SD state is meta-stable. According to the model calculations, it would assume a vortex magnetization state if not otherwise stabilized. Indeed inhomogeneous magnetization structures have been observed in artificial magnetization states of large magnetosomes (McCartney *et al.* 2001). Additional stabilization arises by magnetostatic interaction within the magnetosome chain. The corresponding interaction field depends critically on relative position and spacing between the magnetosomes. Both parameters change with movement and growth of the bacteria which also may impose considerable bending of the chain (Shcherbakov *et al.* 1997). During cell division this interaction can even break down completely which would then lead to irreversible demagnetization if the SD structure is intrinsically unstable within the non-interacting magnetosome. We therefore hypothesize that also magnetosomes within chains do support a meta-stable SD state without magnetostatic stabilization. This implies that the characteristic magnetosome shape and the corresponding orientation of the cubic anisotropy axes should significantly stabilize the SD state in large magnetosomes. We tested this assumption by modelling a particle geometry which is typical for magnetosomes (Mann 1985).

The general shape and orientation of the cubic anisotropy axes used in our modelling is sketched in Figure 2.3b. Particle length l varies along the central [111]-axis and the definition of the width-to-length ratio q is extended to non-rectangular shapes by setting $q = \sqrt{V/l^3}$, which for rectangular particles of size $w \times w \times l$ correctly yields w/l.

The energetically optimal PSD-states of magnetosomes at larger grain sizes depend on the value of q. For a magnetosome with $q = 1$, a vortex in the xz-plane of Figure 2.3b requires less energy than a vortex in the xy-plane. In contrast, in magnetosomes with $q = 0.9, 0.8, 0.7$ vortexes in the yz-plane are minimal energy states. At $q = 0.6, 0.5, 0.4$ again the vortex in the xy-plane is the optimal energy state. The model calculations started out from these respective lowest energy configurations as initial state. The particle sizes were large in the beginning, then stepwise decreased using the previous final solution as initial state for the next step. The results of these calculations are plotted in the right panel of Figure 2.7. The magnetosome particle diameter d_0^{min} above which a vortex is the lowest energy state steadily decreases from $d_0^{min} \approx 200$ nm at $q = 0.4$ to $d_0^{min} \approx 95$ nm at $q = 1$. On the other hand, the apparent upper stability limit d_0^{max} of the flower state is not monotonous and has a minimum between $q = 0.8$ and $q = 0.9$. However, a thermodynamically correct calculation of d_0^{max} requires the determination of the energy barrier between flower and vortex state, which is beyond the possibilities of our current algorithm. Therefore, our estimates of d_0^{max} cannot prove the physical reality of the observed minimum between $q = 0.8$ and $q = 0.9$.

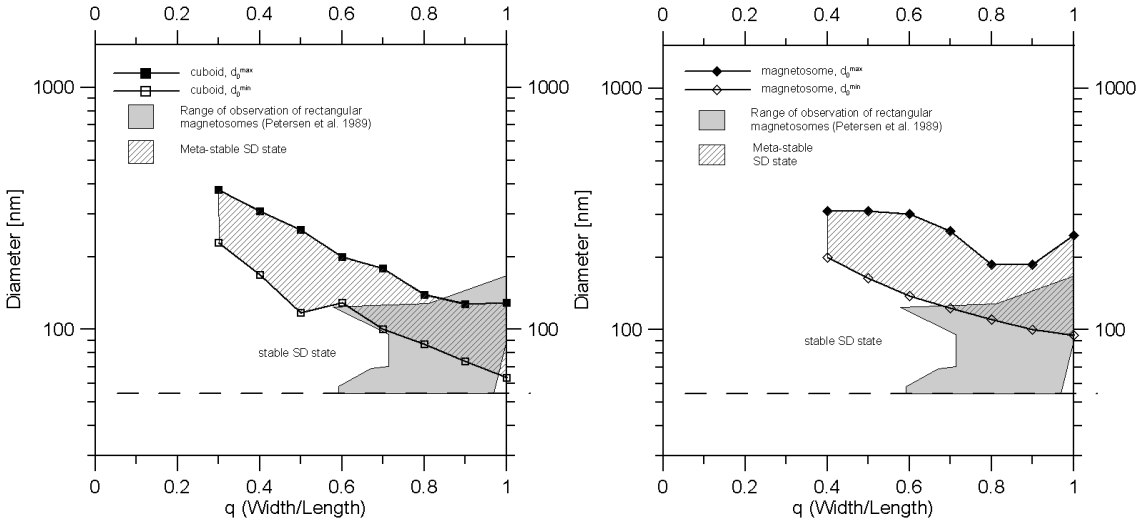

Figure 2.7: Regions of stability and meta-stability of the SD state for rectangular particles (left) or characteristic magnetosomes (right). Displayed is the SD-PDS transition as a function of width over length of the respective particles. The shaded area delineates microscopically observed magnetosome shapes (Petersen *et al.* 1989). The dashed area corresponds to the micromagnetically calculated region where flower states are meta-stable. Above this area the SD state is unstable and cannot persist. See text for further explanation.

Yet, the reliably determined local maximum of d_0^{min} near $q = 0.6$ observed for rectangular particles in Figure 2.7 (left) shows that a change of stable magnetization configurations with elongation also affects the critical diameters. The observation, that the optimal vortex state in magnetosomes with $q = 0.9, 0.8, 0.7$ is different from the ones with higher or lower q thus might well be related to the minimum of d_0^{max}.

The most important outcome of the magnetosome calculations (Fig. 2.7,right) is the confirmation that both types of SD-PSD transitions for magnetosomes occur at larger particle sizes than for elongated cubic particles. The reason for this increased stability of magnetosomes is twofold. First, the easy crystallographic [111]-axis is aligned with the particle elongation which leads to a cooperation of demagnetizing energy and crystal anisotropy. However, this anisotropy effect only accounts for stabilization of elongated particles,. The increase in d_0^{min} and d_0^{max}, though, is especially observed at and near $q = 1$. We attribute this additional stabilization to a geometrical effect. The more rounded shape of the equidimensional magnetosome inhibits strong outward bending of the magnetization at top and bottom edges which is very pronounced in cubic particles. There, it leads to the so-called flower states (Williams and Dunlop 1989). In perfectly elliptical particles, this outward bending is completely suppressed leading to the well-known Brown paradox: in elliptical particles, no nucleation mode is possible and the homogenous SD state persists as a meta-stable state up to arbitrary large grain sizes. The magnetosome shapes studied here are intermediate between rectangular and elliptical shape. In comparison to cubic shapes, nucleation of magnetization swirls is therefore more difficult and occurs at larger particle sizes.

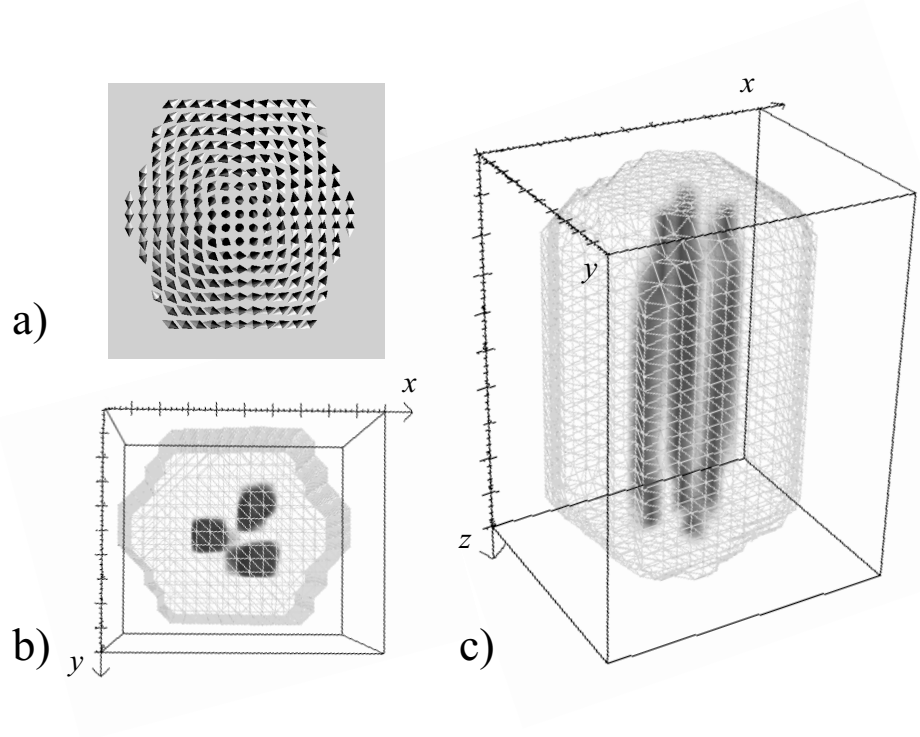

Figure 2.8: Magnetization structure of a stable vortex state inside a modelled magnetite magnetosome of 200 nm length and width-to-length ratio $q = 0.7$. The horizontal xy-slice in a) displays the vortex magnetization structure ranging from top to bottom of the magnetosome. The vortex center is aligned with an easy [111]-direction. Panels b) and c) show different views of the three dimensional anisotropy energy density inside the particle (compare Fig. 2.3b). Dark shading indicates high anisotropy energy. The three high anisotropy tubes ranging from top to bottom of the magnetosome contain information about size and structure of the central vortex. The decreasing distance of the tubes near top and bottom faces reflect a constriction of the vortex.

Spatial structure of the vortex state in magnetosomes

Visualization of complex magnetization structures in irregularly shaped particles is one of the main obstacles when analyzing and interpreting the results of our three-dimensional models. In order to overcome this problem, we apply an interactive software platform designed for visualizing the results from medical tomographies (ILAB 4 by MeVis, Center for Medical Diagnostic Systems and Visualization, Bremen, Germany) (Hahn *et al.* 2003). A specially adapted version of this program allows to display magnetization vectors or local energy densities in space or across arbitrary two-dimensional sections. Here, we report on the somewhat surprising distribution of anisotropy energy within the vortex state of a magnetosome (Fig. 2.8b and c). The general structure of this vortex can easily be derived from cross-sections perpendicular to the long [111]-axis of the magnetosome. The typical appearance is that of the central slide shown in Figure 2.8a. It consists of a single magnetization swirl, the center of which roughly corresponds to the [111] symmetry axis of the particle. In vortex states of rectangular particles, the swirl diameter has been observed to systematically vary throughout the grain while the swirl center may follow a curved line (Fabian 1998).

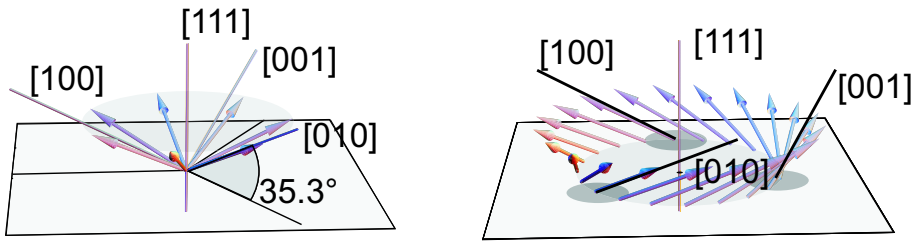

Figure 2.9: Maxima of anisotropy energy density. According to its crystal morphology, the long axis of the magnetosome is aligned with the cubic room diagonal. There are three crystallographic easy axes and three crystallographic hard axes.

To investigate the presence of similar effects in irregularly shaped grains, we observe the variation of local anisotropy energy density within a vortex state of a magnetosome. Figure 2.8c shows that the maxima of anisotropy energy density form three tube-like structures ranging from top to bottom. The presence of these tubes reflects the threefold symmetry of the hard ⟨100⟩-directions with respect to the central [111]-axis. A vortex structure is almost rotationally symmetric in each plane perpendicular to its center. As sketched in Figure 2.9, at a certain distance r from the center the magnetization vector therefore rotates around the center, eventually pointing along any direction on a cone, the opening of which depends on r. Since the hard ⟨100⟩-directions enclose an angle of 54.7° with the central [111]-axis, there is a certain distance r_0 at which exactly this angle occurs and the anisotropy energy becomes three times maximal during a full rotation. This analysis allows to interpret distance and direction of the three high-anisotropy tubes in Figure 2.8b and 2.8c in terms of width and orientation of the magnetization swirl. Thus, Figure 2.8 reveals that although the general structure of the swirl is nearly constant, there is a decrease of swirl diameter and also a slight distortion of the vortex orientation towards the particle surface. These effects are hardly visible in direct images of the three-dimensional magnetization structure.

Conclusions

A new micromagnetic algorithm is used to calculate stable and meta-stable magnetization structures of small naturally shaped particles in dependence of grain size. The results for octahedral magnetite indicate that the transition size from SD to vortex states is about the same as previously found for cubic particles. However, meta-stable SD particles can exist at larger grain sizes which implies that typical PSD effects like the peak in TRM /ARM ratio observed by Dunlop and Argyle (1997) can occur up to grain sizes of 300 nm even in equi-dimensional particles. For magnetosomes, the results obtained deviate considerably from previous estimates based on rectangular particles and show that all naturally occuring magnetosomes can sustain an - at least - meta-stable SD state. Additional support by positive interaction within a magnetosome chain is therefore not essential for the existence of the SD state. This result again confirms the efficiency of biomineralization in magnetotactic bacteria and gives tight constraints on the geometry of biogenic magnetite from magnetotactic bacteria.

Acknowledgements
Detailed and constructive reviews by A. Muxworthy and W. Williams considerably improved the manuscript. This work was supported by DFG grant 793 Fa408/2.

3 DRM and PDRM acquisition

Depositional and post-depositional remanent magnetization

The acronym DRM is usually defined as 'detrital remanent magnetization' which in some textbooks includes depositional remanent magnetization and post-depositional remanent magnetization, whilst in others it is used as a synonym for 'depositional remanent magnetization'. Here, factors influencing depositional remanent magnetization and post-depositional remanent magnetization will be investigated separately and should be distinguished. Therefore, in the following, the acronym DRM will be used for the 'depositional' part of the remanence.
Theoretical models of Collinson (1965) and Stacey (1972) predict that magnetic grains settling through the water column only need a few centimeters to obtain maximal DRM intensity. During natural sedimentation processes, not all magnetic grains are aligned perfectly with the field. Turbulent Water, water currents or particle aggregation might disturb this alignment. Moreover, elongated grains tend to sink with their long axis perpendicular to the axis of descent, thus biasing the recorded magnetization. At the sediment-water interface, magnetic and non-magnetic grains settle in the porous space of the sediment. When magnetic grains are deposited but not yet consolidated, the DRM is not fixed. Bioturbation or mechanical slumping can still alter direction and intensity of the magnetization. Nevertheless, the first few centimeters of the sediment column often display a uniform magnetization thus indicating that a mechanism of post-depositional remanent magnetization (PDRM) acquisition is acting (Irving and Major 1964). After deposition, the sediment experiences chemical alteration, compaction due to the overburden of later sediments, and dewatering. All these processes fix parts of the sediment's magnetization. Still, fractions of this magnetization in compacted sediments may later be altered by post-depositional processes. Bioturbation and even compaction itself can set magnetic particles free, thus allowing them to improve their alignment with the external magnetic field (Otofuji and Sasajima 1981a). When the water content falls below a certain threshold and physical contact prevents the magnetic particles from moving and aligning with the external field, the PDRM is said to be 'locked-in'.

Processes which influence DRM and PDRM

Magnetic grains exposed to a magnetic field experience a torque which tries to align them with the field. This aligning field can be of external origin or an interaction field generated by surrounding magnetic particles. Magnetic dipole interaction tends to align magnetic particles antiparallel to each other, Fig. 3.1. Since the magnetic field strength of the interaction field decreases with the cube of the particles' distance, magnetic particle interaction only plays a role in sediment slurries with high concentrations of magnetic particles. The external magnetic field usually has a larger influence on the magnetic

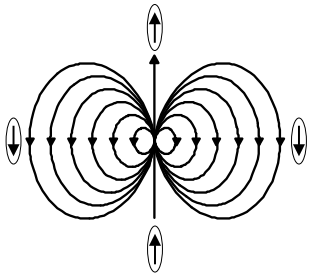

Figure 3.1: Magnetic field of a dipole. Parallel alignment of dipoles is possible as long as the interacting particle form chains. Due to the magnetic field of the dipole, antiparallel alignment can take place not only on a straight line but in a plane. This explains why a dipolar field due favors anti-parallel alignment of particles.

particle alignment.

In the water column, viscous drag or turbulence sometimes oppose rotation caused by the magnetic torque and after deposition, friction obstructs the particles' aligning to the field. Even in the pore space of the sediment, randomizing processes like Brownian motion act against the alignment of particles.

When particles are close to each other, short range electrostatic forces become important and influence their aggregation. The strength of these van der Waals forces depends on particle size as well as particle separation and material.

Like DRM acquisition, PDRM acquisition is also influenced by particle shape. At the sediment-water interface, particle shape influences the settling process in the pore space. During compaction due to sedimentation, elongated particles are more easily rotated than spherical particles. It is not always possible to distinguish between DRM and PDRM influencing processes. Many processes that influence the DRM can also act in the pore space of the sediment thus affecting the PDRM.

Numerical models

Here, numerical models are applied in order to improve our understanding of processes controlling DRM and PDRM. These models are used to independently investigate the importance of different remanence controlling factors. The first article in this section applies a discrete element method (DEM) to study the influence of particle shape, external field strength and compaction on the level of acquired magnetization. Additionally, the DEM model is used to assess the influence of van der Waals forces upon sediment structure. The second article considers the effect of particle-particle interaction and Brownian motion upon DRM acquisition based on experimental and numerical data. A third and fourth manuscript again use the DEM model to assess the influence of van der Waals forces upon DRM acquisition and to estimate the effect of inclination shallowing on the interpretation of paleomagnetic data.

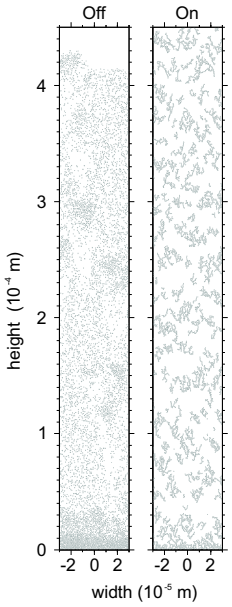

Figure 3.2: The influence of particle aggregation in the water column due to van der Waals forces is investigated using the DEM. On the left, the sediment settles without van der Waals forces. On the right, van der Waals forces lead to particle aggregation in the water column.

Discrete element modelling provides the opportunity of modelling large physically interacting particle assemblages. This makes it a powerful tool for modelling magnetic particle alignment in sediments.

While modelling translational and rotational motion of a non-interacting particle assembly is a simple task, an interacting assemblage is far more difficult to handle. A commercial two dimensional DEM is employed to provide a numerical description of an interacting model granulate material subject to a variety of different forces. The model material's history is calculated in an iterative manner, resolving forces and torques for each time step based on

Newton's second law of motion and the force-displacement law. From forces and torques at the current time step, new positions, velocities and accelerations are determined for the subsequent time step. Fig. 3.2 demonstrates the influence of particle aggregation on the sediment fabric as resulting from DEM calculations.

Discrete element modelling of post-depositional remanent magnetization acquisition in aquatic sediments

A. Witt, D. Heslop, T. von Dobeneck, K. Huhn and K. Fabian

Universität Bremen, FB Geowissenschaften, Postfach 330440, 28334 Bremen, Germany, Tel. +49-421-218-3933, Fax +49-421-218-7008, Email witt@informatik.uni-bremen.de

Abstract

The physical microscale processes by which sediments acquire a post-depositional remanent magnetization (PDRM) defy direct observational investigation and are therefore still poorly understood. We present a series of two-dimensional numerical models based on the discrete element method which are used to investigate the influence of magnetic particle shape, compaction and van der Waals forces upon post-depositional remanence acquisition. The initial models simulate the exposure of spherical and elongated magnetic particles to an external field at varying depths in a sediment column. It is found that spherical particles located just below the sediment-water interface are able to rotate into close alignment with the external magnetic field, whilst the orientation of elongated particles is physically locked by the sediment matrix. At increased overlying pressures, corresponding to greater sediment depths, grain shape loses its influence and the orientation of spherical particles becomes locked. For grain sizes typical of those found in ocean sediments, van der Waals forces produce particle flocs in the water column and highly porous structures below the sediment-water interface. The production of such an open sediment fabric indicates that van der Waals forces play an important role in the formation of voids in which magnetic particles can rotate freely. Finally, it is found that the effect of rotational Brownian motion on the efficiency of magnetic grain alignment with the ambient geomagnetic conditions is negligible except under extremely weak field conditions.

Keywords: rock magnetism; micromagnetics; magnetosomes

Submitted to JGR

Introduction

Marine sediments continuously record directional and intensity changes in the earth's magnetic field and their use in the reconstruction of the paleofield is a well established method in the Earth sciences. The physical mechanisms by which sediments form a remanence is still under debate (Tauxe 1993). Previous studies have demonstrated that a stable palaeomagnetic signal is acquired below rather than at the sediment-water interface. Tauxe *et al.* (1996) concluded that a stable natural remanent magnetization (NRM) is formed within the first few centimeters of the sediment. Greater signal lock-in depths have been reported frequently, (e.g. deMenocal *et al.* (1990); Bleil and von Dobeneck (1999); Channel and Guyodo (2004)) and it is apparent that the depth and width of the lock-in zone is a site-dependent property. Such a delay in remanence acquisition is understandable because the upper layers of marine sediments are highly porous and unconsolidated, thus allowing the rotation of deposited magnetic particles into alignment with the Earth's magnetic field. Recently, Katari and Bloxham (2001) theoretically investigated the influence of particle aggregation in the water column upon the formation of NRM. The work of Katari and Bloxham (2001) raises the hypothesis that flocculation by van der Waals forces plays an important role in controlling palaeomagnetic signal intensity even before sediment particles are deposited.
The environmentally controlled vertical distribution of PDRM relevant physical processes is also of interest in the context of relative paleointensity studies. Each sedimentary factor influencing the degree of magnetic particle alignment will bias and modulate the signal, which is ultimately ascribed to the intensity variation of the past geomagnetic field. The issue of varying interactions of the sediment matrix and magnetic carriers has been addressed previously and may explain spurious climatic signals in paleofield records (Lu *et al.* 1990).
In the past, investigations of the properties and mechanisms of post-depositional remanent magnetization (PDRM) were mainly based on laboratory resedimentation and consolidation experiments (Blow and Hamilton 1978; Kent 1973; Levi and Banerjee 1990) or continuum-theoretical description (Shcherbakov and Shcherbakova 1987). The summaries of a number of investigations are reported in review articles (Verosub 1977; Tauxe 1993). These experiments provided some empirical understanding of the influence of grain size, lithology and consolidation state but left the relevant microscale processes of mobilization, orientation and fixation of the magnetic carriers unknown. To investigate some general mechanisms of particle alignment with an external magnetic field after burial, we employ a collection of two-dimensional numerical models based on deterministic particle arrangements.
In the first set of models, the influence of rotational Brownian motion on the alignment of magnetic particles in the water column is investigated. The grains possess magnetizations corresponding to thermoremanent magnetizations acquired in the Earth's magnetic field and are free to rotate. Assemblages of physically interacting particles can be represented by the discrete element method (DEM) (Cundall and Strack 1979) and as such it is suitable for studying the governing dynamics of NRM formation in the upper layers of aquatic sediments. The controlling roles of particle shape and compaction are considered in the process of magnetic signal formation below the sediment-water interface using a DEM model. As a final step we investigate the influence of van der Waals forces on particle behavior during and after floc formation and the implications for modelled PDRM.

The results of this modelling give independent insight into the relevance of different remanence acquisition processes which might extend to real sediments.

The effect of rotational Brownian motion

According to Stacey (1972), Brownian motion acts as a misaligning process which could explain the field dependance of detrital remanences. To test if the influence of rotational Brownian motion is significant on the alignment of magnetic particles in the earth's magnetic field, we present the following simple model before discussing the DEM simulations.
Brownian motion is usually represented as a purely statistical process. For the alignment of magnetic grains with the Earth's field the rotational rather than translational component of Brownian motion is of primary interest. The theory of Debye (1929) assumes that rotational Brownian motion is random with no preferred direction. Given these assumptions it is possible to calculate the so-called *Debye relaxation time*, τ_0, which corresponds to the time required for the magnetization of a collection of particles aligned with an applied field to decay to half of its initial value once the field is switched off. The relaxation time is given by:

$$\tau_0 = \frac{3V\eta}{kT} \tag{3.1}$$

where V is the volume of the particle, η is the dynamic viscosity of the carrier liquid, T is the absolute temperature and k is Boltzmann's constant.
The alignment of a spherical magnetic particle within an applied field whilst held in a viscous medium can be described by:

$$I\frac{d^2\theta}{dt^2} + 8\pi r^3\eta\frac{d\theta}{dt} + mB\sin\theta = 0 \tag{3.2}$$

where I is the moment of inertia of the particle and r the particle's radius. The magnetic moment of the particle is given by m, the applied field is B and θ is the angle which separates them. We performed *MATLAB* based simulations to determine the time required for different sized magnetic grains orientated at various starting angles to align with an applied field in water. The inbuilt function *ode45* was used to solve numerically for $\theta(t)$ and each particle was assumed to commence its rotation from rest. The magnetizations of the model grains were size dependant according to the relationship (Dunlop and Özdemir 1997):

$$M = 0.9 \times d^{-1} \tag{3.3}$$

where d is the diameter of the particle in μm and M has units of kA/m.

Results

The results from the discussed models of Brownian motion for fields of 50 (the approximate value of the earth's modern field strength), 5 and 0.5 μT and model particles with radii of 35,

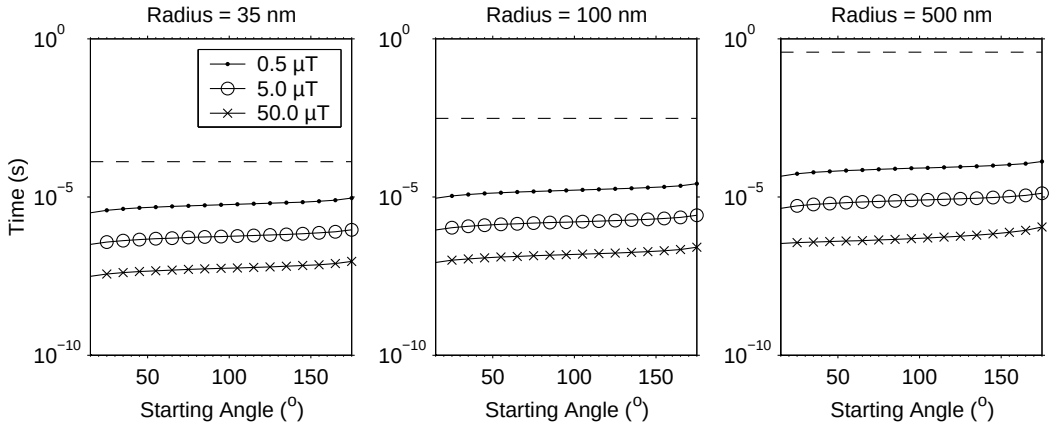

Figure 3.3: Times required for different size model particles carrying realistic TRMs to move from rest at a given angle into alignment with the applied field. The hatched lines represent the Debye relaxation time, τ_0, for the given particle size suspended in water at temperature of 300 K.

100 and 500 nm are shown in Figure 3.3. A number of features of the model results match those expected from theory. First, the influence of rotational Brownian motion decreases for larger particles resulting in increased relaxation times. Second, the time required for grain alignment increases with greater starting angles and is more rapid for higher field strengths. Comparing the periods calculated for different size particles to rotate into equilibrium positions it is apparent that the time required increases as particle size increases.
The most important aspect of the presented models is the comparison between the times required for magnetic alignment of the particles and the Debye relaxation time. The alignment times are orders of magnitude shorter than the Debye relaxation time, indicating that for typical magnetic particle sizes the effects of rotational Brownian motion are insignificant even in very weak fields. This point is emphasized by a further calculation for a particle with a radius of 500 nm starting from an orientation of 90^o to the applied field. For such a particle, the field strength at which the required rotation time and the Debye relaxation time are the same is an extremely low value of $\sim$0.1 nT. One limitation of the Debye relaxation time is that it does not consider the effects of the particle inertia. Further calculations have shown that the effects of particle inertia act to increase relaxation time, thus indicating a reduced effect from Brownian motion, (Fannin *et al.* 1995).
Because of the negligible effects of rotational Brownian motion on the alignment of magnetic particles with an external field, we opted to remove the consideration of Brownian motion from the following DEM model, thus increasing the computational efficiency of the simulation.

The Discrete Element Model

Two separate series of DEM simulations where used to investigate various microscale processes controlling PDRM acquisition. The first set considered the influence of particle shape, compaction and external field strength, whilst the second set explored the role of van der

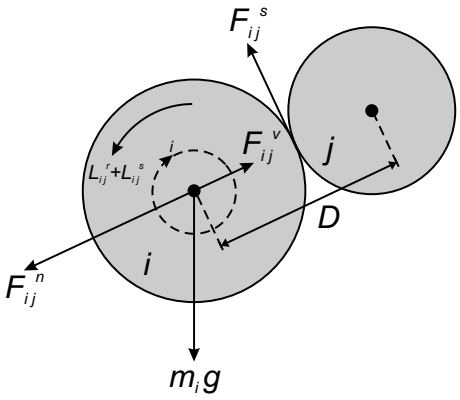

Figure 3.4: Schematic illustration of the forces acting on particle i, which is in contact with particle j, based on Yang *et al.* (2000). I_i is the moment of inertia of particle i and ω_i is its rotational velocity. The normal contact force and shear contact force are given by $\mathbf{F}^n_{ij}$, $\mathbf{F}^s_{ij}$, whilst the torques due to the shear force and rolling friction are $\mathbf{L}^s_{ij}$ and $\mathbf{L}^r_{ij}$ respectively. The force of gravity acting on particle i is given by $m_i g$ and the van der Waals force due to the proximity of particle j is $\mathbf{F}^v_{ij}$, where the center to center separation is D.

Waals forces.

The motion of every suspended sediment particle can be described by translational and rotational components according to Newton's second law of motion. It is therefore simple to calculate the motion of a collection of model particles as long as they do not interact with each other. However, in natural sediments most particles have several contacts with their neighbors which must be accounted for.

The DEM provides a numerical description of the behavior of a model granulate material subject to a variety of different forces. In the case of the model sediment behavior, gravity, particle-particle contacts, friction, magnetic torque, van der Waals forces and overlying pressure are all taken into consideration, Fig. 3.4. The history of a collection of model particles is calculated in an iterative manner. For each time step, the forces and torques acting on the individual particles are resolved and new positions, velocities and accelerations are determined for the subsequent time step. Based on the integration of Newton's second law of motion, the movement of a particle i of radius r_i and mass m_i can be computed for a time step by:

$$m_i \frac{d\mathbf{v}_i}{dt} = \sum_i (\mathbf{F}^n_{ij} + \mathbf{F}^s_{ij} + \mathbf{F}^v_{ij}) + m_i \mathbf{g} \tag{3.4}$$

and

$$I_i \frac{d\omega_i}{dt} = \sum_i (\mathbf{R}_i \times \mathbf{F}^s_{ij} - \mu_r r_i |\mathbf{F}^n_{ij}| \, \hat{\omega}_i) + \mathbf{L}_{ij} \tag{3.5}$$

$\mathbf{v}_i$, ω_i and I_i are, respectively, the translational and angular velocities and the moment of inertia of particle i; μ_r is the coefficient of rolling friction, $\hat{\omega}_i = \omega_i / |\omega_i|$, Fig. 3.4. The normal contact force, shear contact force, magnetic torque and van der Waals force are given by $\mathbf{F}^n_{ij}$, $\mathbf{F}^s_{ij}$, $\mathbf{L}_{ij}$ and $\mathbf{F}^v_{ij}$ (Yang and Yu 2003). $\mathbf{R}_i$ denotes a vector pointing from one particle's center to the contact point with magnitude r_i. Contacts between particles are represented using the linear viscoelastic model of Cundall (1987). The effects of friction are included in

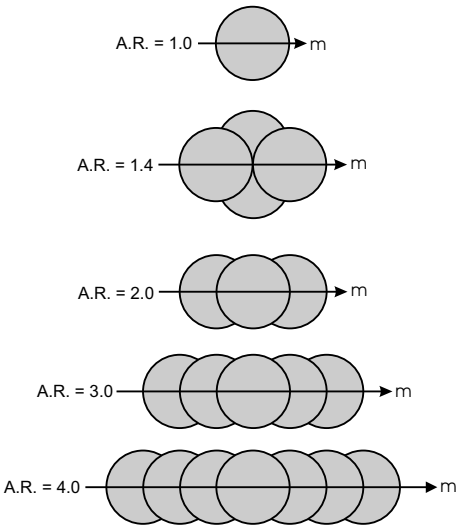

Figure 3.5: In order to include non-spherical particles in the DEM model, spherical particles are statically combined to form clumps with different aspect ratios (A.R.). The magnetization that is assigned to a clump is orientated along its long axis.

the maximum allowable shear contact force according to Coulomb's law (Cundall 1987). By the use of an additional term in the equations of motion it is possible to linearly damp the particles' accelerations in order to obtain an energy dissipation for motion in water.
As an advantage of DEM over similar numerical methods, the time step selected for calculating the particles' motion is so small that within one iteration the motion of a single particle in the model will only effect its immediate neighbors and not the whole assemblage. This processes reduces the number of required computations from order n^2 to order n.
Magnetostatic interactions are not considered in the model since for N particles this would require the evaluation of N^2 differential equations. The assumption of no magnetostatic interactions is justified by the supposition that in typical marine sediments there are so few magnetic particles that one of them is hardly influenced by any other magnetic particles. The unrealistically high proportion of magnetic particles in the presented models serves simply to improve statistics concerning average particle behavior.

All of the presented DEM models were created using the PFC2D (*Particle Flow Code in 2 Dimensions*) software from HCItasca. The program acts as a computation engine which solves user-designed simulations. The PFC2D software only allows simulations involving spheres or disks, but particles can be statically combined to produce other simple forms (Fig. 3.5). The positions of the modelled particles are restricted to the confines of a predefined container which is constructed from *walls* with the same properties as the particles themselves (see later diagrams).

Table 3.1: parameters for the DEM model

Parameter	Value
Radius of magnetic particles	$50 - 100\ nm$
Radius of non-magnetic particles	$100\ nm$
Number of particles	≈ 1000
Coefficient friction	0.6
Particle density	$2500\ kg/m^3$
Young's modulus	$10^8\ Pa$

Limitations of the simulations

When constructing a DEM simulation it is necessary to define a number of properties of the model system such as the density of the particles, the friction between particles, etc (Table 3.1). We have attempted to use realistic values for each of these quantities, however a number of them are poorly defined for natural systems. Therefore, although it is possible to simulate the basic processes which take place in fine grained sediments it would be premature to attempt the formulation of quantitative relationships based on the model results.
Some further limitations result from considering a two-dimensional rather than a three-dimensional system. In a two-dimensional system porosities can be calculated as the ratio of the total void area to the total area. The use of this value is however somewhat limited in the two-dimensional model because it is assumed that the centroids of all the particles are aligned on a single plane. This results in calculation of reduced porosities for two-dimensional compared to three-dimensional systems. This point is demonstrated by the fact that the most efficient regular packing of uniform spheres has a volume based porosity of 25.95 %, whilst the most efficient regular packing of uniform circles has an area based porosity of 9.31 % (Deresiewicz 1958). A second limitation of the two-dimensional model is that percolation (the process of small particles migrating through and filling the void space of a system of larger particles) cannot be properly represented, leading to larger voids within the sediment and increases in the area-based porosities.

The effect of particle shape and compaction

For the first numerical experiments, the model magnetic particle size is held constant in the range of single domain magnetite grains (50 nm to 100 nm), while the non-magnetic sediment grains are assigned a radius of 100 nm (Table 3.1). The reason for selecting such small non-magnetic grains in the model comes from the limitation of only being able to work with particles based on spheres. The voids between silt sized spheres will always be large enough to allow free rotation of much smaller magnetic grains. Therefore, to represent irregular grain shapes which could lock magnetic particles we work with a very fine non-magnetic model matrix. The approach of small non-magnetic particles, rather than working with large irregular particles constructed from spheres, substantially reduces computation time.

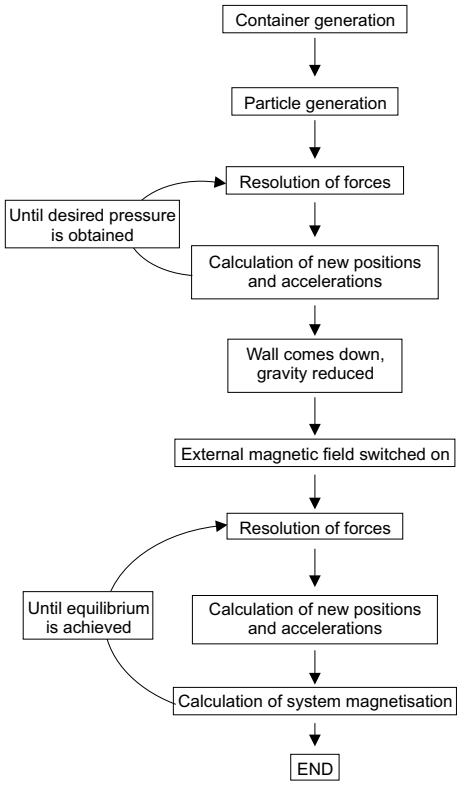

Figure 3.6: A flowchart to illustrate the sequence of operations performed in the DEM simulation of the post-depositional realignment of magnetic particles.

The individual magnetic particles are assigned a magnetization corresponding to a realistic thermoremanence (Dunlop 1990b) and a random starting orientation. Each model consists of approximately 1000 particles, ∼20% of which are magnetic with predefined aspect ratios. The sequence which the model follows is most efficiently represented using the flowchart in Figure 3.6. The initial state of the model consists of particles positioned at uniformly distributed random locations throughout the area of a container with width of 5μm and height of 7μm, (Figure 3.7a). The model particles settle under the influence of gravity with zero external magnetic field. In order to generate model sediment configurations which represent systems with different overlying pressures, gravity must be increased during the settling phase of the simulation. As soon as the particles have sedimented at the bottom of the model box, an upper wall moves downwards and is positioned at the sediment surface to maintain the overlying pressure. When the top wall has arrived at its final position, gravity is gradually decreased until it equals the normal value of 9.81 N/kg. The gradual decrease in gravity, the absence of an external magnetic field and the effect of the top wall produce a model sediment exposed to a known overlying pressure and with no preferential alignment of the magnetic grains, Figure 3.7b. In this way, different depths within sediment cores can be simulated and the model of PDRM formation can be studied without having to consider the contribution from an existing detrital remanent magnetization. Unfortunately, because of the previously discussed limitations of a two-dimensional model the values chosen for the

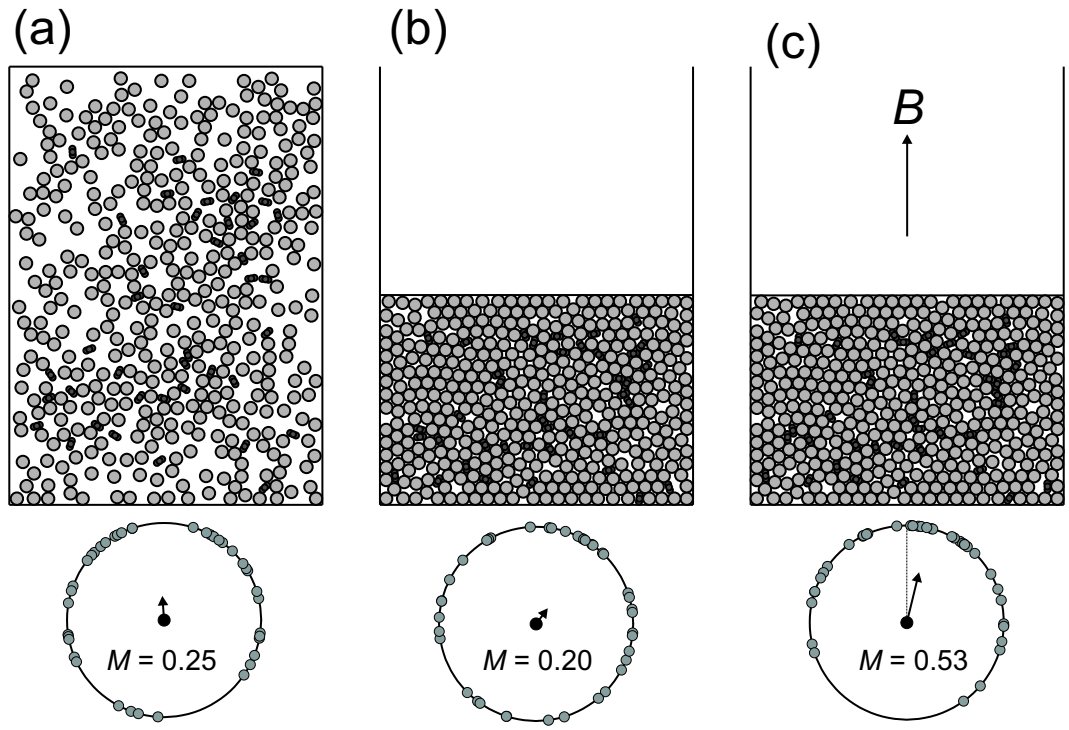

Figure 3.7: Stages of the DEM model to study post-depositional realignment of magnetic grains. Plotted below each illustration of the model container is a circular representation of the distribution of the orientation angles of the magnetic particles contained within the system. The arrow at the center of each circle represents both the direction and the magnitude of the magnetization of the whole system. ***(a)*** The sediment particles are created at uniformly distributed random locations within the four walls of the container. The non-magnetic particles are light grey spheres, whilst the magnetic grains are smaller dark gray particles with an aspect ratio of 3. ***(b)*** The sediment particles descend to the base of the container under the influence of gravity. Once deposition is complete, the top wall of the container is moved downwards to apply an overlying pressure of known strength to the sediment pile. ***(c)*** Whilst the overlying pressure is maintained an external field, B, with a direction pointing vertically upwards is switched on and the realignment of the magnetic particles can be determined. The dashed line in the final circular plot shows the axis of the external magnetic field.

overlying pressure cannot be easily converted into true core depths for real sediments. Instead, the model pressures are chosen in a way to best represent the full range of magnetic particle behavior in two dimensions, ranging from completely lock into position to being able to rotate freely.

After the settling portion of the model is complete, an external magnetic field is invoked and a magnetic torque can be applied to the particles. The orientation of each of the magnetic particles can then be assessed to determine the overall magnetization of the model system, Figure 3.7c. Because the models are constructed from a relatively small number of particles, the PDRM acquisition curves of individual runs are quite variable and cannot necessarily be considered to be fully representative of the true behavior of the system. Figure 3.8, plots the modelled magnetization from the sediment configuration shown in Figure 3.7. Although the final magnetization reaches a steady equilibrium value it was found that the absolute value could vary depending on the starting positions of the model particles. To overcome this

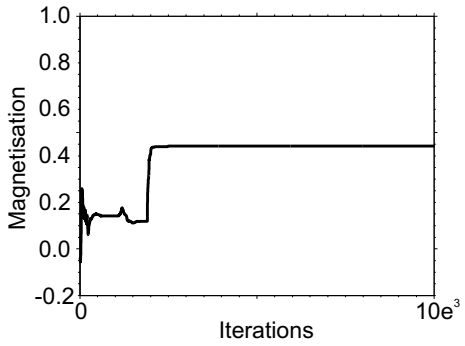

Figure 3.8: PDRM acquisition results for the sediment configuration shown in Figure 3.7. The steady magnetization at the end of the model is assumed to represent the equilibrium magnetization of the system.

problem each simulation was repeated a total of 50 times with different starting positions for the individual particles. The magnetization curves from each series of simulations were stacked to provide an arithmetic mean and the variability between the individual runs was assessed by the calculation of the standard deviation.

Results

The magnetic torque experienced by a particle has to act against forces imposed by the surrounding sediment. We hypothesize that particle shape plays a major role in the amount of remanence a sediment can acquire since it seems to be reasonable to assume that it is far harder to fix a smooth spherical particle than to fix an elongated or irregular particle.
The first set of DEM simulations consider the post-depositional realignment of spherical particles (Fig. 3.9). At low pressures the final magnetization of the model system is clearly dependant on the magnitude of the external field, however, saturation is effectively achieved at fields below 50 μT. This result is not surprising because in the model spherical particles can rotate under the influence of a magnetic torque without having to restructure the other particles in their local surroundings. For spherical particles the main resistance to rotational motion is in the form of friction produced by the normal forces of particle-particle contacts. It is apparent from the results that at low pressures the effects of friction in the model can be overcome by a relatively weak magnetic torque. As the pressure is increased to represent burial of the particles at a greater depth, the friction acting on the magnetic particles also increases. The effect of this overlying burden is to produce a level of friction that is sufficient to restrict the rotation of the magnetic spheres and a saturation magnetization is not achieved in the model even for fields of 100 μT.
It is also important to note the implications of the standard deviation calculated for each model stack. For the low pressure models shown in Figure 3.9, the standard deviation of the magnetization decreases as the field strength is increased. It is therefore apparent that the number of sediment configurations in which a spherical particle can become locked increases as the external field is reduced, thus producing a greater variety of equilibrium magnetizations in the individual model results.

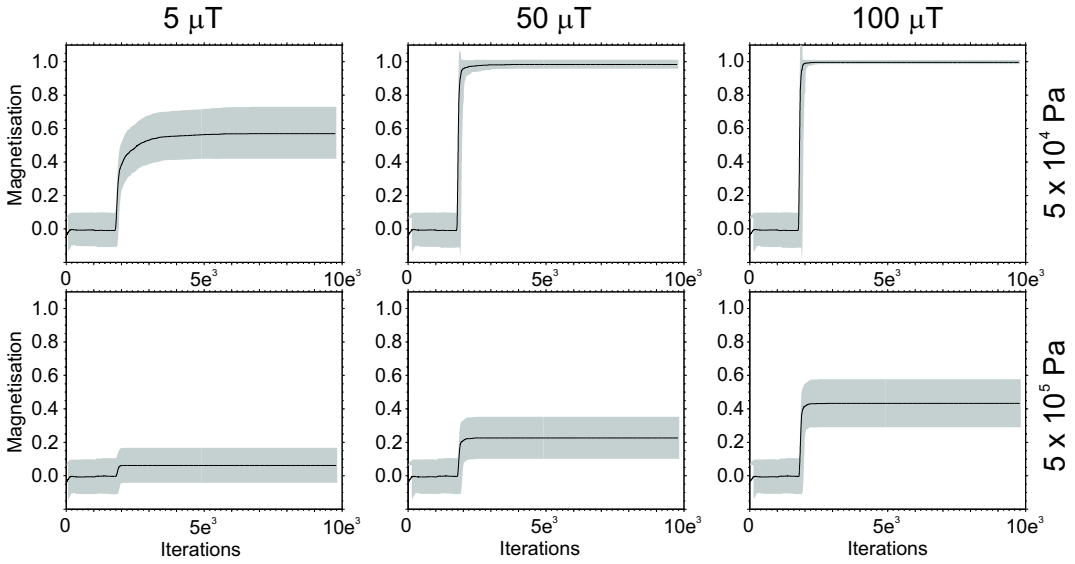

Figure 3.9: PDRM acquisition results for spherical particles. Each row represents one overlying pressure, each column one external field value. Throughout the figure, fields and pressures increase. The black line in each plot represents the intensity of the remanence (where a value of 1 is perfect alignment with the field). The mean value is obtained by stacking 50 model runs. The grey area surrounding the curve is the standard deviation of the runs. The low magnetization values at the start of each curve represent the settling portion of the model in the absence of an external magnetic field. Once a field is applied, typically after ∼1800 iterations, the magnetization of the systems is seen to increase.

Spherical particles cannot be considered as realistic representatives of natural sediments. Therefore a further series of models was calculated to investigate the PDRM behavior of magnetic grains with aspect ratios greater than 1. Elongated magnetic particles differ from spherical ones because they must rearrange their immediate neighbors in order to successfully rotate into alignment with an external field unless they are located within large sediment voids. Therefore elongated magnetic grains are not only restrained by friction but also the resistance of the surrounding sediment to reorganization. The results presented in Figure 3.10 show simulations for particles with increasing aspect ratios under constant field ($50\ \mu T$) and constant pressure conditions ($5 \cdot 10^4 Pa$). The equilibrium states of the modelled systems

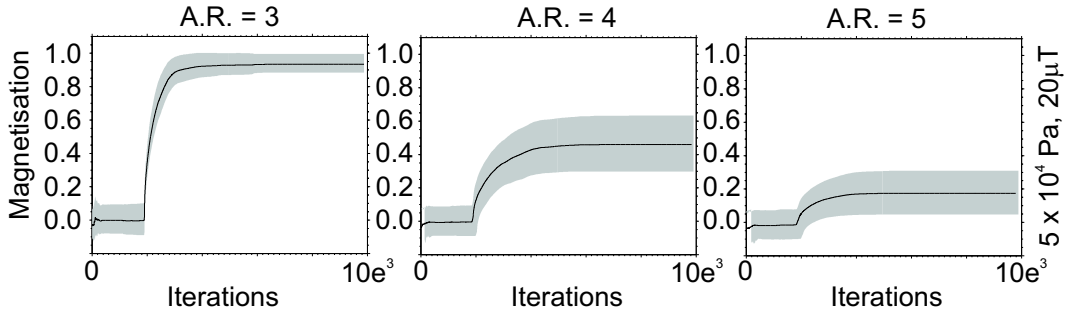

Figure 3.10: Different elongations subject to the same external magnetic field and the same overlying pressure.

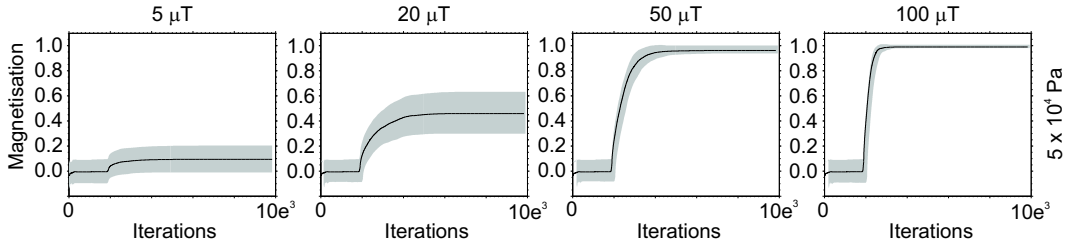

Figure 3.11: The influence of external magnetic field strength upon the quality of alignment for the same particle shape and the same overlying pressure.

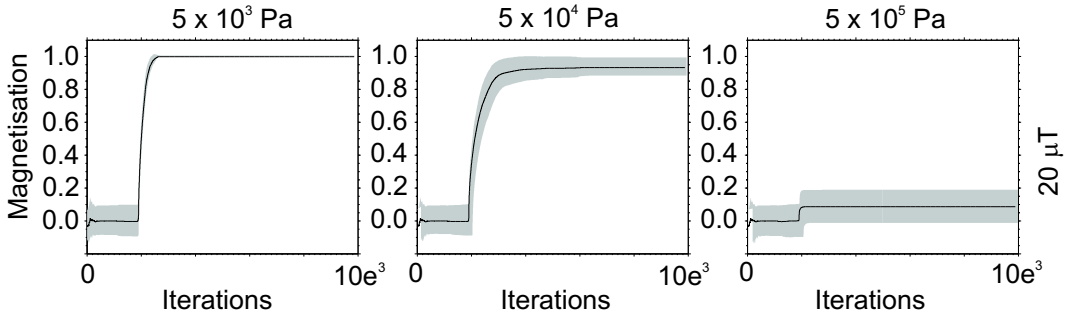

Figure 3.12: Different pressures acting on particles of the same shape subject to the same external magnetic field

show a trend of decreasing magnetization with increasing magnetic particle aspect ratio. Such a result is expected when it is considered that a more elongated particle must describe a larger circle during its rotation and thus it is required to reorganize a greater sediment volume. In the model the effect of particle elongation appears to be quite dramatic with a decrease in the PDRM realignment from ~ 0.9 to ~ 0.15 as the aspect ratio increases from 2 to 4

The remaining models consider the effects of external field strength and overlying pressure on the PDRM of elongated magnetic particles (A.R. = 2). As the strength of the external magnetic field increases, the magnetic torques of the particles become sufficiently large to restructure the sediment matrix. This restructuring process results in a more efficient PDRM realignment, Figure 3.11. Considering the effects of pressure the PDRM alignment can go from almost perfect at low pressures to almost zero at high pressures. When the pressure reaches a certain limit ($5 \cdot 10^5 Pa$), the acquisition of remanence in the model occurs almost instantly where free movement of the particles is possible (Figure 3.12). However, the sediment is sufficiently compacted that once rotating particles are obstructed by the non-magnetic matrix they become locked.

The results of all of the models are compiled in Figure 3.13. For the smallest overlying pressure and less elongated particles the magnetization is nearly saturated, therefore almost no difference can be seen between spherical particles and the particles with high aspect ratios. In the upper layers of sediment, modelled with low pressures, the particles align almost perfectly with the magnetic field. Since natural PDRMs are typically far below this saturation value, it would appear that randomizing processes influence the particles' alignment in nat-

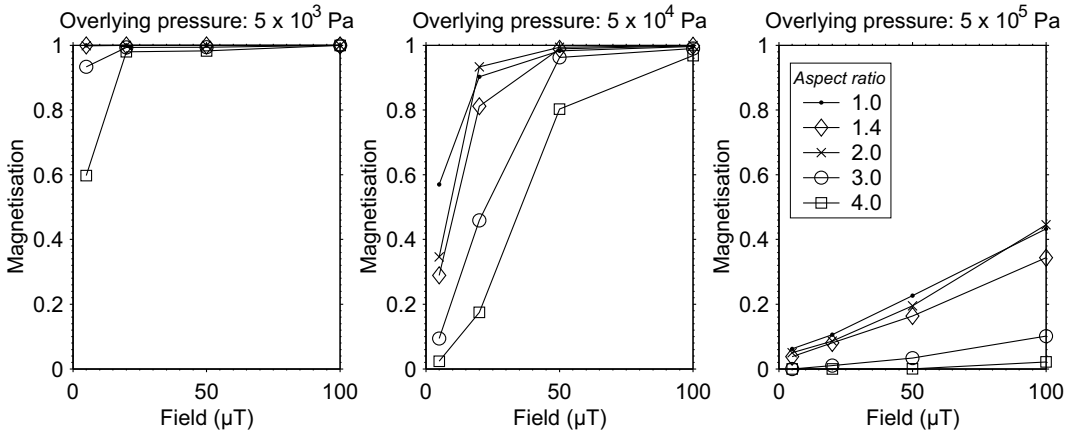

Figure 3.13: Scatter-plots of acquired model magnetization as a function of grain shape, external magnetic field and overlying pressure. The overlying pressure increases from the left to the right picture.

ural systems while overlying sediment accumulates. Such processes could be the rotation of grains due to bioturbation, dewatering, compaction and early diagenesis of the sedimentary matrix. For the highest pressures modelled and fields typical of the Earth's magnetic field, the acquired magnetization is less than 30% and resembles values reported for natural and redeposited sediments (Barton *et al.* 1980).

The effect of van der Waals forces

During sedimentation, the influence of van der Waals forces upon particle aggregation can not be ignored. Van der Waals forces are attractive electrostatic short range forces. We use a numerical representation of van der Waals forces for particles that are large compared to the distance separating them (Hamaker 1937). With:

$$E = -\frac{A}{6}\left[\frac{d_1 d_2/2}{D^2 - (\frac{d_1+d_2}{2})^2} + \frac{d_1+d_2}{D^2 - (\frac{d_1-d_2}{2})^2} + \ln\frac{D^2 - (\frac{d_1+d_2}{2})^2}{D^2 - (\frac{d_1-d_2}{2})^2}\right] \tag{3.6}$$

and

$$\mathbf{F} = -\nabla E \tag{3.7}$$

where

$$D = \frac{d_1+d_2}{2} + s \tag{3.8}$$

one is able to obtain an approximation for van der Waals forces, where A is the material dependent Hamaker constant (set to $10^{-19}J$ for all models), d is the diameters of the particles and s their separation.

As can be seen from equation 3.6, van der Waals forces are particle-particle interactions. A system with N particles requires the evaluation of N^2 equations in order to assess fully the

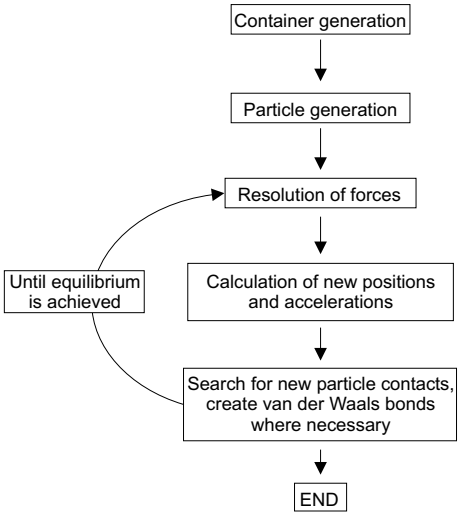

Figure 3.14: A flowchart to illustrate the sequence of operations performed in the DEM simulation of particles sedimenting in the presence of van der Waals forces.

van der Waals forces. For large systems such computations quickly become cumbersome. Since van der Waals force decreases with the 7^{th} power of the particles' separation, it was only calculated in the model for particles that actually come into contact and is simulated by assigning a contact bond to these particles which possesses a strength equivalent to the van der Waals force between them. Because of the zero in the denominator for particles that come into contact, a minimum distance between the particles of 4 Ångstrom is assumed in the calculation of the bond strength (Hamaker 1937).
The initial state of the DEM model used to investigate van der Waals forces consisted of 10^4 spheres with lognormally distributed radii, positioned at random locations in a container with dimensions 1000 (height) by 200 (width) times the mean particle radius. After creation of the model assemblage, a gravitational force was applied and the particles were allowed to settle with the effect of van der Waals forces switched either on or off. Each simulation was terminated when the model assemblage reached equilibrium and the particles became static (Figure 3.14).
Because van der Waals forces have a normal but no shear component, their only influence on the orientation of spherical particles is due to rolling friction. To demonstrate the relatively limited direct effect of van der Waals forces on the PDRM of an assemblage of spherical particles, the number of contacting neighbors required to produce a level of rolling friction sufficient to lock the orientation of a magnetic particle in a given field are calculated (the so-called *locking coordination*). The resistance to rotation of a particle is obtained as the product of the normal force from the van der Waals bonds and the coefficient of rolling friction (set as 0.01 for all models). A magnetic particle with diameter of 150 nm is selected as the basis for the model and the required *locking-coordination* of monodispered spheres of a given size is determined, Figure 3.15.
For a 50 μT field it is calculated that the *locking-coordination* ranges from ∼70 for medium sized sand particles to ∼180 for clay particles. It is clear that such high coordination numbers

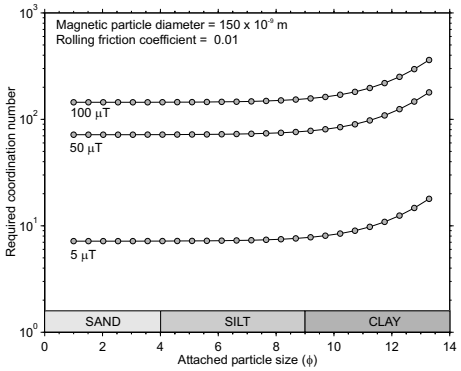

Figure 3.15: The number of spherical particles calculated to provide sufficient rolling friction to stop a 150 nm magnetic particle aligning with an external field is presented in terms of coordination numbers. Model results are shown for coordinating particles with sizes ranging from 1 - 13 ϕ (Udden & Wentworth scale, see text for further explanation) and three different field strengths.

would not be possible in real systems because the magnetic particle is not of a sufficient size to accommodate such a large number of contacting neighbors. In the case of a weak field, 5 μT, the calculated *locking-coordination* has a minimum value of 7 for sand particles which would also appear to be a physically impossible configuration when the relative sizes of the magnetic and sand particles are considered. These results demonstrate the limitations of employing only spherical particles in the model where van der Waals forces only effect particle alignment via rolling friction. In the case of non-spherical particles, we assume that van der Waals forces will be responsible for attaching magnetic grains to larger particle aggregates. In order for a non-spherical particle to rotate it must also turn the particles to which it is attached. Thus the inertia of the aggregate becomes critical to resisting the alignment of the magnetic particle with the external field. This process is similar to the theory of Katari and Bloxham (2001), who considered the effects of particle aggregation on detrital remanent magnetisation formation. The calculation of van der Waals forces for irregular particles is not a trivial task (Tadmor 2001) and is currently under development for the DEM method. Due to the limitations of modelling with spherical particles, we only consider the influence of van der Waals forces on sedimentary fabric and do not include magnetic particles in the simulation.

Coordination numbers

Because of the ambiguities of porosities in the representation of two-dimensional systems we employ the concept of *coordination numbers* to describe the results of our models. The coordination number of any particle is given by the number contacts which exist between it and its neighbors. Coordination numbers are typically high for well packed sediments, however as the packing becomes more open, for example chain-like structures, coordination numbers will reduce to values of around two, where each particle can be supported by one particle and at the same time supports another.
A visual comparison of the models calculated for uniform spheres with a diameter of $\phi = 10.0$ on the Udden & Wentworth scale ($\phi = -\log_2 S$, where S is the grain size in millimeters)

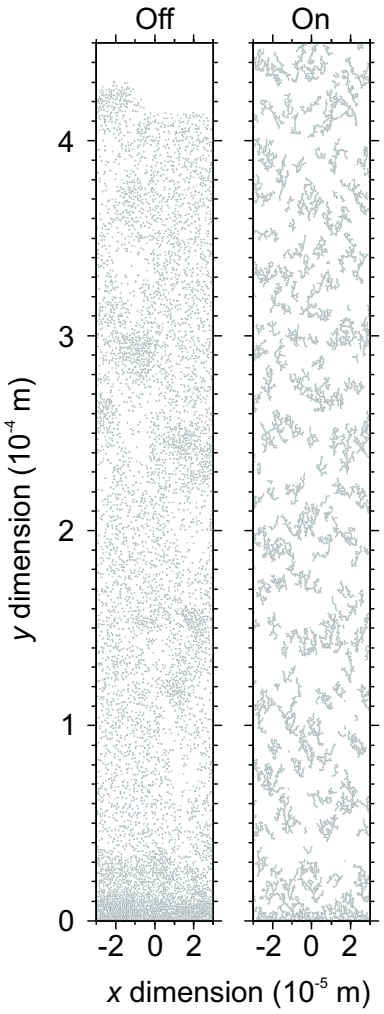

Figure 3.16: Sedimentation model of a collection of 10^4 particles of size $\phi = 10$ deposited under gravity without and with the influence of van der Waals forces. In the presence of van der Waals forces particles tend to floc, forming large aggregates

reveals the influence of van der Waals forces. After a short period of settling, van der Waals forces are responsible for forming flocs in the model container and the particles continue their descent as members of large aggregates. When the influence of van der Waals forces are not included in the model, the particles remain dispersed and aggregates do not form, Figure 3.16.

The final structure of the model sediment settled without the influence van der Waals forces is typical for particles falling though a viscous medium under the influence of gravity and is termed a *random loose packing*, (He *et al.* 1999). The influence of van der Waals forces appears to be substantial, with the formation of large voids in the modelled sediment as the attractive forces act to hold the particles in more chain-like structures, Figure 3.17. In addition, the void spaces in the model decrease in size with increasing depth in the sediment. This is due to the pressure of the overlying sediment which is sufficient to overcome the van der Waals forces between particles, resulting in a closer, gravity dominated packing

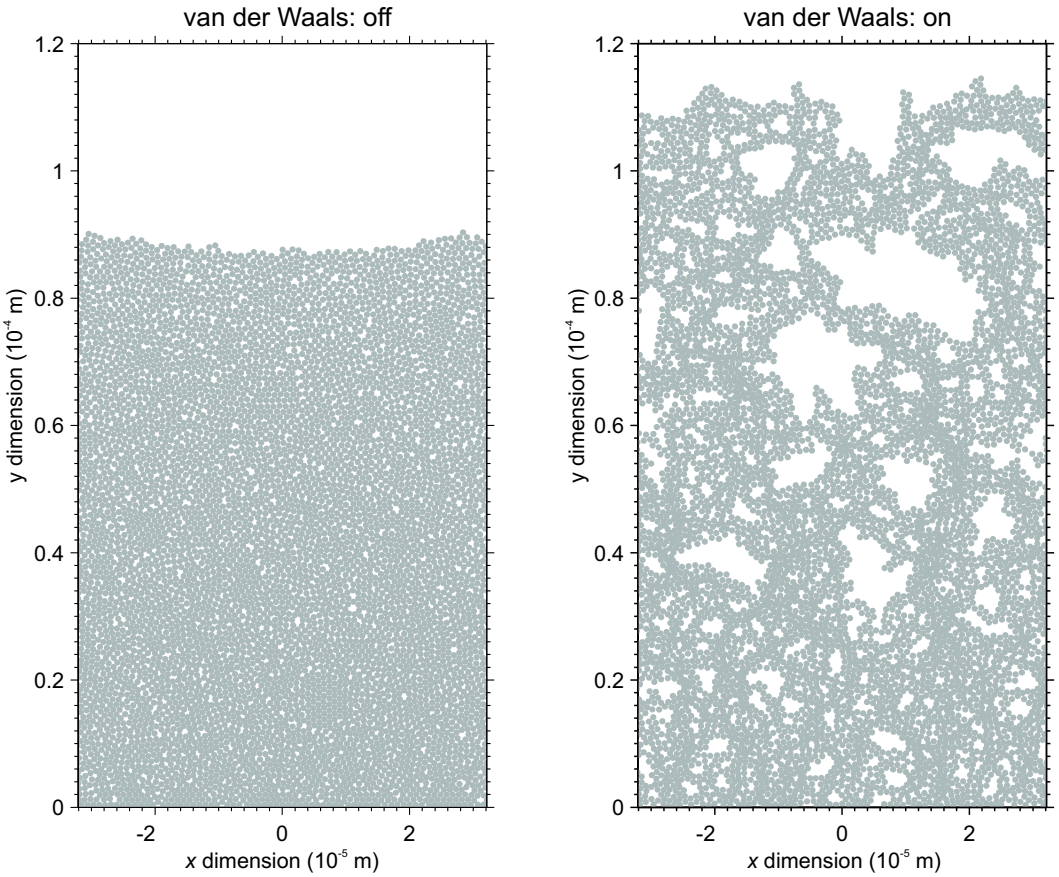

Figure 3.17: Final model configurations of a collection of 10^4 particles of size $\phi = 10$ deposited under gravity without and with the influence of van der Waals forces.

structure. It is expected that the effect of such an open porous structure would be to delay the formation of a stable NRM as there are many sites within the sediment matrix where rotation of magnetic particles would still be possible.

The distributions of coordination numbers in the two model sediments reveal a clear shift to a smaller mean number of particle-particle contacts (with a constant modal value), providing an indication of the more chain-like porous matrix structure, when van der Walls forces are applied, Figure 3.18a. As further examples we show the distribution of coordination number from models involving unequally sized particles. The shown examples, Figure 3.18b & c, have lognormally distributed particle sizes with a mean diameter of 7.5 ϕ (fine silt) and standard deviations of 0.3 and 0.6, corresponding to a *very well sorted* and a *moderately well sorted* sediment respectively (Boggs 2000). As with the previous examples both model assemblages show a tendency towards lower coordination numbers and thus a more open sediment structure when van der Waals forces are taken into consideration.

In the final example, Figure 3.18d, large monodisperse spheres are considered ($\phi = 2.0$, corresponding to medium to fine sand). In this case the particles are of a sufficient size that the forces due to gravity entirely overcome the van der Waals forces. As a result of this imbalance the distribution of coordination numbers is effectively independent of van der

Waals forces and both models produce a random loose packing. It is important to note at this point that the relationship between specific particle sizes and the effect of van der Waals forces is only semi-quantitative because a number of constants employed in the model are poorly defined and only spherical particles were considered.

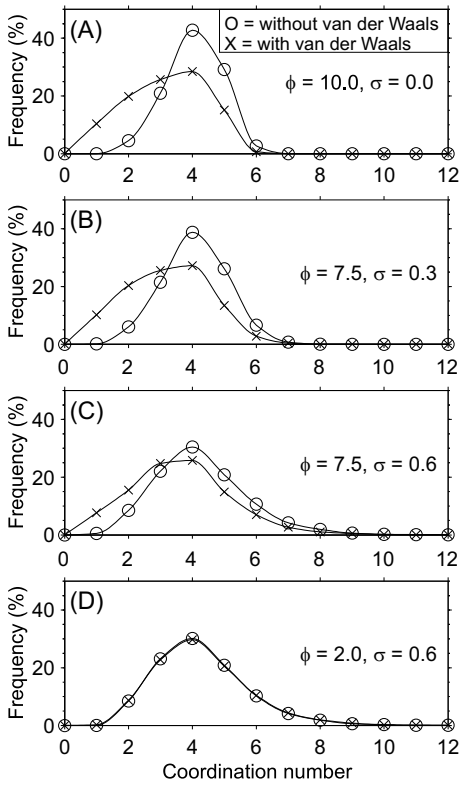

Figure 3.18: Coordination number distributions for the model sediment configurations obtained for different grain size distributions with and without the influence of van der Waals forces. ϕ represents the mean grain size and σ the standard deviation of the distribution.

Van der Waals forces: PDRM acquisition

The model results for spherical particles demonstrate the influence of van der Waals forces both in the water column and final sediment configuration, where the tendency of particles to produce chain-like structures yields a highly porous matrix structure. According to the model of Otofuji and Sasajima (1981b), PDRM formation is promoted by a porous sediment structure. At the sediment-water interface, the friction between particles is relatively low and can be overcome by the magnetic torque of a badly aligned particle. In an open sediment structure, this allows the alignment of the magnetic particles with the external field. As compaction proceeds, friction and packing increase and the chances of a particle being set free and aligning with the field decrease. It is apparent that van der Waals forces produce the kind of sediment structure that would make the PDRM acquisition mechanism of Otofuji and Sasajima (1981b) possible.

Discussion and conclusions

The ability of the DEM method to represent interacting systems of particles makes it a powerful tool for modelling particle behavior in sediments. It is possible to subject the model sediment to different forces and the particles' behavior can be determined. Using the DEM, it was possible to model the influence of particle shape, sediment depth and external magnetic field strength on the level of acquired remanence. The modelled remanence acquisition showed that the ability of particles to undergo realignment decreases with depth and particle elongation. Particle shape, magnetic field strength and overlying pressure all influence the ability of a magnetic grain to rotate within the modelled sedimentary matrix. The inclusion of van der Waals forces into a DEM model leads to formation of chain-like structures during settling and to a highly porous structure of the consolidated sediment. In the absence of van der Waals forces, the macrostructure of the sediment is more closed and resembles a random loose packing. In larger grained sediments the magnitude of the gravitational force on the particles almost entirely overcomes the influence of the van der Waals forces and the sediment forms a close packing almost immediately after settling.
A number of studies have hypothesized that PDRM intensity in natural sediments is a function of magnetic field strength, particle shape, overlying pressure and a number of other variables. For deep sea oceanic sediments, the results of the DEM model support this conjecture. Considering inter-particle forces, it is reasonable to assume that the fine-grained systems typical of deep-sea sedimentation will be influenced to some extent by van der Waals forces and there will be a tendency for particle flocs to form in the water column. It has been hypothesized that open sediment structures such as the ones produced by the DEM will promote PDRM acquisition (Otofuji and Sasajima 1981b). Van der Waals forces are one possible mechanism in the production of such a sediment configuration.
Investigating the processes of PDRM acquisition, many influencing factors have to be taken into consideration. Thus, the consideration of particle shape, sediment depth, van der Waals forces and external field strength is just the first step forward in the attempt of modelling PDRM acquisition in detail.

Investigation of a possible magnetic self-reversal mechanism in marine sediments

A. Witt, T. Kleiner, K. Fabian and D. Heslop

Universität Bremen, FB Geowissenschaften, Postfach 330440, 28334 Bremen, Germany, Tel. +49-421-218-3933, Fax +49-421-218-7008, Email witt@informatik.uni-bremen.de

Abstract

The processes which influence a detrital remanent magnetization (DRM) as well as the physical microscale factors that control the forming of a stable post-depositional remanent magnetization (PDRM) are still not fully understood. Previous investigations have reported the presence of apparent spurious 'ghost images' of magnetization reversals in marine sediment cores. Laboratory studies and statistical numerical approaches have shown the possibility of a sediment slurry to display an apparent self-reversal in magnetization. Such behavior in magnetic slurries could provide one explanation for spurious magnetizations in marine sediment cores. In laboratory experiments we investigated magnetization decay as a function of time in sediment suspensions produced with varying lithologies and particle concentrations. A companion model takes into account the physics of magnetic particle-particle interactions, Brownian motion and hydrodynamic forces to numerically investigate the possibilities of magnetic assemblages suspended in water to display dynamic reversals of magnetization. Neither the experiments nor the numerical models produced a self-reversal in magnetization thus implying that magnetic interactions or magnetic interactions in combination with Brownian motion are not responsible for the previously reported reversals.
Keywords: Depositional remanent magnetization, self-reversal, marine sediments

Submitted to GJI

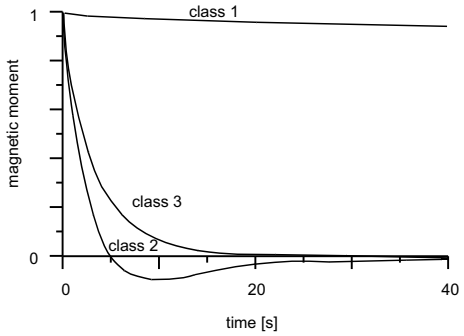

Figure 3.19: Experiments of Yoshida and Katsura (1985) using a sediment slurry consisting mainly of reddish-brown clay show three different classes of relaxation patterns. Class 1 and class 2 are attributed to electrostatic and magnetostatic interactions within the sediment slurry respectively. Class 3 is thought to represent a non-interacting system dominated by Brownian motion.

Introduction

The reconstruction of the earth's magnetic paleo-field from marine sediments is well-established. Still, the physical processes that control the formation of DRM and PDRM in marine sediments are not completely identified and remain under debate (Shcherbakov and Shcherbakova 1987; Tauxe 1993; Tauxe *et al.* 1996; Katari and Tauxe 2000; Katari and Bloxham 2001). For example, Bleil and von Dobeneck (1999) reported 'ghost images' of magnetization reversals that were attributed to lock-in effects or self-reversal of the sedimentary magnetization during remanence acquisition in a weak external field. There have been a variety of models and theoretical explanations concerning the DRM process. Collinson (1965) related the behavior of magnetic particles in a fluid to classical paramagnetic gas theory thus allowing the influence of Brownian motion on DRM formation to be investigated. Further calculations by Stacey (1972) showed that magnetic particles in a fluid treated as paramagnetic gas would take only a few seconds to reach an equilibrium with the external field conditions. Stacey's result implies that DRM formation should be 100% efficient and produce a saturation magnetization. Laboratory redeposition experiments carried out by Blow and Hamilton (1978), Kent (1973) and Levi and Banerjee (1990) showed that DRM intensity varied as a function of applied external field strength and therefore could not be 100% efficient, indicating that there are other processes involved in DRM and PDRM acquisition.

The experiments of Yoshida and Katsura (1985) showed that the relaxation behavior of a magnetic suspension is not fully describable by paramagnetic gas theory. Yoshida and Katsura (1985) used the relaxation behavior of dilute slurries to investigate the magnetic properties of different sediment types. Upon exposing the slurries to a weak external field they found three different relaxation patterns for the subsequent sample magnetization decay in zero field. The relaxation pattern of suspensions with a high particle concentration displayed nearly no decay, Fig. 3.19, class 1. Such a stable magnetization was attributed to flocculation of the sediment particles forming an ordered fabric and restricting the motion of the magnetic particles. Suspensions with intermediate concentrations displayed an exponential decay followed by a polarity change before approaching zero (class 2), this pattern was

attributed to magnetostatic interactions within the sediment slurry. The suspension with the lowest concentration displayed an exponential decay (class 3) and was attributed to a non-interacting system dominated by Brownian motion.
Investigating magnetic properties of natural sediments by using First-Order Reversal Curve diagrams, Roberts *et al.* (2000) detected magnetostatic interactions between single domain particles in a number of their samples. These investigations demonstrate that magnetic interactions occur in some natural sediments and could therefore play an important role in the process of DRM acquisition.
To investigate the influence of magnetostatic interactions we will present laboratory studies of remanence decay in sediment suspensions as well as a numerical model representing interacting magnetic particles in water. The model takes into account the physical theory of interacting magnetic particles, hydrodynamic forces and Brownian motion as a statistical disturbance. Whilst we investigate behavior in the watercolumn, fabrics at the sediment-water interface are highly porous (Kranck 1991; Wartel *et al.* 1991; Bennett *et al.* 1991) and therefore the processes that control the magnetic behavior of a slurry could also be valid for such sediments.

Experiments

Laboratory experiments

The experiments carried out to investigate the behavior of interacting magnetic particles in a sediment slurry were designed to match the experiments of Yoshida and Katsura (1985). The decay of slurry magnetizations were performed in zero field in order to be able to clearly define the influence of magnetostatic particle-particle interaction without bias due to an external field. In the experiments of Yoshida and Katsura (1985), the magnetic relaxation behavior of two different sediment types (reddish brown clay and calcareous ooze) in various concentrations was observed.
For the presented experiments, 20 samples were taken from 4 different gravity cores from the South Atlantic. The cores cover a broad range of lithologies (high content of opal, carbonate rich and clayey sediment) and their rock magnetic properties have been discussed previously by Franke *et al.* (2004). The chosen samples all had a magnetic susceptibility greater than $300 \cdot 10^{-6} SI$.
The sediment samples were suspended in distilled water mixed with a spatula tip of peptizer $Na_4P_2O_7 \cdot 10\, H_2O$. Sieving was then performed to remove the sediment fraction with diameters above 20 μm. The samples were homogenized by treatment in an ultrasonic bath and stirring. The sediment suspensions were concentrated by allowing the sediment to settle and removing the excess water. Nine different concentrations c_n were generated from each suspension ($c_n = 2^{-n} c_0$, $n = 0, .., 8$ and $c_0 = 1.5 \cdot 10^{-1}\ g/ml$). In the experiments, plastic containers filled with 7 ml of the suspensions were measured.
The samples were measured using a 2G cryogenic SQUID magnetometer. After being exposed to a 100 μT axial constant field in z-direction for 30 s, the samples' magnetic moment

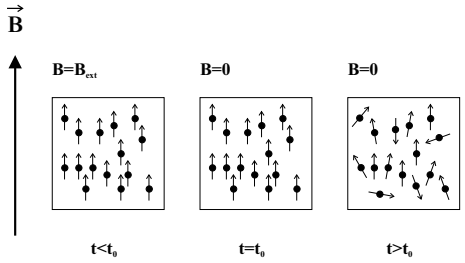

Figure 3.20: The sediment suspension is exposed to a magnetic field for 15 seconds, the particles align with the external field. At time $t = t_0$, the field is switched off and measurement of the magnetization commences. The decay of magnetization is recorded as a function of time for 120 s

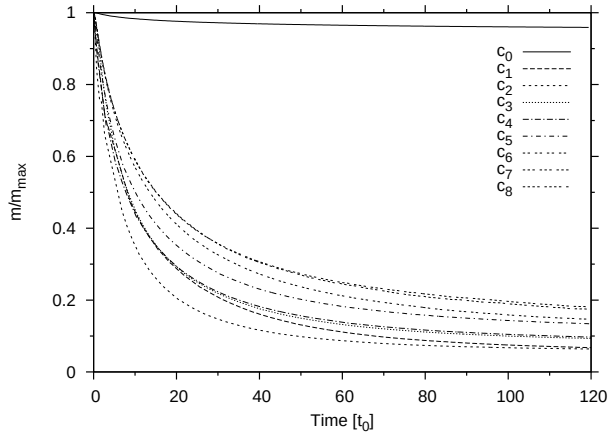

Figure 3.21: Experimental data for a typical sediment sample. The relaxation pattern of suspensions with nine different concentrations is plotted against time. The highest concentration (c_0) shows only a small decrease while the other suspensions relax far more quickly.

was measured along the z-axis in zero field over a period of 120 s. The basic concept of the laboratory studies is shown in Fig. 3.20.

Experimental results

In Fig. 3.21, an example of the decrease in magnetization is shown for all 9 concentrations of a typical sample. Suspensions with a high sediment concentration (c_0) displayed only a small decrease in magnetic moment with time. With decreasing sediment concentration, there is a large increase in the rate of relaxation.
According to Collinson (1965) and Stacey (1972), the decay of magnetization due to Brownian motion should be describable using an exponential function. Our measurements do not meet this requirement, they can best be described using the sum of two exponential functions and a constant.

$$m(t) = a_1 e^{-a_2 t} + a_3 e^{-a_4 t} + a_5 \tag{3.9}$$

where $\tau_1 = 1/a_2$ and $\tau_2 = 1/a_4$ are the relaxation times of the respective exponentials.

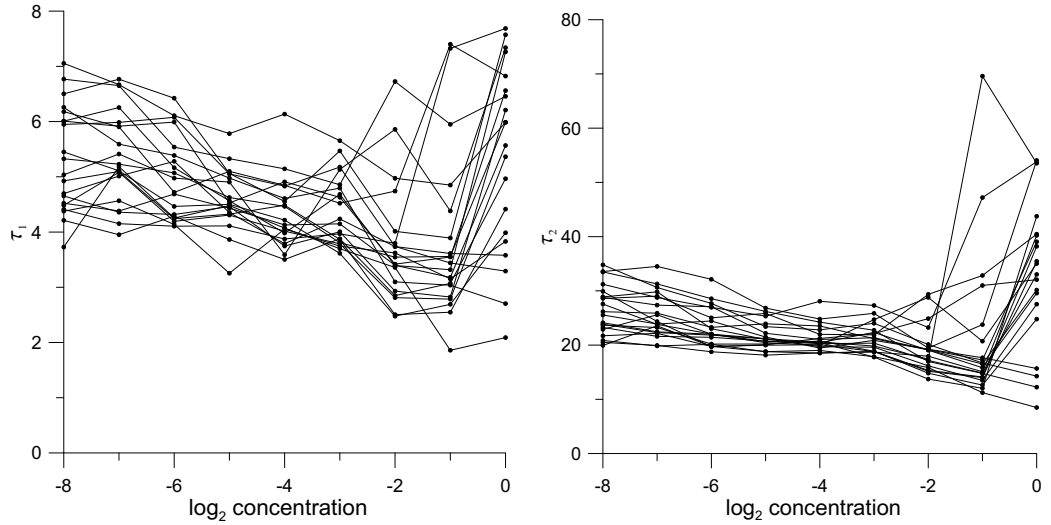

(a) (b)

Figure 3.22: (a) Relaxation time τ_1 plotted against a $\log_2$ based concentration. Out of 20 samples 16 displayed a significant decrease in relaxation time moving from low to high concentrations and an increase in relaxation time moving from second highest to highest concentration. (b) Relaxation time τ_2 plotted against a $\log_2$ based concentration. Out of 20 samples 15 displayed a significant decrease in relaxation time moving from low to high concentrations and an increase in relaxation time moving from second highest to highest concentration. From left to right, the data points represent concentrations c_8 through to c_0.

A plot of τ_1 against concentration and a plot of τ_2 against concentration for all samples displays a decrease in τ_1 and τ_2 with increasing concentration up to the second highest concentration (c_1), Fig. 3.22(a) and Fig. 3.22(b). From the second highest to the highest concentration there is a sharp increase in both τ_1 and τ_2. A Spearman rank correlation test showed that for 16 (τ_1) and 15 (τ_2) samples out of 20 there is a significant ($\alpha = 0.05$) monotonic decrease in τ_1 and τ_2 between c_8 and c_1. Plotting τ_1 against τ_2 reveals a linear relationship between the two parameters, Fig. 3.23(a). Additionally, a plot of a_5 against concentration shows a similar pattern to τ_1 and τ_2 with decreasing values as concentration increases until a sharp increase is observed at the highest concentrations, Fig. 3.23(b).
For suspensions with a constant viscosity, rotational Brownian motion leads to a concentration independent relaxation time:

$$\tau = \frac{3V\eta}{kT} \tag{3.10}$$

where V is the particle volume, η is the viscosity, k is the Boltzmann constant and T is the absolute temperature. However, the plots of τ_1 and τ_2 against concentration do not show a concentration independent behavior. The viscosity of the suspensions is expected to increase with increasing sediment concentration, therefore, according to eq.3.10, the time required for relaxation of the magnetization due to rotational Brownian motion should increase with viscosity. In addition, an increase in concentration also leads to increased flocculation processes, flocs are bigger than single particles and thus have a higher relaxation time than a single particle. For our experiments for concentrations less than c_0 the rate of magnetization decay increases with increasing concentration. Therefore, changes in the suspension's viscos-

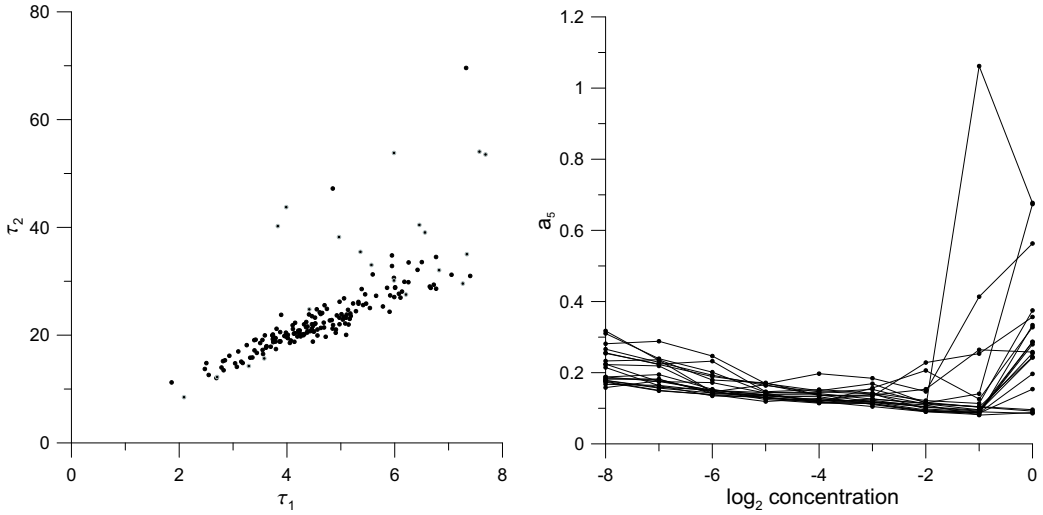

(a) (b)

Figure 3.23: (a) Relaxation time τ_1 plotted against relaxation time τ_2. The samples display a linear relationship between τ_1 and τ_2. The majority of samples that do not follow the trend correspond to the highest concentration suspensions that show very little decrease in magnetization (grey points). (b) Constant a_5 plotted against a $\log_2$ based concentration. There is a sharp increase in a_5 moving from second highest to highest concentration. This increase can be attributed to increased flocculation of magnetic and non-magnetic particles resulting in a locking of the magnetic particles. From left to right, the data points represent concentrations c_8 through to c_0.

ity and flocculation thus cannot be responsible for the decreasing relaxation times moving from c_8 to c_1 as displayed in Figs. 3.22(a) and 3.22(b).

The sharp increase in the plot of a_5 against concentration moving from second highest to highest concentration indicates that there is a process acting which prevents the overall magnetization of the system from relaxing. This process could be flocculation or clumping of particles, its influence appears to be strong enough to lead to high relaxation times.
Examination of eq. 3.10 shows that magnetization decay due to rotational Brownian motion will only follow an exponential if all the particles have the same radius. This would be an unrealistic assumption for natural sediments, therefore to understand more fully the effects of rotational Brownian motion it is important to consider the form of magnetization decay that will be observed in a system which contains particles with a distribution of sizes.
A simple Monte Carlo model was constructed to test if the experimental data could be fitted with curves corresponding to rotational Brownian motion acting upon a magnetic assemblage with a distribution of grain sizes. The model involved drawing 10^5 pseudo-random numbers from a log-normal distribution with predefined mean and standard deviation, these numbers were taken to represent the diameters of the magnetic particles in the system. The exponential decay for each of the particles was calculated and the curves were combined to provide a representation of the magnetization decay for the whole assemblage (under an assumption that all the particles have the same magnetization). The mean and standard deviation of the log-normally distributed random numbers were iteratively optimized in order to minimize the sum of squared residuals between the model curves and the experimental data.

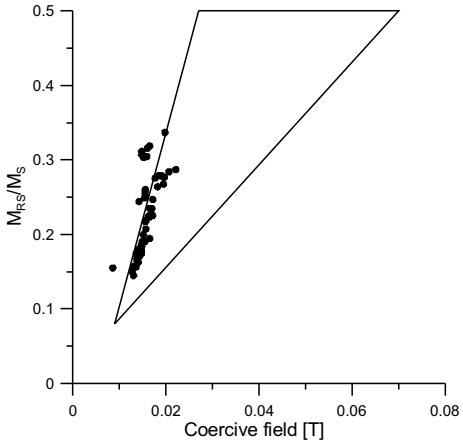

Figure 3.24: A ratio of saturation remanent magnetization and saturation magnetization (M_{RS}/M_S) plotted against the coercive field (data from Hofmann and Fabian (2005)). According to Tauxe *et al.* (2002), particles within the triangle can be considered to be mixtures of single domain magnetite particles and superparamagnetic material. The samples plot along the left edge of the superimposed triangle which, according to Tauxe *et al.* (2002) corresponds to a mixture containing uniaxial single domain magnetite with a length to width ratio of 1.3.

It was found that all of the experimental curves could be fitted closely with a decay corresponding to effects of rotational Brownian motion acting on distribution of particle sizes. The ability to fit the experimental data with a log-normal distribution of grain sizes indicates that τ_1 and τ_2 are predominantly controlled by rotational Brownian motion. The mean particle sizes and the standard deviations for the fitted distributions all fall into the clay size range (average distribution mean for all samples: $\phi = 8.57 \pm 0.17$ and average distribution dispersion for all samples: $\sigma_\phi = 0.18 \pm 0.02$). Such particle sizes are in contrast to the hysteresis data obtained for the sediment samples, Fig. 3.24, which indicates an assemblage dominated by a mixture of uniaxial single domain and superparamagnetic grains. The most obvious explanation for this discrepancy is that the magnetic particles are attached to larger clay particles, most probably by electrostatic forces (Lu *et al.* 1990), thus increasing their effective grain size in terms of the Brownian motion process. Although such a mechanism provides a convincing explanation for the experimental data it cannot account for the apparent gradual decrease of τ_1 and τ_2 with increasing concentration. Therefore, although rotational Brownian motion appears to be the dominant process controlling the decay of the magnetizations, other processes must also be acting.

Numerical model

Kinematics of magnetic particles in fluids

The experiments of Yoshida and Katsura (1985) raise the question whether an interacting assemblage of remanence carriers in a fluid can exhibit dynamic self-reversal, c.f. class 2 in Fig. 3.19. To investigate this problem, the equations of motion of n magnetic particles with radii R_i and magnetic moments m_i in a fluid have to be solved.

The dynamic self reversal as observed by Yoshida and Katsura (1985) cannot be attributed to Brownian motion only, therefore other processes must influence the suspension's relaxation behavior. Brownian motion and magnetic particle interaction are simulated in the presented numerical model. In addition to Brownian motion and magnetostatic particle interaction the particles will be subject to hydrodynamic forces. The particles are suspended in a carrier fluid of viscosity η and temperature T. The system's Reynolds number has a magnitude of approximately the particles' radius squared (Truckenbrodt 1980). Therefore, the system's inertia is negligibly small (Truckenbrodt 1980), all intertial terms are zero and the motion of the particles is described by the equilibria of forces and torques.

$$\mathbf{F}_i^{\mathrm{mag}} + \mathbf{F}_i^{\mathrm{visc}} + \mathbf{F}_i^{\mathrm{brown}} = \mathbf{0}, \tag{3.11}$$

$$\mathbf{L}_i^{\mathrm{mag}} + \mathbf{L}_i^{\mathrm{visc}} + \mathbf{L}_i^{\mathrm{brown}} = \mathbf{0}. \tag{3.12}$$

$\mathbf{F}_i^{mag}$ and $\mathbf{L}_i^{mag}$ are the force and torque exerted by the magnetic induction, $\mathbf{F}_i^{visc}$ and $\mathbf{L}_i^{visc}$ the force and torque imposed by the fluid's viscosity and $\mathbf{F}_i^{brown}$ and $\mathbf{L}_i^{brown}$ the force and torque attributed to Brownian motion. The latter will be accounted for by adding random disturbance to the particles' motion and will be discussed below.

Equations of Motion

The forces that contribute to the motion of the particles are the force exerted by the viscous fluid, $\mathbf{F}_i^{visc}$, and the force exerted by the magnetic field, $\mathbf{F}_i^{mag}$. The latter depends on the magnetostatic self-energy E_i^{mag} of the i-th dipole and the external magnetic field:

$$\mathbf{F}_i^{mag} = -\nabla E_i^{mag}(\mathbf{r}_i) \tag{3.13}$$

$$E_i^{mag}(\mathbf{r}_i) = -\mathbf{m}_i \cdot \mathbf{B}(\mathbf{r}_i) \tag{3.14}$$

The magnetic induction $\mathbf{B}(\mathbf{r}_i)$ is, in the absence of an external magnetic field, the sum of the dipolar interaction fields:

$$\mathbf{B}(\mathbf{r}) = \frac{\mu_0}{4\pi} \sum_{i=1}^{n} \left(3\frac{(\mathbf{m}_i \cdot (\mathbf{r} - \mathbf{r}_i))(\mathbf{r} - \mathbf{r}_i)}{|\mathbf{r} - \mathbf{r}_i|^5} - \frac{\mathbf{m}_i}{|\mathbf{r} - \mathbf{r}_i|^3} \right) \tag{3.15}$$

The viscous fluid exerts a force opposite to the dipole's velocity (Stoke's Law):

$$\mathbf{F}_i^{visc} = -6\pi\eta R_i \dot{\mathbf{r}}_i \tag{3.16}$$

This leads to the following equation of motion for particle translation:

$$\nabla(\mathbf{m_i} \cdot \mathbf{B}(\mathbf{r}_i)) = 6\pi\eta R_i \dot{\mathbf{r}}_i \tag{3.17}$$

$$\Rightarrow \qquad \dot{\mathbf{r}}_i = \frac{1}{6\pi\eta R_i} \nabla(\mathbf{m_i} \cdot \mathbf{B}(\mathbf{r}_i)) \tag{3.18}$$

The terms contributing to the equilibria of torques are the torque attributed to the magnetic field, $\mathbf{L}_i^{mag}$, and the torque attributed to the viscous fluid, $\mathbf{L}_i^{visc}$. The magnetic field exerts a torque $\mathbf{L}^{mag}$ acting on the dipoles (Gerthsen and Vogel 1993):

$$\mathbf{L_i}^{mag} = \mathbf{m}_i \times \mathbf{B}(\mathbf{r}_i) \tag{3.19}$$

The rotation of the dipoles due to the magnetic field acts against the viscous fluid. The fluid's viscosity gives rise to a torque $\mathbf{L}^{visc}$ which acts against $\mathbf{L}^{mag}$. Assuming the particles to be of spherical shape, $\mathbf{L}^{visc}$ takes on the following form (Currie 1974):

$$\mathbf{L_i}^{visc} = -8\pi R_i^3 \eta \dot{\boldsymbol{\varphi}} \tag{3.20}$$

thus leading to the following equation of motion:

$$\begin{aligned}
&\mathbf{m}_i \times \mathbf{B}(\mathbf{r_i}) = 8\pi R_i^3 \eta \dot{\boldsymbol{\varphi}}_i \\
\Rightarrow \quad &\boldsymbol{\omega}_i = \dot{\boldsymbol{\varphi}}_i = \frac{\mathbf{m}_i \times \mathbf{B}(\mathbf{r_i})}{8\pi R_i^3 \eta} \\
\Rightarrow \quad &\boldsymbol{\omega}_i \times \mathbf{e}_i = -\frac{1}{8\pi R_i^3 \eta} \mathbf{e}_i \times (\mathbf{m}_i \times \mathbf{B}(\mathbf{r_i})) \\
\Rightarrow \quad &\dot{\mathbf{e}}_i = \frac{-m_i}{8\pi R_i^3 \eta} \mathbf{e}_i \times (\mathbf{e}_i \times \mathbf{B}(\mathbf{r_i})) \\
\Rightarrow \quad &\dot{\mathbf{e}}_i = \frac{-m_i}{8\pi R_i^3 \eta} (\mathbf{e}_i \cdot (\mathbf{e}_i \cdot \mathbf{B}(\mathbf{r_i})) - \mathbf{B}(\mathbf{r_i}))
\end{aligned} \tag{3.21}$$

$m_i \mathbf{e}_i = \mathbf{m}_i$ and $|\mathbf{e}_i| = 1$, $\mathbf{e}_i$ is a unit vector in direction of $\mathbf{m}_i$.

Scaling

In order to save computation time, the model works with reduced magnitudes, this leads to a system of equations that are scale independent. Using the new system of equations, one can switch from physical variables to system variables. There are fewer system variables than physical variables which considerably reduces the computation time when systematically scanning through all sizes that influence the system. Another effect of the switching from physical to system variables is to avoid unnecessary inaccuracy in the numerical calculations. The equations of motion were scaled using values which are characteristic for this system. These values are indicated by a subscript zero. In the equations below, the physical parameters with a tilde denote the respective variable without units.

$$\begin{aligned}
\frac{d\mathbf{r}}{dt} &= \frac{d(R_0 \tilde{\mathbf{r}})}{d(t_0 \tilde{t})} \\
&= \frac{1}{6\pi\eta R_0 \tilde{R}} \frac{d}{d(R_0 \tilde{\mathbf{r}})} (m_0 \tilde{\mathbf{m}} B_0 \tilde{\mathbf{B}})
\end{aligned} \tag{3.22}$$

using $B_0 = \frac{\mu_0 m_0}{R_0^3}$, this leads to

$$\dot{\tilde{\mathbf{r}}} = \frac{\mu_0 t_0 m_0^2}{6\pi\eta R_0^6} \frac{1}{\tilde{R}} \tilde{\nabla} (\tilde{\mathbf{m}} \tilde{\mathbf{B}}) \tag{3.23}$$

and

$$\begin{aligned}\frac{d\mathbf{e}}{dt} &= \frac{d\mathbf{e}}{d(t_0\tilde{t})} \\ &= -\frac{m_0\tilde{\mathbf{m}}}{8\pi\eta R_0^3\tilde{R}^3}B_0(\mathbf{e}(\mathbf{e}\tilde{\mathbf{B}}) - \tilde{\mathbf{B}}) \\ \Rightarrow \quad \dot{\tilde{\mathbf{e}}} &= -\frac{\mu_0 t_0 m_0^2}{8\pi\eta R_0^6}\frac{\tilde{\mathbf{m}}}{\tilde{R}^3}(\mathbf{e}(\mathbf{e}\tilde{\mathbf{B}}) - \tilde{\mathbf{B}}) \end{aligned} \tag{3.24}$$

μ_0 being the permeability of free space in SI units.

Brownian motion

According to Debye (1929), the relaxation time of a system of particles can be calculated using the formula

$$\tau = \frac{\zeta}{2kT} \tag{3.25}$$

where ζ is a constant satisfying

$$\mathbf{L} = -\zeta\dot{\boldsymbol{\varphi}}. \tag{3.26}$$

In this case, $\mathbf{L}$ is the torque produced by the fluid's viscosity and $\zeta = 8\pi\eta R^3$ for spherical particles.
Translational Brownian motion is accounted for by adding a random number drawn from a normal distribution with standard deviation $\sigma_x = \sqrt{\frac{kT2\triangle t}{6\pi\eta R_i}}$ (Joos 1959) to an existing particle position. For the rotation, an Euler pole is chosen from a uniform distribution across a sphere's surface. A rotation matrix is constructed around this pole using an angle drawn from a normal distribution with standard deviation $\sigma_\theta = \sqrt{\frac{4kT\triangle t}{8\pi\eta R_i^3}}$ (Debye 1929). Again, these equations have to be transformed to a reduced form as discussed in the scaling section:

$$\tilde{\sigma}_x = \sqrt{\frac{2t_0 kT}{6\pi\eta R_0^3}\frac{\Delta\tilde{t}}{\tilde{R}_i}} \tag{3.27}$$

$$\tilde{\sigma}_\theta = \sqrt{\frac{4t_0 kT}{8\pi\eta R_0^3}\frac{\Delta\tilde{t}}{\tilde{R}_i^3}} \tag{3.28}$$

Numerical details of the model

Naturally occurring magnetic particles tend to form clusters as soon as they get close to each other. This is accounted for in the model by replacing two particles i and j that are less than twice the sum of their radii apart by a new particle:

$$|\mathbf{r}_i - \mathbf{r}_j| < 2(R_i + R_j)$$

The new particle's volume is the sum of the two former volumes, the magnetic moment is a vector sum of the two former moments.

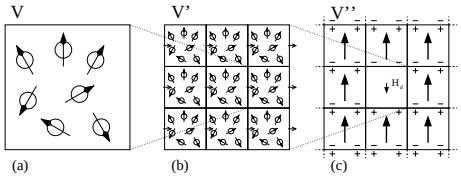

Figure 3.25: The n particles that are simulated are situated inside the center box V of a cube V' consisting of 27 boxes. The other 26 boxes contain shifted images of the center box. This should account for more realistic conditions while simulating the experiment, since the number of particles that can be handled at once is rather small. The large black arrows in (c) denote the average magnetization within each box. H_d is the demagnetizing field.

The numerical solver used to solve the differential equations is an Adaptive Runge-Kutta solver (Press *et al.* 1992). It adjusts the time steps it takes according to the function's gradient thus ensuring that the dipoles will not oscillate around each other when one gets into the other's vicinity.

For the calculations to be statistically representative, a large number of particles should be simulated. Since particle-particle interaction is taken into account, the computation time increases with the number of particles squared. Therefore, calculations dealing with many particles rapidly become cumbersome. In order to solve this problem, the computation space is assumed to be homogeneously magnetized. The space is split into $3 \times 3 \times 3$ equally sized cubes, each holding the same particle subset. For the particles within the center box, the equations of motion are solved taking into account the magnetic fields of the particles within this box and the 26 surrounding boxes. The field due to all other particles is taken into account by introducing their demagnetizing field, again assuming homogenous magnetization, cf. Fig. 3.25. This leads to the following equation for the magnetic field within V (see Fig. 3.25 for definitions of V and V'):

$$\mathbf{B}(\mathbf{r}) = \sum_{\mathbf{r}_i \in V'} \mathbf{B}(\mathbf{r}, \mathbf{r}_i, \mathbf{m}_i) + \mu_0 \mathbf{H}_d(\mathbf{r}) \tag{3.29}$$

The magnetostatic field in eq. 3.29 is obtained by calculating the surface charge potential Φ of the outer box, its negative gradient being the demagnetizing field (Fabian *et al.* 1996):

$$\begin{aligned}
\phi(\mathbf{r}) &= \frac{1}{4\pi} \left[\int_V \frac{-\nabla \mathbf{M}(\mathbf{r}')}{|\mathbf{r} - \mathbf{r}'|} \, dV' + \int_S \frac{\mathbf{M}(\mathbf{r}') \cdot \mathbf{n}(\mathbf{r}')}{|\mathbf{r} - \mathbf{r}'|} \, dS' \right] \\
&= \frac{1}{4\pi} \int_S \frac{\mathbf{M}(\mathbf{r}') \cdot \mathbf{n}(\mathbf{r}')}{|\mathbf{r} - \mathbf{r}'|} \, dS' \\
\mathbf{H}_d &= -\text{grad}\, \phi
\end{aligned}$$

V and S are the sample volume and surface respectively and $\mathbf{n}$ is the outward surface normal. Since the magnetization $\mathbf{M}$ is treated as constant inside the boxes, $-\nabla \mathbf{M}$ equals zero. The magnetostatic field is also expressed as a reduced magnitude.

$$\mathbf{H}(\mathbf{r}) = \frac{m_0}{R_0^3} \tilde{\mathbf{H}}(\tilde{\mathbf{r}})$$

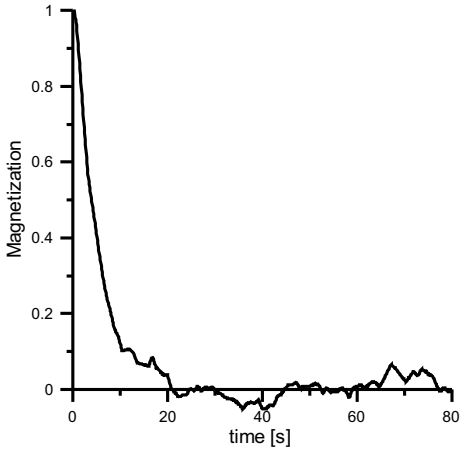

Figure 3.26: Example of a stack of 50 model runs with 20 particles each (arithmetic mean).

Table 3.2: systematic variation of parameters

particle radius	$0.1 - 10\ \mu m$
magnetic moment	$4.27 \cdot 10^{-16} - 9.57 \cdot 10^{-11}\ A/m^2$
concentration	$1/16 - 256\ ppm$
number of particles	20
number of stacked runs	50

8 particle radii and 8 magnetic moments equally distributed on a logarithmic scale as well as 12 different concentrations equally distributed on a log 2 scale were chosen.

In order to maintain energy and momentum within the computation space, we use periodical boundary conditions: a particle that leaves a box at one side reenters at the opposite side. The numerical model runs start with all particles aligned in one direction. Since there is no external field, the particles immediately start to rearrange. The relaxation pattern of a system of 20 particles was observed as a function of the particle concentration and radii. For each radius and concentration combination, 50 model runs were stacked to produce a more representative data set, Fig. 3.26.

Model runs

To investigate what causes the three different relaxation patterns as observed by Yoshida and Katsura (1985), magnetization was calculated as a function of scale length (R_0), scale length of magnetic moment (m_0) and particle concentration c, which is a substitute for $\tilde{\mathbf{R}}$. These three parameters are the only ones that need to be varied, they cover all possible configurations of system parameters, cf. section 3.

In Table 3.2, the parameter space covered in the calculations is shown. The chosen values correspond to naturally occurring magnetite samples. The reason for selecting a mineral with a large moment is to maximize the contribution from magnetostatic interactions. All model

runs were carried out with and without particle-particle interaction in order to be able to distinguish between the influence of Brownian motion and particle-particle interaction.

Numerical results

The current state of the model quantitatively reproduces class 3 relaxation patterns as observed by Yoshida and Katsura (1985). The simulated data can be fitted using one exponential function and a constant.

$$f(t) = a_1 e^{-a_2 t} + a_3$$

In order to interpret and visualize the numerical data, we chose a parallel coordinate representation (Inselberg 1985). Since our data is a function of particle radius, magnetic moment and concentration, all combinations yielding a single relaxation time, we are dealing with a four dimensional data set. To get an insight into the different interactions and interdependencies, four axes representing radius (r), magnetic moment (m), concentration (c) and relaxation time (τ) were plotted parallel to each other. The concentration as well as the radius were plotted on a log_2 scale, the magnetic moments on a log_{10} scale. A model result with radius-, magnetic moment-, concentration- and relaxation time-coordinate now results in a line moving from the left to the right axis, crossing the axes at which ever value belongs to this result, Fig 3.27. The complete data set is represented as grey lines while the region of interest is represented as black lines.
Looking at concentration dependencies, the lowest concentrations do not lead to the highest relaxation times, Fig 3.27(a) and Fig 3.27(b). Intermediate to high concentrations cover the whole range of relaxation times, Fig. 3.27(c). This indicates that particle-particle interactions influence the relaxation process but the decay curve can still be fitted with a single exponential.
Investigations of the data set as a function of radius shows that large particles cover the whole spectrum of relaxation times while particles with an intermediate to small radius lead to the shortest relaxation times, Fig. 3.28. This suggests that for particles with a radius below a certain size the influence of Brownian motion exceeds the influence of magnetic particle-particle interactions.

Looking at the magnetic moments, any given moment covers almost the entire range of relaxation times, large moments lead to slightly shorter relaxation times, whilst the relaxation times for small magnetic moments are more dispersed, Fig. 3.29.
Long relaxation times are due to the resistance of large particles to Brownian motion, Fig. 3.30(a). Large particles can relax quickly if the concentration of the suspension and their magnetic moment is high enough, Fig. 3.30(b) and Fig. 3.30(c). In this last configuration, particle-particle interactions seem to overcome the influence of Brownian motion.

There were also calculations carried out for non-interacting particle systems, these systems were subject to Brownian motion only. The relaxation times of the non-interacting systems displayed just a particle radius dependence. This is not surprising since Brownian motion depends neither on the particle concentration nor on the particles' magnetic moment and these experiments were simply used to confirm the numerical model. Comparing non-interacting

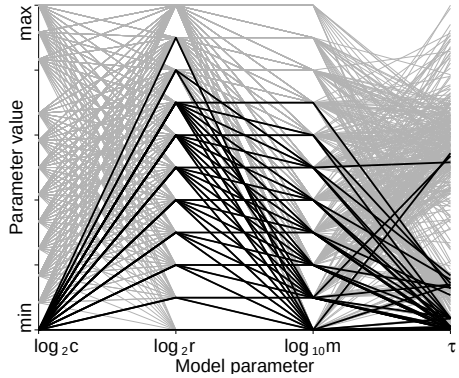

(a) smallest concentration

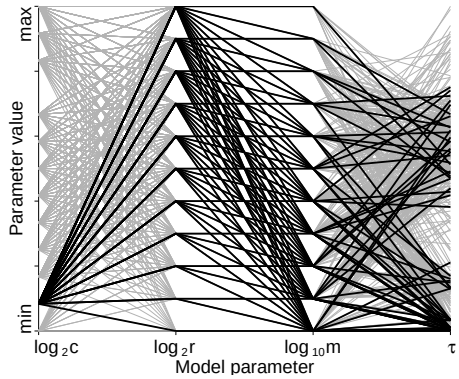

(b) second smallest concentration

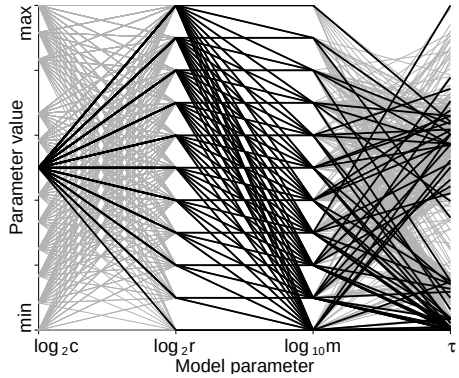

(c) intermediate concentration

Figure 3.27: Numerical data demarcated by concentration. c is the concentration, r the particle radius, m the magnetic moment and τ the relaxation time. The complete data set is shaded grey, the data we want to emphasize is displayed black.

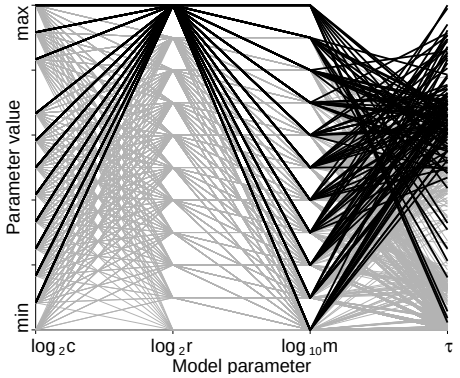

(a) biggest radius

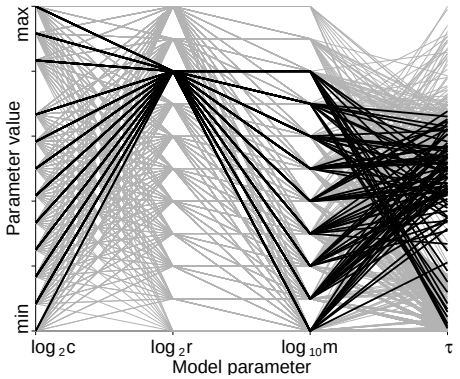

(b) intermediate radius

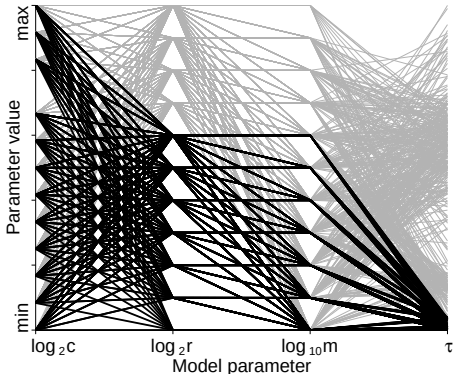

(c) small radii

Figure 3.28: Numerical data demarcated by particle radius. c is the concentration, r the particle radius, m the magnetic moment and τ the relaxation time. The complete data set is shaded grey, the data we want to emphasize is displayed black.

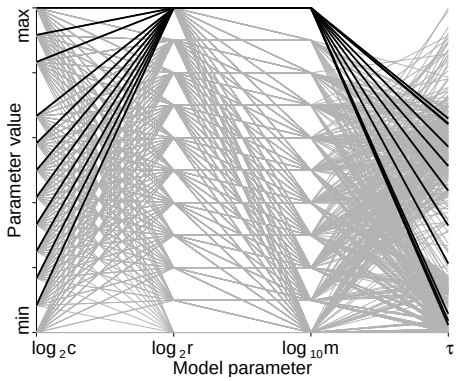

(a) high magnetic moment

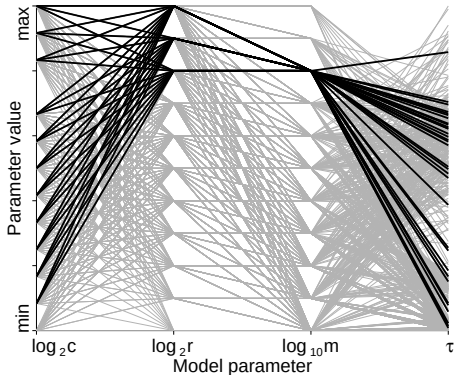

(b) intermediate moment

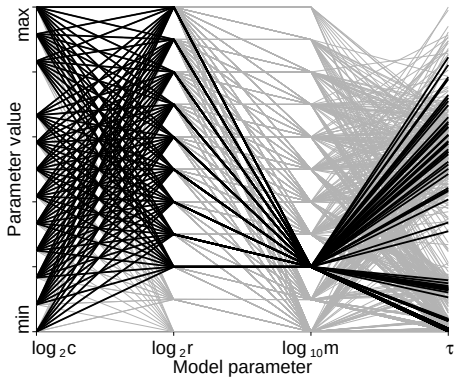

(c) small moment

Figure 3.29: Numerical data demarcated by magnetic moment. c is the concentration, r the particle radius, m the magnetic moment and τ the relaxation time. The complete data set is shaded grey, the data we want to emphasize is displayed black.

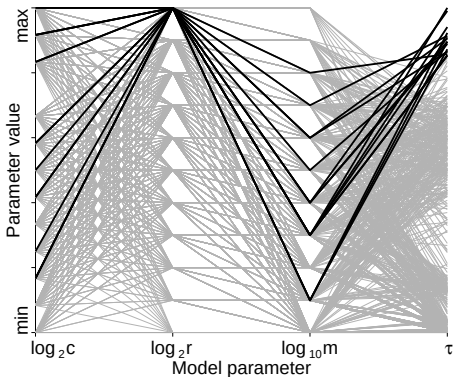

(a) long relaxation time

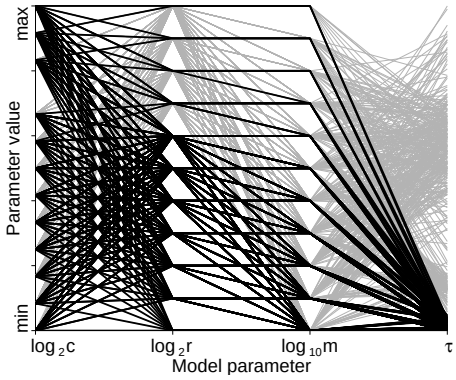

(b) short relaxation time

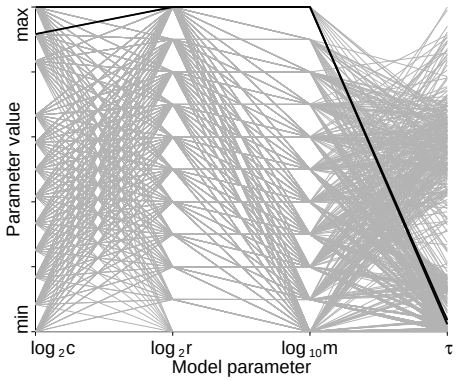

(c) short relaxation time/big radius

Figure 3.30: Numerical data demarcated by relaxation time. c is the concentration, r the particle radius, m the magnetic moment and τ the relaxation time. The complete data set is shaded grey, the data we want to emphasize is displayed black.

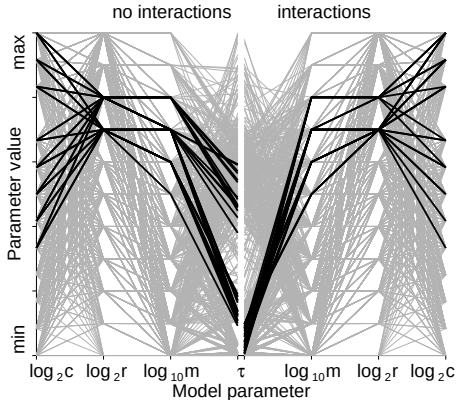

Figure 3.31: Comparison of relaxation time for non-interacting and interacting particle assemblages with high concentration, large radii and high magnetic moments.

systems to interacting systems, it appears that a certain concentration of magnetic material is necessary for the influence of particle-particle interaction to exceed the influence of Brownian motion. Once this concentration is reached, the relaxation time decreases rapidly with increasing concentration until a certain level is reached, Fig. 3.31. This level appears to remain constant for increasing concentrations. In Fig. 3.31, a system without magnetic interactions (left side) is compared to one with interactions (right side). It can be seen that for high concentrations and particle sizes with a high magnetic moment the interacting system leads to shorter relaxation times than the magnetically non-interacting system.

Discussion

The numerical experiments produced magnetization decay which can be fitted with a single exponential curve and demonstrate that we cannot clearly distinguish between the influence of Brownian motion and magnetic interactions when both processes act at the same time. Investigations through the parameter space of the model show the magnetization decay is predominantly controlled by Brownian motion, while magnetic interaction expresses itself by slightly modifying the relaxation time of the exponential curve. In this way they support the interpretation of the experimental data which suggested that the predominant process acting is Brownian motion, magnetostatic particle-particle interactions yield a fairly small contribution which still manages to alter the relaxation curve and explains why τ_1 and τ_2 are concentration dependant. The experimental results showed features such as a strong resistance to decay (characterized by a high value of a_5) that were not observed in the numerical results, thus indicating that processes other than Brownian motion and magnetostatic particle interaction play a major role in the magnetic relaxation behavior of a sediment slurry. Van der Waals forces or other electrostatic attractive forces are an example of forces that may have a large influence on the relaxation of magnetization. Electrostatic attractive forces would lead to the forming of clumps, magnetic particles could attach to bigger clay particles and thus form a large floc resistant to Brownian motion. When flocculation processes are dominant the formation of an ordered fabric could result in little or no magnetization decay.

The results of the Monte Carlo investigation indicate that flocculation is present in all of the suspensions with magnetic particles attaching to larger clay particles.
Considering the work of Yoshida and Katsura (1985), neither our experimental results nor the numerical model reproduce class 2 relaxation patterns as observed in their studies. Judging from our numerical experiments, processes other than Brownian motion and magnetostatic particle interactions must be responsible for the proposed magnetization reversals in sediment slurries.

Discrete element modelling of the influence of floc-formation on the acquisition of magnetization in sediment suspensions

A. Witt and D. Heslop

Universität Bremen, FB Geowissenschaften, Postfach 330440, 28334 Bremen, Germany, Tel. +49-421-218-3933, Fax +49-421-218-7008, Email witt@informatik.uni-bremen.de

Abstract

Detrital remanent magnetization (DRM) formation and the processes which lead to a stable sedimentary remanence are poorly understood. Organic coatings which act as a cement and electrostatic attraction such as van der Waals forces lead to flocculation of magnetic and non-magnetic particles within the water column. Previous experimental and theoretical investigations have indicated the level of acquired DRM may be a function of overall floc magnetization and size. Since the process of DRM formation is not directly observable, we make use of a series of two-dimensional numerical models based on the discrete element method (DEM) to investigate the influence of flocculation upon the level of suspended magnetic particle alignment with an external field.

Our DEM model takes into account irregular floc shape and the partial cancellation of the magnetizations of particles held in the same floc. We consider two forms of sediment suspensions, in the first, flocs are formed with no influence from an external field. In the second, floc formation takes place under the influence of a magnetic field. Flocculation is a dynamic process which is ongoing throughout the simulation, therefore no a priori assumptions are made concerning floc size. It is found that floc size has a major influence on the level of magnetic particle alignment. All of the models show that the extent of particle alignment is a function of both external field strength and the extent of flocculation. This has important implications for natural systems where the majority of magnetic particles are thought to descend through the water column attached to other particles.

Keywords: depositional remanent magnetization, discrete element method, marine sediments, van der Waals forces

Submitted to GJI

Introduction

Directional and intensity changes in the earth's magnetic field are continuously recorded in marine sediments. The use of these sedimentary records to reconstruct the earth's paleofield is a well established method in the earth sciences but the physical mechanisms that lead to the formation of a stable remanence are still under debate, for reviews see Verosub (1977) and Tauxe (1993). Detrital remanent magnetization is formed by the tendency of magnetic particles to physically rotate until their magnetizations are in equilibrium with the geomagnetic field. Initial rotation is thought to occur in the water column where an isolated magnetic particle would rapidly rotate into alignment with the external field. Once deposited at the sediment-water interface, so-called post-depositional mechanisms come into play with processes such as compaction and bioturbation influencing the orientation of the particles. In addition to such randomizing processes, the magnetic grains can still align with the geomagnetic field if they are captured within sediment voids where free rotation is still possible. Once compaction of the sediment is sufficient to physically hold all the magnetic particles in position, the remanence is considered to be stable and the magnetization 'locked in'. In the past, the influence on DRM formation of processes such as Brownian motion, sediment lithology and electrostatic forces have been investigated in both laboratory experiments (Barton *et al.* 1980; Lu *et al.* 1990; van Vreumingen 1993b; Katari and Tauxe 2000) and in numerical studies (Nagata 1961; Collinson 1965; Stacey 1972; Shcherbakov and Shcherbakova 1987; Katari and Bloxham 2001).

A theoretical calculation of the time required to align a magnetic sediment grain suspended in water with the geomagnetic field shows that this process would take a matter of seconds (Stacey 1972). Under such conditions, all the magnetic particles descending through a still water column would be expected to be aligned with the external field by the time they are deposited and thus form a saturated DRM. Natural remanences and even laboratory remanences are far from being completely saturated. In fact, sedimentary remanence intensity is known to vary as a function of applied field strength and this relationship forms the basis of relative paleointensity reconstructions (Johnson *et al.* 1975; Levi and Merrill 1976; Tauxe 1993). Such a field dependence is also observed in laboratory experiments, where the remanent magnetization of redeposited sedimentary material is found to increase with increasing external field strength (Johnson *et al.* 1948; Kent 1973; Yoshida and Katsura 1985; Quidelleur *et al.* 1995). A number of studies have concluded that randomization of the orientation of magnetic particles can occur whilst in the water column and post-depositionally (Irving and Major 1964; Verosub 1977; Lovlie 1989). It is therefore apparent that a field dependant magnetization is caused by the balance between the tendency of particles to align due to magnetic torque and their tendency to adopt no preferred orientation due to randomization processes.

Here, we will focus on the effect of flocculation on the level of magnetic particle alignment before deposition. The majority of suspended sediment entering the oceanic realm is flocculated and during descent through the water column, flocculation is a dynamic process with particles breaking apart and new aggregates forming. A combination of organic bonding and electrostatic attraction is thought to be responsible for the formation of microflocs ($10-20\ \mu m$) and macroflocs which are in size of the order of 1 mm (Dyer 1994). Therefore,

in typical ocean sediments, (silt-clay range) both micro- and macroflocs would be expected to contain a large number of individual magnetic particles.
Previously, van Vreumingen (1993b) investigated experimentally the variability of magnetization intensity with flocculation in suspensions of clay minerals and magnetic particles. Varying the salinity of the suspensions provided control over the level of floc formation by changing the magnitude of the electrostatic attractive forces which are responsible for holding particles together. After applying an ultrasonic treatment to ensure that the particles in the suspension were dispersed it was found that subsequent flocculation in an applied field reduced the magnetization of the system by up to 99%. Through salinity controlled floc growth it was determined that the greater the extent of flocculation, the lower the overall magnetization of the suspension. Therefore the mutual cancellation of magnetizations of particles included in a floc must be a primary controlling factor in DRM intensity. The effect of flocculation was considered experimentally by Katari and Tauxe (2000) and theoretically by Katari and Bloxham (2001) whose work resulted in a model for spherical flocs. In the model, the viscous drag of water and the magnetic torque of large flocs were of the same order of magnitude preventing perfect alignment of the aggregates in the water column with the applied magnetic field. Katari and Bloxham (2001) were able to closely fit data from redeposition experiments by Barton *et al.* (1980) with the viscous drag model even with the assumptions of spherical flocs and constant magnetic moments corresponding to a single magnetite particle in each aggregate.
Our two dimensional numerical model is based on the discrete element method (DEM). This model will be used to investigate the level of magnetization acquired in a suspension as a function of floc size and external magnetic field. The DEM can account for irregular floc geometry and cancellation of magnetic particle moments and therefore allows an extension of the work of Katari and Bloxham (2001) towards a system that is more representative of natural sediment processes.

The Discrete Element Model

The DEM

The discrete element method provides a numerical description of the behavior of an assemblage of discrete interacting particles. The key to the DEM is the ability to model the behavior of particles which come into contact. We employ a so-called soft-body approach where contacts are represented by allowing small particle overlaps Fig. 3.32. When particles come into contact, a force $\mathbf{F}_n$ acts normal to the contact and a shear force, $\mathbf{F}_s$, acts parallel to the contact. The contact is split into two phases: a loading phase and an unloading phase where the magnitude of $\mathbf{F}_n$ is related to the extent of particle overlap d_n. Because the forces of the unloading phase of a contact are less than those of the loading phase, energy is dissipated during a collision producing a visco-elastic effect (Cundall 1987). The magnitude of the shear force is related to the magnitude of the normal force and is limited by Coulomb's law of friction:

$$\|\mathbf{F}_n\| \leq \mu \|\mathbf{F}_s\| \tag{3.31}$$

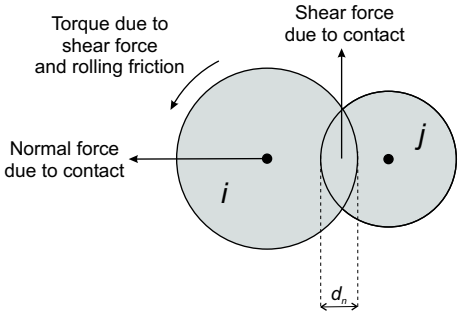

Figure 3.32: Schematic illustration of the forces acting on particle i due to the contact with particle j. A soft-body approach is applied which allows the particles to overlap at contacts. In case of an overlap, the value d_n becomes positive (the magnitude of the overlap in the figure is exaggerated for illustrative purposes). The software used in the presented DEM simulations is the pfc2d package from Itasca (Cundall and Strack 1979)

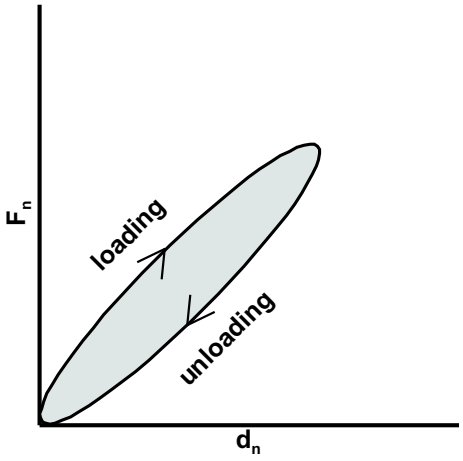

Figure 3.33: Schematic illustration of the viscoelastic contact treatment according to Cundall (1979). The shaded area between the loading and unloading curve is energy dissipation due to contact.

where μ is the coefficient of friction.
In a single cycle of the DEM model, Newton's second law of motion and the force-displacement law are used subsequently to take into account both particle-particle interactions and translation due to gravity. An additional linear term is added to the equations of motion for non-contacting particles, which acts as a form of local damping to reduce accelerations, both rotational and translational. This damping approach provides an approximation for the friction experienced by a particle travelling through a viscous medium, in this case water. In the course of a model run, position, velocity, acceleration and acting forces can be observed at each iteration for the individual particles within the system.

Modelling of flocculation in a settling sediment

The presented model consists of an assemblage of approximately 5000 particles with a log-normal size distribution typical for oceanic sediments ($\bar{\phi} = 8$ with a dispersion of $\sigma_\phi = 0.3$, on the Udden & Wentworth scale, $\phi = -\log_2 d$, where d is the grain size in millimeters). The initial particle positions are drawn from uniform random distributions of coordinates within a predefined area. In order to produce a high energy starting state analogous to turbulent water in ocean systems or ultrasonic treatment in laboratory experiments, e.g. van Vreumingen (1993b), we employed a 'radius expansion' particle generation approach (Itasca 2002). The individual particles are created with initially reduced radii and large overlaps with their neighbors. The particles' radii are then expanded to their final size resulting in unrealistically large overlaps, thus generating high kinetic energy in the system. No boundaries are applied to the space of the model, therefore the system is allowed to expand through time. This approach removes the effect of bounding walls which tend to produce particle bridges between them.
In nature, the majority of suspended particles are held in flocs bonded together by some form of organic material acting as a cement (Eisma 1986). To initiate the cementing of particles, we employ van der Waals forces which are short range attractive electrostatic forces. We use a numerical representation of van der Waals forces for particles that are large compared to the distance separating them (Hamaker 1937). With

$$\phi = -\frac{A}{6}\left[\frac{d_1 d_2/2}{D^2 - (\frac{d_1+d_2}{2})^2} + \frac{d_1 + d_2}{D^2 - (\frac{d_1-d_2}{2})^2} + \ln\frac{D^2 - (\frac{d_1+d_2}{2})^2}{D^2 - (\frac{d_1-d_2}{2})^2}\right] \tag{3.32}$$

and

$$\mathbf{F} = -\nabla\phi \tag{3.33}$$

where

$$D = \frac{d_1 + d_2}{2} + s \tag{3.34}$$

one is able to obtain an approximation for van der Waals forces, where A is the material dependent Hamaker constant (set to $10^{-19}J$ for all models), d is the diameters of the particles

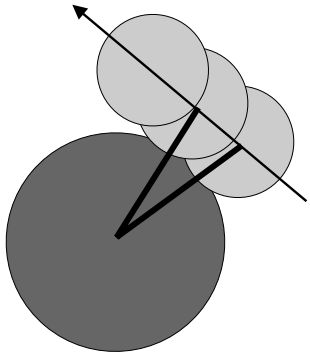

Figure 3.34: The magnetic particles are a combination of three equally sized spheres (light grey) and have an aspect ratio (width/length) of 0.5 with the magnetization pointing along the particle's long axis. Van der Waals forces are taken into account by assigning contact bonds between the particles (heavy black lines). If two particles have two contact points, two contact bonds are assigned between them.

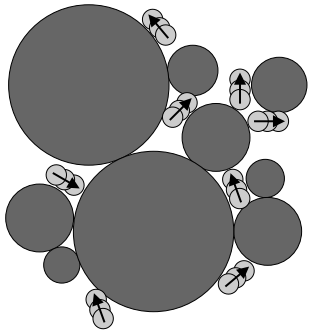

Figure 3.35: Model of a particle floc due to van der Waals forces. The overall resultant magnetization in such a clump is much smaller than the resultant magnetization of all the magnetic particles in perfect alignment with the field.

and s their surface-surface separation.
In an n-particle model, the exact computation of the acting van der Waals forces would amount to approximately n^2 computations. Computations of the order n^2 are not desirable since computation time is soon unmanageable. Since van der Waals forces decrease with the particles' separation to the power of 7, we only consider van der Waals forces for particles that are in contact or about to contact. Because of the zero in the denominator in eq. 3.32 for contacting particles we assume a minimum separation of 4Å for all contacts (Hamaker 1937) this also accounts for negative values of s when particles overlap in the soft body contact model. The organic cementation of particles is accounted for by assigning a contact bond between them with the same strength as the acting van der Waals force. The assigned contact bonds are not permanent and can be broken if sufficient forces act to overcome the attachment of two particles.

Magnetic properties of the model

The pfc2d software we use for our two dimensional simulations restricts the model to spherical particles. For our calculations, three spherical particles were statically combined to form

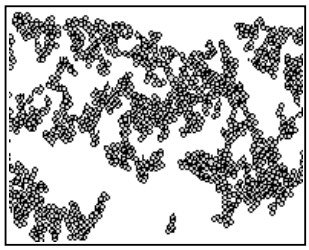

Figure 3.36: Enlarged section of one model run with particles forming flocs as they descend through the water column.

non-spherical magnetic particles with an aspect ratio of 0.5 and diameter of 1 μm ($\phi = 10$), Fig. 3.34. Of the particles in the sediment 10% are magnetic and are assigned a magnetization of $900 A/m$ according to the magnetite grain size dependent relationship for thermoremanent magnetizations acquired in a 100 μT field (Dunlop 1990a). For non-spherical magnetic grains, there are cases of more than one contact point between two particles Fig. 3.34. A contact bond is assigned to all of these contact points as would be expected for a natural cementation process.

The first set of model runs starts with all magnetic particles aligned with an external field of predefined strength and no initial flocculation. This state represents particles that have descended through turbulent water where flocculation was not possible. Upon entering a zone of still water, particles align rapidly with the external field and flocculation commences. The second set of models starts with randomly oriented particles and the external field is not applied until a predefined point in time. This allows flocculation to commence with no influence from the external field, thus simulating the entry of particles into a still water zone as members of preformed flocs. After the initial step of both models, the particles descend downwards and flocculation continues in the presence of an external magnetic field, Fig. 3.36. Five different magnetic fields typical of possible geomagnetic intensities are investigated in these model runs: 0, 5, 20, 50 and 100 μT in the vertical direction.

Limitations of the model

Up to this point, it is not practical to include particle-fluid coupling in our model. DEM contact models are based on dry powders and the effects of interstitial fluids on particle-particle interactions are poorly understood (Muguruma *et al.* 2000). As discussed above, inclusion of a linear damping coefficient (Cundall and Strack 1979) provides an approximation for particle motion through a viscous fluid. This effect, however, does not produce settling according to Stokes' law and therefore collisions and resultant flocculation will not occur due to different settling velocities. An elongated magnetic floc with a low resultant magnetization would naturally descend through the water column with its long axis perpendicular to the axis of descent (Pan *et al.* 2002) as the hydrodynamic torque dominates over the magnetic torque. In our numerical model, as in that of Katari and Bloxham (2001), the slightest magnetic moment is enough to rotate the floc into alignment with the field providing the residence time in the still water zone is sufficient. There are certain advantages to not considering full particle-fluid coupling in 2D. The viscous drag of a fluid acting on a natural floc is strongly

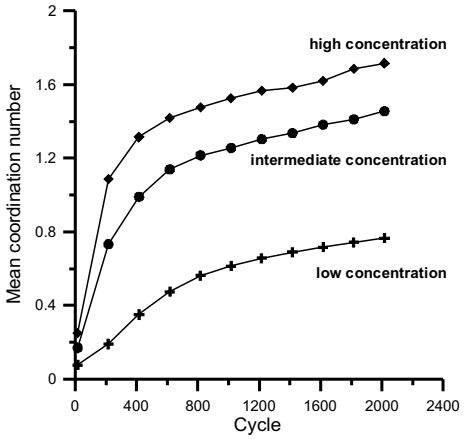

Figure 3.37: Plot of the change in coordination numbers throughout the model runs for all three starting concentrations.

influenced by the porosity of the aggregate (Wu and Lee 2001). In a 2D system, flocs are non-porous and if full particle-fluid coupling was included in the model, the hydrodynamic torque acting on a non-porous 2D floc would be over represented compared to the torque on the equivalent porous 3D floc.

Results

Flocculation

The size of the area in which particles are initially generated can be changed in order to produce suspensions with different particle concentrations. We employ starting areas with three different sizes, area based concentrations of 0.03, 0.02 and 0.01. The extent of flocculation is monitored using the concept of coordination numbers which represent the average number of contacting neighbors of each particle within the system, therefore high coordination numbers indicate greater flocculation. The coordination numbers of all three systems show that flocculation is ongoing throughout the duration of the model, Fig. 3.37. Initially, flocs form rapidly and subsequently the rate of floc formation decreases as the system expands and particle-particle collisions become less frequent. Not surprisingly the mean coordination number is directly related to initial concentration with the largest flocs forming in the smallest regime where collisions are the most frequent. Of the three systems, the low concentration suspension produces substantially smaller flocs than the two more concentrated suspensions. The mean coordination numbers reveal that the final floc sizes of the low concentration suspension are similar to those found in the early stages of the higher concentration suspensions. Thus it is possible to control the extent of flocculation in the numerical suspension simply by varying the concentration of particles in the initial configuration with higher concentrations producing larger flocs.

Flocculation commencing in the still water zone

In the system where all sediment particles enter the still water zone as individuals and the magnetic grains are fully aligned with the external field before flocculation commences all the intensity curves display an initial rapid decay followed by a more gradual reduction in magnetization, Fig. 3.38. At the beginning of each model, the system has a high kinetic energy and therefore particle-particle collisions do not always result in the formation of a bond but instead act to randomize the orientation of the particles. The initial behavior of each of the models follows the same path as the zero field curve, demonstrating the dominance of kinetic energy and the low influence of external magnetic field. Once sufficient energy has been dissipated from the system by viscoelastic behavior and damped motion, collisions start to produce bonds and flocs form. This is expressed by a departure of the curves from the zero field path. The point of departure is dependant on the field strength and concentration of the system indicating the increasing influence of the external field when flocculation is limited. In all the curves where an external magnetic field is invoked, a small recovery in magnetization is observed after the rapid initial decay. This peak corresponds to the commencement of floc formation and rotation into alignment with the external field. Once large flocs start to form, their inertia has an increasing influence on future collisions. A comparison of final magnetization as a function of applied field for the three different sized systems shows a similar pattern to the coordination numbers, Fig. 3.39 and Fig. 3.37, with the smallest flocs producing the highest magnetization. It is important to note that even in the absence of an external magnetic field the magnetization of the system does not reach zero. This is because the system is expanding and thus has a continuously decreasing concentration. After a certain level of expansion, further particle-particle collisions become highly improbable and the equilibrium magnetization is due solely to the flocs which retain some memory of the initially aligned particle state.

Flocculation above the still water zone

To simulate particle flocculation in turbulent water, the magnetic particles were initially assigned a random orientation in zero field. Flocculation was then allowed to proceed in zero field until all the magnetic particles had at least one contact bond, the external field was then invoked. The sudden introduction of an external field represents the movement of flocculated particles from turbulent water where magnetic torque will have little or no control over particle orientation into still water where magnetic torque can play an important role. In all the suspensions, there is a clear dependence between field strength and acquired magnetization, thus indicating the role of flocculation, Fig. 3.40. In a system with no flocculation, the magnetization would rapidly reach saturation in an external field as the magnetic particles are free to rotate. The high field curves rapidly acquire an equilibrium magnetization and maintain a stable intensity for the remainder of the model run. Such non-saturation is indicative of the partial cancellation of magnetic moments within the floc. As discussed above, the variation of final magnetization as a function of field appears to be related to the ongoing process of flocculation. In the high field cases, once the field is invoked, all of the flocs rapidly rotate into alignment with the external magnetic field. Once

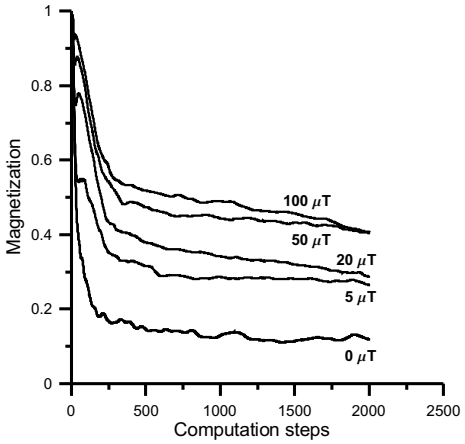

(a) high particle starting concentration

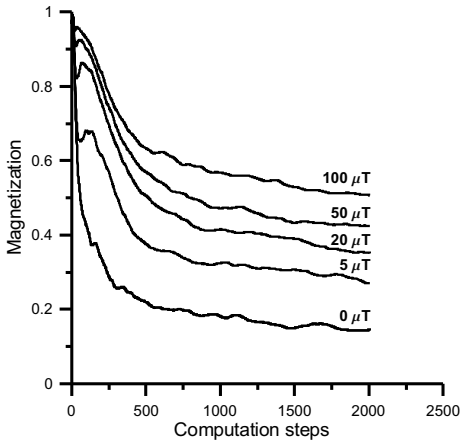

(b) intermediate particle starting concentration

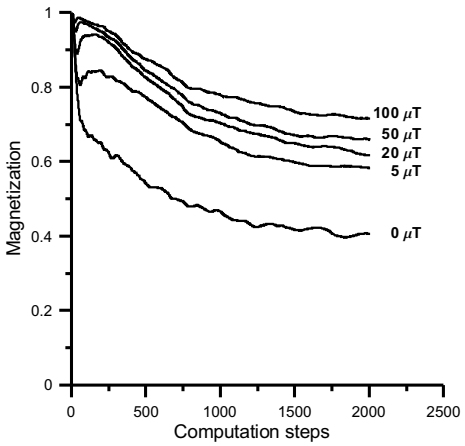

(c) low particle starting concentration

Figure 3.38: Decay in magnetization when entering the still water zone as individual particles. Three different starting concentrations with 5 different geomagnetic field strength values each are displayed. The scaling of the y-axis changes in order to provide more information.

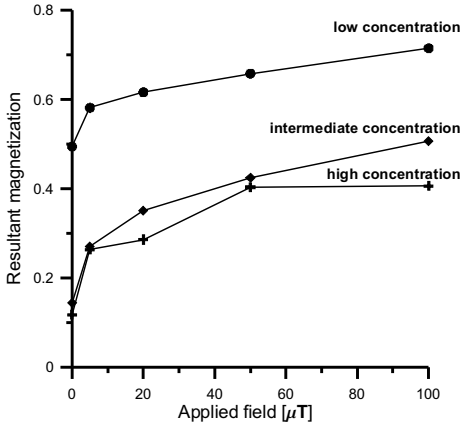

Figure 3.39: Acquired magnetization as a function of external field strength displayed for all three starting concentrations and the particles entering the still water zone as individual particles.

in this configuration, further flocculation has limited influence on the amount of acquired magnetization. For weaker fields, the degree of alignment is reduced and the time required for rotation into alignment is increased. Therefore, further aggregation involves flocs including particles with a distribution of alignments, the dispersion of which increases with decreasing field strength. In this way, cancellation is greater in the flocs formed in weaker fields. More details of the effects of flocculation are revealed by the high and intermediate concentration systems, Fig. 3.40(b) and Fig. 3.40(c). As floc size and therefore rotational drag increases, the equilibrium magnetization decreases, as the flocs require more time to align with the external field. Therefore, magnetization is a function of both external field strength and floc size, Fig. 3.41. The coordination numbers indicate that the high and intermediate concentration systems contain similar sized flocs whilst the low concentration system contains much smaller flocs, Fig. 3.37. The pattern of resultant magnetization as a function of applied field is closely related to the pattern observed in the coordination number plot with the low concentration system showing substantially higher magnetizations.

Discussion and conclusions

Because expected rates of floc formation and destruction are not known, it is difficult to select appropriate contact bond models which will provide an accurate representation of natural aggregation processes. Since our model does not take into account fluid dynamics, it strongly favors energy dissipation and as such particle flocculation occurs more readily than floc destruction. Even with this bias, the flocs produced in the model are smaller than the macroflocs found in natural systems.

From previous theoretical work it was suggested that Brownian motion could play a dominant role on the misalignment of magnetic particles in the water column resulting in reduced sedimentary remanences (Collinson 1965; Stacey 1972). In our model, flocculation, not Brownian motion, is responsible for reducing the level of particle alignment in the water column. As the majority of the magnetic particles are expected to be included in large

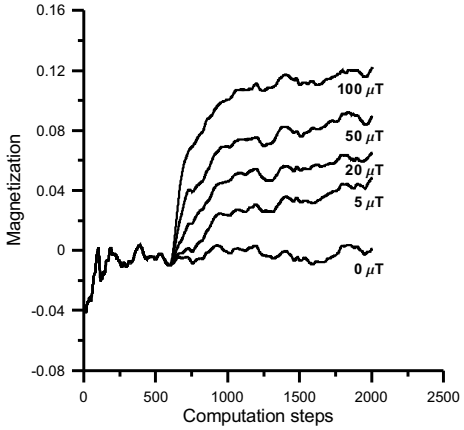

(a) high particle starting concentration

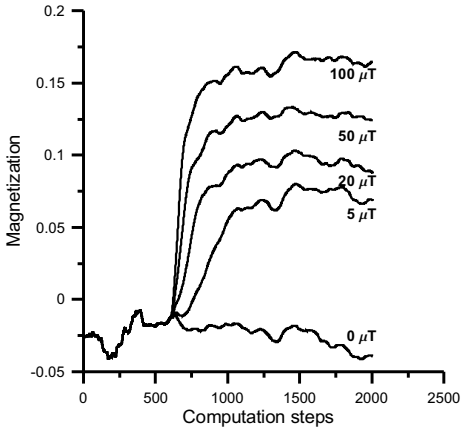

(b) intermediate particle starting concentration

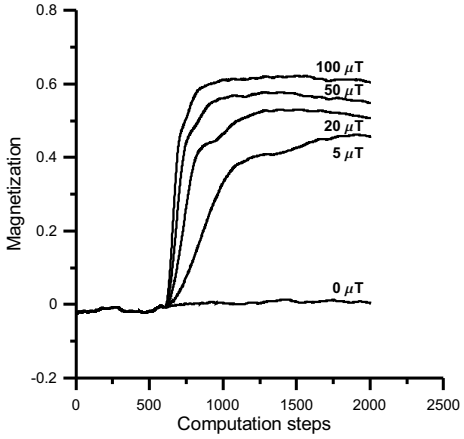

(c) low starting particle concentration

Figure 3.40: Acquired magnetization in the still water zone when flocculation already occurs above the still water zone. Three different starting concentrations with 5 different geomagnetic field strength values each are displayed. The scaling of the y-axis changes in order to provide more information.

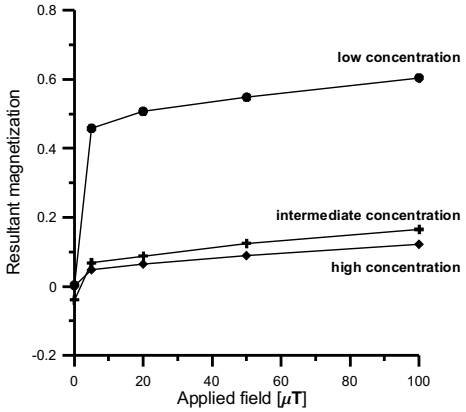

Figure 3.41: Acquired magnetization as a function of external field strength displayed for all three starting concentrations and the flocculation commencing above the still water zone.

aggregates, it is reasonable to assume that their orientation will not be influenced by Brownian motion. Considering a field typical of the earth's magnetic field (50 μT), the final suspension magnetization varies between 9% and 55% for flocculation above the still water zone and 40% and 66% for flocculation commencing in the still water zone. Values for natural sedimentary remanences are expected to be less than approximately 1% (Barton *et al.* 1980). It is not surprising that the calculated magnetizations are greater than those found in natural sediments as a number of additional randomizing factors are not included in the model. As previously discussed, the lack of fluid particle coupling plays an important role. Differential settling cannot be represented and flocs of different sizes will not collide due to differing descent velocities. Therefore flocs in the model will tend to be smaller than expected and thus less cancellation takes place. Additionally, shear flow that would cause more particle-particle collisions and would have a randomizing effect on particle orientations is not considered. Furthermore, natural sedimentary remanences will be strongly controlled by post-depositional processes as bioturbation, compaction and chemical alteration all of which are expected to alter the magnetization (Kent 1973; Karlin and Levi 1985; Channell 1989). Therefore, magnetizations in the water column cannot be compared directly to sedimentary remanences.

All of the presented models show a relationship of increasing magnetization with increasing field strength and decreasing floc size. This supports the previous experimental work of van Vreumingen (1993b) and the theoretical models of Katari and Bloxham (2001). In the viscous drag model of Katari and Bloxham (2001), a saturation magnetization will always be achieved if the still water zone through which flocs descend is sufficiently large because cancellation of magnetic moments is not included in the model. The DEM approach allows us to represent mutual cancellations of the magnetizations of particles contained in the same floc. This process is clearly demonstrated because magnetization varies inversely with floc size. Therefore, in a flocculating system, saturation magnetization will never be achieved no matter how large the still water zone is. This has important implications for natural sediment DRMs and provides one possible mechanism that could be responsible for magnetizations being dependent on the geomagnetic field strength.

4 Inclination error

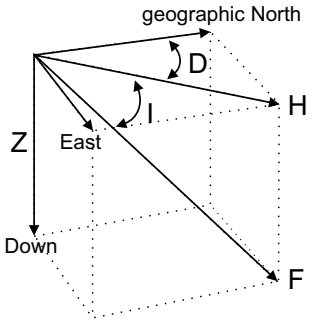

Figure 4.1: Declination D and inclination I of the total field **F**. H and Z are the horizontal and vertical components of **F**, respectively.

The direction of the paleomagnetic field is obtained from magnetic records in terms of inclination I and declination D, Fig. 4.1. Inclination is the angle between the horizontal plane and the field vector, declination is the angle between the vector's projection into the horizontal plane and true north. Geodynamic reconstructions as well as investigations of the structure of the paleomagnetic field are based on the assumption that the time-averaged field corresponds to a geocentric axial dipole, Fig. 4.2. Under this assumption, the geographic latitude θ and geomagnetic inclination I are linked by

$$\tan I = 2 \tan \theta \tag{4.1}$$

When paleofield inclination is identified with sample remanence inclination I_r, a bias of the latter automatically leads to an incorrect determination of the sample's paleolatitude.
By using 185 deep-sea sediment cores, Schneider and Kent (1990) showed that inclinations from sediment records match the expected dipole inclinations. Nevertheless, there are many processes influencing the recorded remanence. During deposition and recording, mechanical moments can exceed the magnetic torque. Since effects of mechanical moments are random in their direction to true north, this does not affect the recorded declination but could result in an inclination error. King (1955) proposed a first model for mechanical misalignment. He

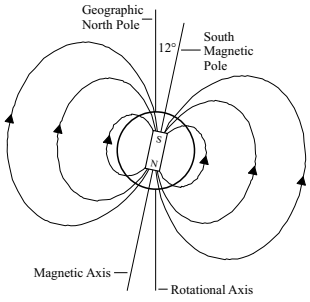

Figure 4.2: Modern day dipole field. In a geocentric axial dipole, magnetic and geographic poles coincide. Considering secular variations over a 10 000 year period, the offsets between the magnetic axis and rotational axis average out.

considered elongated magnetic particles which settle with their long axis perpendicular to the direction of gravitation. The particles are assumed to be magnetized along their long axis since this is magnetostatically favorable. The investigation of King (1955) led to a formula relating remanence inclination I_r to the geomagnetic inclination I.

$$\tan I = f \tan I_r \tag{4.2}$$

where $f = 1$ represents no flattening and $f = 0$ maximum flattening of the paleomagnetic signal. A second theoretical model by Griffiths *et al.* (1960) considered spherical grains depositing on an irregular surface. In both models, the typical inclination error varied between 10° and 20°.

Taking into account inclination error solves explanatory problems concerning some sedimentary magnetic records. Investigating paleomagnetic data from the Mediterranean region, Krijgsman and Tauxe (2004) show that correcting shallowed inclinations that have been attributed to either major geographic displacement, non-dipole components of the earth's field or systematic inclination flattening according to existing theory leads to paleogeographically reasonable results. After correction, their data from Spain and Crete match the expected middle Miocene latitudes of the region.

Kent and Tauxe (2005) use a statistical geomagnetic field model to correct for inclination error in records from early Mesozoic reift basins from North America, Greenland and Europe. The corrected data match independent data from igneous rocks ranging over thousands of kilometers and tens of millions of years and indicate that the paleofield corresponded to a geocentric axial dipole in the Late Triassic.

The DEM provides the opportunity to investigate the recorded inclination influencing factors like particle shape, compaction and bedding plane. Additionally, model data with a known error in the inclination can be used to investigate the possibility of mistaking biased recorded inclination for non-dipole components of the geomagnetic field.

Modelling depositional inclination error using the Discrete Element Method

D. Heslop and A. Witt

Universität Bremen, FB Geowissenschaften, Postfach 330440, 28334 Bremen, Germany, Tel. +49-421-218-3933, Fax +49-421-218-7008, Email witt@informatik.uni-bremen.de

Abstract

Palaeomagnetic inclination data and the hypothesis that the time-averaged Geomagnetic field corresponds to a Geocentric Axial Dipole (GAD) form the basis of many geodynamic reconstructions. Errors in depositional inclination are however known to exist in a number of sedimentary systems and when effects such as shallowing bias are unidentified they can produce untenable reconstructions that bring the GAD hypothesis into question.
Sedimentary inclination errors have been successfully identified in natural sediment sequences and recreated in laboratory redeposition experiments. Processes such as compaction and sedimentation onto a tilted bedding plane are known to influence recorded inclinations, however, these mechanisms are still poorly understood on a quantitative level. The discrete element method (DEM) provides a numerical approach to modelling the behavior of sediment particles both above and below the sediment-water interface and can take into consideration post-depositional effects such as compaction. DEM models make it possible to consider not only the mean direction of a sedimentary remanence but also the distribution of magnetic particle orientations. The presented models indicate that external field direction, overlying pressure, particle shape and bedding plane angle are all important factors in controlling both the type and magnitude of sedimentary inclination errors. In addition, it is shown that shallowed inclinations could mistakenly lead to an interpretation for zonal octupole contributions to the palaeofield.
Keywords:

Submitted to EPSL

Introduction

Palaeomagnetic records obtained from sedimentary sequences make a number of essential contributions to the reconstruction of the Earth's history. Information concerning processes such as secular variation, relative palaeointensity, field reversal frequency, the configuration of the ancient field and geodynamics is regularly obtained from the magnetic signal preserved in sedimentary archives. It is however widely accepted that sediments do not provide a perfect record of the ambient field conditions in which they were deposited and the fidelity of different sequences can vary greatly. Although Schneider and Kent (1990) demonstrated that the inclination component of the Natural Remanent Magnetization (NRM) of 185 deep-sea sediment cores did approximately correspond to the inclinations of a Geocentric Axial Dipole (GAD) field, a number of studies have also reported so called *depositional inclination errors*. The commonest form of this error is a shallowing of the sedimentary inclination from the expected GAD direction. Inclination shallowing has been reported in deep-sea sediments (Arason and Levi 1990a), lake sediments (Marco *et al.* 1998), continental sequences (Gilder *et al.* 2003) and is even thought to occur in the alignment of flocced magnetic particles in the water column (van Vreumingen 1993a). Investigations have shown the inclinations recorded in some sediments to be significantly shallower than those recorded in contemporaneous igneous units, providing a strong indication that the shallowing is an artifact of the sedimentary process and not a genuine feature of the Earth's magnetic field (Reynolds 1979; Gilder *et al.* 2003).

Recently, depositional inclination errors have received renewed attention because of the development of a method for the detection of inclination shallowing based on a simplified statistical model for the palaeomagnetic field (Tauxe and Kent 2004). In some cases a slight shallowing of the signal can result in geodynamic reconstructions which are offset by hundreds of kilometers (Krijgsman and Tauxe 2004; Kent and Tauxe 2005; Tauxe 2005). In cases where geodynamic reconstructions from sedimentary sequences produce implausible results it is necessary to either infer that inclination shallowing has taken place or alternatively question the usefulness of a GAD as a long-term representation of the Earth's magnetic field (van der Voo and Torsvik 2001).

Considering the importance of the GAD assumption, it is necessary to consider in detail the processes that could produce depositional inclination errors. A number of laboratory experiments have reported inclination shallowing in redeposited sediments, with some cases having offsets of the magnetic signal greater than 20^o (King 1955; Tauxe and Kent 1984; Levi and Banerjee 1990). Experiment has revealed the importance of compaction in shallowing sedimentary inclinations as overlying pressure overcomes the magnetic torque of the particles and rotates them away from the ambient field direction and into alignment with the bedding plane. One of the first redeposition studies to consider the effects of post-depositional compaction was performed by Blow and Hamilton (1978), who redeposited silty clay grade sediments in both a slurry and grain-by-grain manner to find that compaction of the resulting sediment produced a significant shallowing of the magnetic signal.

Arason and Levi (1990a) confirmed the link between compaction and sedimentary inclination shallowing in natural systems by the statistical analysis of deep-sea sediments from the Pacific ocean. Shallowing of the palaeomagnetic signal observed in a high sedimentation-rate

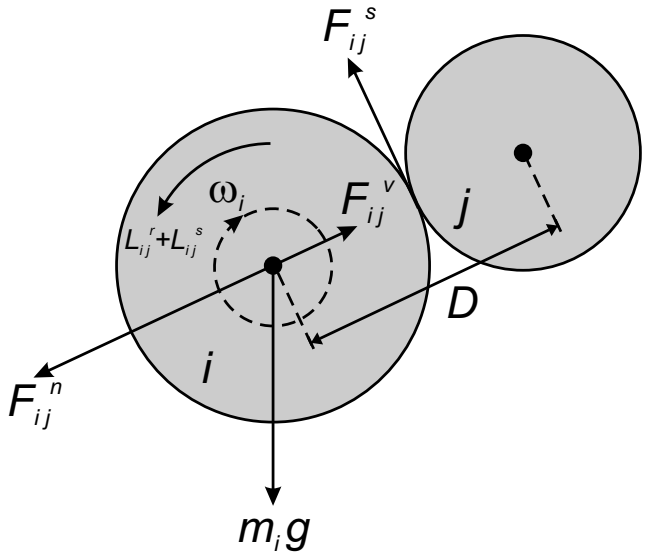

Figure 4.3: Schematic illustration of the forces acting on particle i, which is in contact with particle j. (A) In the soft-body contact model the collision of two particles is represented by allowing a small overlap, $\mathbf{d}_n$, between them. The normal contact force and shear contact force are given by $\mathbf{F}_{ij}^n$, $\mathbf{F}_{ij}^s$, whilst the torques due to the shear force and rolling friction are $\mathbf{L}_{ij}^s$ and $\mathbf{L}_{ij}^r$ respectively, resulting in the rotational velocity, ω_i. The force of gravity acting on particle i is given by $m_i g$. (B) in the viscoelastic contact model the magnitude of the repulsive normal force is related to the overlap of the particles. The loading and unloading phases of the contact produce forces of different magnitudes and thus energy is dissipated during a collision

core obtained at ODP site 578 appeared to increase with depth, therefore indicating a link between inclination error and compaction. At a neighboring location, ODP site 576, which had much lower sedimentation rates than ODP 578 and therefore a lesser burden from overlying sediments, no inclination shallowing was observed.
Theoretical studies such as those of Arason and Levi (1990b) have derived exact mathematical expressions to relate inclination shallowing to compaction. We will consider a numerical approach to modelling the possible mechanisms of depositional inclination error using the Discrete Element Method (DEM) of Cundall and Strack (1979). Previously, the DEM approach has been successfully employed by Witt *et al.* (2005) to model magnetic particle alignment below the sediment-water interface. It is hoped that through the use of a numerical approach it will be possible to simulate more complex systems than those which can be represented analytically and thus provide a more realistic model of sedimentary inclination shallowing.

The discrete element method

Sediment can be considered as a granular material with a structure controlled by processes such as gravity, friction and particle-particle collisions. DEM is a discontinuous simulation method that can provide a representation of the individual motion and mutual interactions of a large population of particles (Cundall and Strack 1979). In the DEM approach, it is assumed that all the forces acting on a particle are known. These forces may originate from

collisions with other particles and immovable bodies or the influence from external factors such as gravitation or a magnetic field. Newton's second law of motion and the force displacement law are implemented iteratively to model the particles' behavior through time. For each iteration, the forces and torques acting on the individual particles are resolved and new positions, velocities and accelerations can be computed for the next iteration. Particles interact through soft-body contacts which produce normal and shear forces according to the nonlinear viscoelastic relationship of Cundall (1987), Figure 4.3. The effects of friction according to Coulomb's law are included in the contact model by limiting the maximum allowable shear force between two particles.

It is known that fluid flow around a particle will produce shear stress and it has previously been reported that sedimentary magnetizations can be influenced by water currents (King 1955). In the presented models, the motion of particles is considered to take place in a vacuum. Whilst the assumption of a vacuum is a rather undesirable simplification it is necessary for a number of reasons. First, the simulation of the motion of a single settling ellipsoid in a fluid is a complicated and time consuming task (Pan *et al.* 2002), therefore to consider large numbers of particles experiencing mutual interactions would be beyond our current processing capacity. Second, although some attempts have been made to consider the effects of interstitial fluids in DEM contact models (Muguruma *et al.* 2000), many aspects of particle-fluid coupling are still poorly understood. The simulations do employ the linear approximation of Cundall and Strack (1979) for friction originating from interstitial fluid which acts to damp both translational and rotational motion of the particles.

At the present time, the simulations are restricted to two-dimensions in order to decrease the required computation time. The earth's magnetic field has both inclination and declination components that cannot be represented simultaneously in a two-dimensional model. Previous studies have suggested that whilst the shifts in inclination of individual grains are not random, thus producing an inclination error, the shifts in declination are random and are thus mutually cancelling (Arason and Levi 1990b). Therefore, an inability to represent declination in the presented models is not considered to be critical. There are other limitations to the reduced dimensionality in terms of the nature of the modelled sedimentary fabric. First, the porosities of two-dimensional sediments cannot be compared properly to those of three-dimensional systems, making it difficult to contrast compaction in the models to that expected for natural sediments. In addition, the absence of percolation in two-dimensions, where small particles migrate though a sediment pack to infill voids, results in fundamentally different fabrics for two and three-dimensional systems. In the future, we hope to extend the model into the third dimension. At the present time however, we consider the modelled sedimentation system to be so simplified compared to the natural processes of sedimentation that any results must be considered as only semi-quantitative. As such, working with a two-dimensional model will be sufficient to capture the essence of the sedimentation process.

Details of the Model

All of the presented DEM models were created using the PFC^{2D} (*Particle Flow Code in 2 Dimensions*) software from HCItasca. The program acts as a computation engine which solves

user-designed simulations. The PFC^{2D} software only allows simulations involving spheres or disks, but particles can be statically combined to produce other simple forms and this feature was utilized in the construction of elongated magnetic grains (Fig. 4.7). The positions of the modelled particles are restricted to the confines of a predefined container which is constructed from immovable *walls* with the same properties as the particles themselves thus resulting in non-periodic boundary conditions (see later diagrams). In order to obtain walls with the same properties as the particles the sides of the container are modelled as particles with infinite mass and radius. The size of the container in each of the models was 5 by 7 μm and the coefficient of friction of each of the walls was set to zero.
The magnetic particles in the simulation were assumed to have infinite anisotropy and to be in the single-domain grain size range. The particles were assigned magnetizations according to an empirical relationship for thermoremanent magnetizations for magnetite produced in a field of 100 μT(Dunlop and Özdemir 1997):

$$M_{tr} = 0.9 \times d^{-1} \tag{4.3}$$

where M_{tr} has units of kA/m and the particle diameter is expressed in μm. All of the spherical non-magnetic particles in the model were created with a radius of 100 nm. The motivation for choosing such small non-magnetic matrix particles is the ability to physically lock the magnetic grains into position. If larger non-magnetic spheres are employed in the model the magnetic grains can easily rotate within the voids of the sediment fabric and a stable remanence does not form. Therefore, the use of such small grains provides a method for representing larger irregular shaped grains using only spheres.
The external field of each DEM simulation was set as 50 μT with a predefined inclination and the magnetic torque acting on any particle could be calculated and included into the model. Such an assemblage of spherical non-magnetic and elongated magnetic particles is an oversimplified representation of a natural sediment, however it provides a number of advantages. First, because the DEM method is designed for spheres, such a basic sediment system allows large numbers of particles to be considered with a reasonable execution time, providing a result that is more statistically representative. Second, by selecting simple geometric particles and discounting many of the more complex depositional and post-depositional processes, such as attractive electrostatic forces, a system can be constructed where the results can be interpreted in terms of the initial model conditions rather than a complex interplay of many competing processes.

For each model, the inclination of the external field was set at a predefined value and an assemblage of magnetic particles with a given aspect ratio and non-magnetic spheres was created within the container, Figure 4.4. These particles were allowed to settle in the base of the container under the influence of gravity. Once settling was completed, the top wall of the container descended to meet the top of the sediment. At this stage the sediment is considered to represent a *random-loose-packing* (RLP) which is typical of particles deposited through a viscous fluid (He *et al.* 1999). With the top wall in place the orientations of the individual magnetic particles were recorded and the top wall was lowered to simulate further compaction of the sediment. Compaction proceeded until a *random-close-packing* (RCP) was achieved where no further compaction could occur without distorting the particles themselves (He *et al.* 1999). Once a RCP state was obtained, the orientations of the

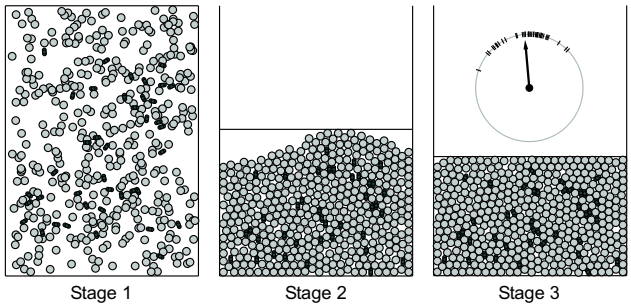

Figure 4.4: The three stages of the DEM model. Elongated magnetic particles (black) and spherical nonmagnetic particles (grey) are created within the container and a predefined external field is invoked (vertical and upwards in this case). The particles are allowed to settle under the influence of gravity to form a random loose packing and the top-wall moves down to meet the surface of the sediment. In the final stage the top-wall applies pressure to the sediment to cause compaction until a random close packing is achieved. The inset panel displays the distribution of magnetic particle orientations plotted on a circle with the arrow representing the mean magnetization vector.

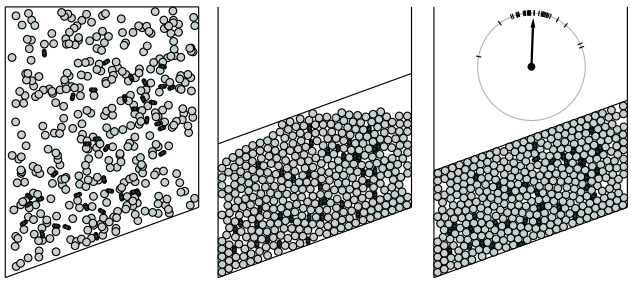

Figure 4.5: The three stages of the DEM model as shown in Figure 4.4. The base and top-wall of the container are tilted at a predefined angle to the horizontal in order to simulate sediment deposition on a slope.

individual magnetic particles were again recorded. We chose to study only these two packing extremes because as previously discussed the porosities of a two-dimensional model cannot be converted into three-dimensional values. Therefore the progression of the compaction through the simulation cannot expressed in terms that can be compared to natural systems. In a post-processing step the particle orientations, θ, were utilized to calculate the mean resultant magnetic vector and standard deviation of the distribution of magnetic particle orientations using the formulas (de Sa 2003):

$$\overline{c} = \sum_{i=1}^{n} \cos\theta_i / n \quad \overline{s} = \sum_{i=1}^{n} \sin\theta_i / n \tag{4.4}$$

The mean resultant vector is given by:

$$\overline{r} = [\overline{c} \quad \overline{s}]' \tag{4.5}$$

with the mean resultant vector length:

$$\overline{r} = \sqrt{\overline{c}^2 + \overline{s}^2} \in [0, 1] \tag{4.6}$$

and mean direction for ($\overline{r} \neq 0$)

$$\overline{\theta} = \begin{cases} \arctan(\overline{s}/\overline{c}), & \text{if} \quad \overline{c} \geq 0 \\ \arctan(\overline{s}/\overline{c}) + \pi sgn(\overline{s}), & \text{if} \quad \overline{c} \ < 0 \end{cases} \tag{4.7}$$

the circular standard deviation, s, is then given by:

$$s = \sqrt{-2 \ln \overline{r}} \tag{4.8}$$

Each simulation consisted of 200 particles of which 40 were magnetic. In order to obtain a representative sample of particle behavior each simulation was repeated 125 times with different particle starting positions, thus providing data on a total of 5000 magnetic particles. The simulation of sedimentation on a slope could be achieved by modifying the shape of the model container, Figure 4.5. At the start of the model the base-wall was tilted at angles of up to 20^o to the horizontal and the particles were created within the confines of the container. The top-wall would then be tilted at the same angle as the base-wall and the simulation would proceed as previously discussed.

Results - testing the DEM model for antisymmetry

The majority of previous studies which have attempted to simulate sedimentary inclination shallowing both experimentally and theoretically have made an assumption of antisymmetry, thus requiring only one sense of inclination (positive or negative) to be investigated. As a first test of the DEM model we investigate if it exhibits antisymmetrical behavior. The model

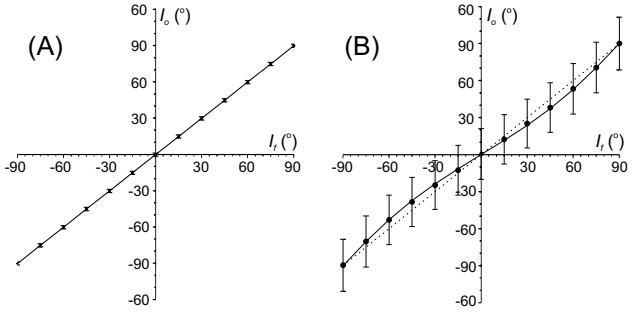

Figure 4.6: Applied field (I_f) versus observed (I_o) inclinations for unconsolidated (A) and compacted (B) sediments. The vertical bars represent ±1 circular standard deviation and the solid lines show the curves fitted according to the inclination error formula (see text). The dashed line in (B) shows the curve f=1.

involved the sedimentation of a collection of elongated magnetic particles with an aspect-ratio (diameter/ length) of 0.5 and spherical non-magnetic particles. Predefined inclinations between -90^o and 90^o (in 15^o increments) were employed as the directional component of the external fields.

A plot of the applied field inclination versus the observed inclination reveals inclination shallowing which is induced when the sediment is compacted, Figure 4.6. Shallowing occurs for both positive and negative inclinations and reaches a maximum value of $\sim 7^o$, whilst the maximum shallowing before compaction is $< 0.01^o$. It is also apparent that the circular standard deviation of the particle orientations increases substantially after compaction reaching magnitudes of $\sim 20^o$. This process of dispersion of the particle orientations still occurs at inclinations of 0^o and $\pm 90^o$ but due to cancellation, the resulting shallowing of the mean direction is minimal. The level of directional shallowing is assessed using the inclination error formula of King (1955) which relates the observed (I_0) and actual field (I_f) inclinations via a flattening parameter, f;

$$\tan(I_0) = f \tan(I_f) \tag{4.9}$$

where f=1 represents no flattening and f=0 represents maximum flattening. The dashed line in Figure 4.6 shows that the data points can be fitted closely with the inclination error formula giving $f = 1$ and 0.76 for the non-compacted and compacted sediments respectively. In order to demonstrate that the DEM model is antisymmetrical, it is necessary to not only consider the mean directions for each field but also the distribution of the magnetic particle orientations. The nonparametric uniform-scores-test for circular data (Mardia and Jupp 2000) was employed to compare the distributions of directions obtained for antipodal fields. To ensure the directions were comparable the distributions of particle orientations for the simulations involving negative inclinations were reflected about $I = 0^o$ before the test was performed. For all the modelled inclinations it was found that the distribution of grain orientations was statistically identical for antipodal fields at a significance level of 0.01. These results indicate that in general the assumption of antisymmetry can be accepted for the DEM model and subsequent simulations are only calculated for external fields in one sense.

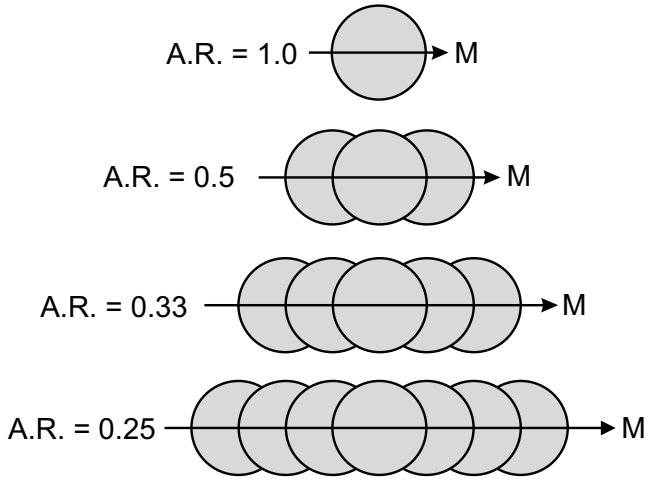

Figure 4.7: Spherical particles are statically combined to form clumps with different aspect ratios ($A.R.$). The magnetization that is assigned to a clump is orientated along its long axis.

Results - the effects of particle aspect ratio

It is well known that magnetic particles with a variety of aspect ratios occur in natural sediments. It would appear reasonable to hypothesize that the greater the elongation of a particle the greater its tendency to align with the bedding plane when subjected to overlying pressure. This hypothesis can be tested using DEM models. Collections of magnetic particles with four different aspect ratios were constructed by the static combination of spheres, Figure 4.7. These elongated particles were then included in particle deposition simulations with non-magnetic spheres in external fields with inclinations ranging between 0 and 90^o.

For the RLP sediments all of the assemblages (except those containing magnetic particles with an aspect ratio of 0.25) successfully record the inclination of the external field. Once the sediment was compacted, all the grain shapes showed an overall shallowing of the mean inclination. The inclinations produced by each grain assemblage are shown in Figure 4.8. Shape played such a dominant role for the most elongated particles that shallowing of the signal was observed before compaction of the sediment, resulting in a flattening factor of $f = 0.91$.

After compaction, the RCP assemblages show a consistently shallower inclination than the previous RLP configuration. The magnitude of the shallowing increases with particle elongation revealing a positive relationship between the aspect ratio and the flattening factor. The magnitude of the circular standard deviation also increases after compaction and apparently as a function of decreasing magnetic particle aspect ratio. Therefore, the magnitude of the final system magnetizations are not controlled solely by external field strength but also by particle shape.

All of the curves can be fitted closely using the inclination error formula and the maximum shallowing is always observed when the external field is at an angle of 45^o. It is interesting to note that the magnitude of the shallowing for the particles with aspect ratios of 0.33 and 0.25 is almost identical. The two assemblages have flattening factors of $\sim$0.68 which is intriguingly

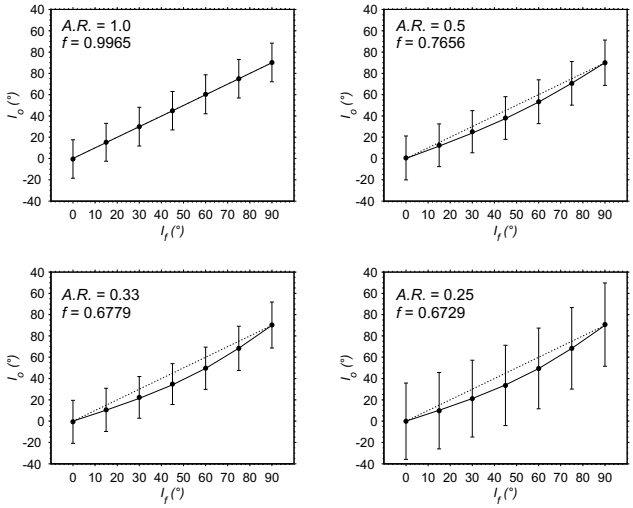

Figure 4.8: Applied field (I_f) versus observed (I_o) inclinations for compacted sediments containing magnetic particles with different A.R. The vertical bars represent ± 1 circular standard deviation and the solid lines show the curves fitted according to the optimum flattening parameter. The dashed line in each panel represents the expected inclinations for f=1.

similar to values (0.68 - 0.7) reported for real sedimentary systems in the Mediterranean by (Krijgsman and Tauxe 2004). It is however not apparent if the simulations are providing a true limit to the effect of particle shape on inclination shallowing of sedimentary systems or if the observed value is simply an artifact of the model. Considering the simplicity of the model and the number of phenomena that are not accounted for, a conservative stance must be adopted and the close correspondence between f values obtained from the model and those from natural data must be assumed to be coincidental.

In cases of natural sediments where inclination shallowing has occurred but remains unidentified the production of untenable geodynamic reconstructions can bring the GAD hypothesis into question. To consider this problem in more detail we investigate the kind of non-dipolar fields that could produce the inclinations that are observed after shallowing has occurred. First, it is important to select a non-dipole field which has a similar form to the shallowed data. A zonal quadrupole field is symmetrical about the equator, however, in contrast to the shallowed directions its maximum offset from a GAD occurs at the equator. A zonal octupole field is more appropriate because it has no offset from a GAD at the equator and is also antisymmetrical about the equatorial plane (van der Voo and Torsvik 2001). Figure 4.9 shows the inclinations expected at different latitudes for a GAD field as a dashed line. The points show the observed inclinations for the shallowed directions obtained from the various DEM models and in each case the data can be fitted closely by inclinations for a GAD field with a small octupole contribution (solid line). This demonstrates that if shallowing processes of the kind produced by the DEM model go unidentified in natural samples it would be possible to mistake the effect for a spurious non-dipole (specifically zonal octupole) field contribution.

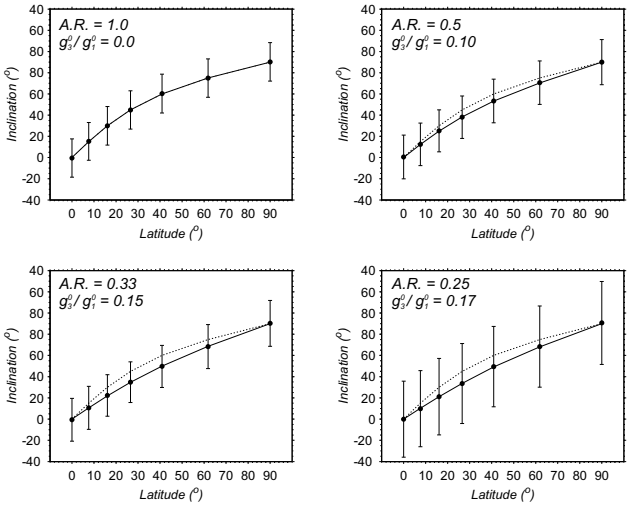

Figure 4.9: Latitudinal dependency of inclinations for compacted sediments containing magnetic particles with different aspect ratios deposited in a GAD field. The data points and vertical bars represent mean directions with ±1 circular standard deviation and can be compared to the expected inclinations for a GAD field (dashed line). The calculation of the inclinations expected for a GAD with a small octupole contribution (solid line) demonstrates that if the shallowing effect went unidentified the observed inclinations could easily be interpreted as a product of non-dipole field behavior. Also shown are the ratios g_3^0/g_1^0 of the Gaussian coefficients which produced the optimum octupole non-dipole field contribution to the fit the data.

Results - deposition on a slope

To investigate the effects of a non-horizontal bedding plane on sedimentary inclination records, models were performed with the bottom-wall of the DEM container positioned at angles of 0, 5, 10, 15 and 20^o to the horizontal. The first series of models considered non-magnetic spheres and elongated magnetic particles (aspect ratio = 0.5) falling in an external field with an inclination of 90^o. As with the previous models, the orientation of the magnetic particles was assessed as the sediment reached RLP and RCP states. The outcome of the models is shown in Figure 4.10. In the RLP state the magnetic particles faithfully record the direction of the ambient field with very little dispersion in their orientations. After compaction, however, the angle of the static bottom-wall and compressing top-wall play a role in controlling the final mean inclination of the magnetic particle assemblage. It appears that a linear relationship exists between the inclination of the sediment and the angle of the slope onto which the particles were deposited. This result is supported by previous investigations of natural sediments which revealed a linear relationship between the inclination error of varved sediments and the tilt of the bedding plane onto which they had been deposited (Rees 1964). The DEM provides additional information showing the angular dispersion of the model particles as represented by the circular standard deviation appears to be related to the angle of the slope in some nonlinear manner, Figure 4.10.

The series of simulations was repeated for an external field with an inclination of 0^o. As with the vertical field, the magnetic particles almost perfectly record the inclination of the field before compaction. After compaction, the recorded inclination increases leading to a steepening of the magnetic signal. The circular standard deviations again appear to follow

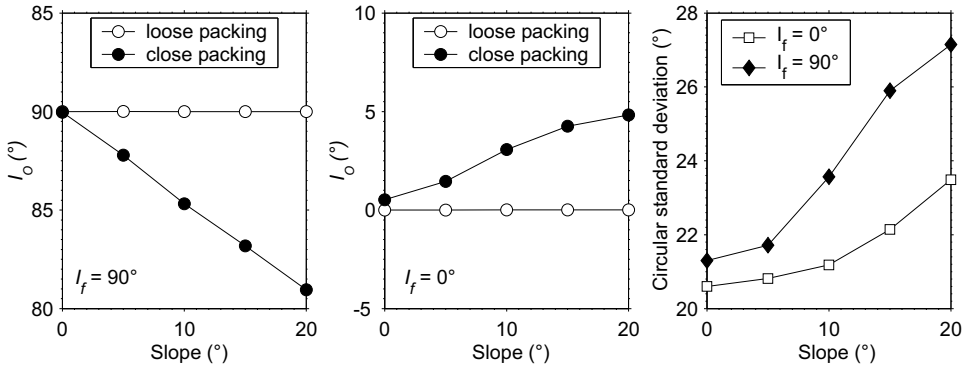

Figure 4.10: The effect of bedding plane angle on the inclination recorded by compacted sediments. The first two panels show the situation for external field inclinations of 90 and 0^o. In addition, it appears in the final panel that the dispersion of the magnetic particle orientations increases in magnitude with the steepness of the slope.

a nonlinear relationship with respect to the angle of the slope.
It is apparent from these results that the final inclination of compacted sediment is a function both of the angle of the slope on which deposition takes place and the inclination of the field. It is also important to note that the simulations performed with a horizontal field demonstrate that under appropriate conditions the inclination can undergo a steepening rather than shallowing. It would therefore seem to be more appropriate to refer to a *depositional inclination error* when considering the remanence of sediments deposited on a slope.

Conclusions

The numerical approach of DEM demonstrates a number of points concerning detrital inclination error. The presented models consider only a simple particle system which ignores the effects of sedimentary processes such as flocculation in the water column, bioturbation and diagenesis. However, a number of aspects of the results from our simple numerical approach appear to indicate that the model at least partially captures the essence of some aspects of detrital inclination error. First, all the model results show flattening factors which are well within the range of those reported for both natural sediments and laboratory redeposition experiments. Second, when inclination shallowing is considered as a function of field direction, the model results could always be fitted closely by the inclination error formula. It also appears that the form of shallowing which occurs as a function of latitude could easily be mistaken for the influence of non-dipole (zonal octupole) field contributions if a depositional inclination error is not identified.
In the limited case of a simple system consisting of spherical sediment particles it is evident that overlying pressure has the effect of rotating elongated magnetic particles into partial alignment with the bedding-plane. Although this result is expected from the work of previous studies, the DEM approach also provides information on the distributions of particle orientations after compaction as well as mean directions. Finally, detrital inclination error should not always be considered in terms of inclination shallowing. The DEM models demonstrate

that deposition of sediment on a moderately tilted slope in the presence of shallow external field can result in a steepening of the observed inclination.

Summary

Numerical models in geoscience have to be simple enough to understand but still complex enough to represent real processes. If a numerical model were a perfect copy of the real process it represents, it would have the same drawbacks as a map of a city which is as big as the city itself and includes every house, tree and inhabitant. Such a map would completely lose its purpose to abstract and generalize (Gleick 1987).
In this sense, investigating recording mechanisms of magnetic grains using micromagnetic modelling as well as the numerical investigations of post-depositional remanence and depositional remanence influencing processes with a discrete element method are successful, and lead to results that are in good accordance with experimentally observed behavior.

Micromagnetics

As shown in chapter 2, micromagnetic modelling of irregularly shaped particles confirms the shape dependence of domain structure in magnetite particles and thus can explain the size range of magnetosomes in sediments as observed by Petersen *et al.* (1989). Previous micromagnetic models of rectangular particles led to the conclusion that some magnetosomes cannot even carry a meta-stable single domain remanence. The ability to carry a stable magnetization is crucial for magnetotactic bacteria to navigate through the water column properly. The discovery of magnetosomes that are in size beyond the meta-stable single domain size range for rectangular magnetite could have two reasons. First, interaction within the chains of magnetosomes could lead to a stabilization of the single domain state within a chain. Second, the irregular shape of the single magnetosomes could enlarge the meta-stable single domain region. Modelling irregularly shaped magnetosomes shows that the mechanism is one possibility for explaining the ability of large grains to stay in a single domain range. Taking into consideration irregular shape, all large magnetosomes from Petersen *et al.* (1989) fall into the meta-stable single domain range.
Additionally, micromagnetic investigation of euhedral magnetite shows that octahedral single domain particles can be considerably larger in size than meta-stable rectangular single domain particles.

PDRM and DRM acquisition

The newly introduced discrete element method (DEM) is a powerful tool in numerically investigating magnetic remanence properties of a sediment. Here, the main task is the basic design of a first sediment model to investigate processes influencing depositional and post-depositional remanence acquisition. While modelling an assemblage of non-interacting particles is an easy task, the difficulty in modelling real sediment behavior lies in the large number of interacting particles. The discrete element method provides an efficient way of treating these particle interactions.
The purpose of the models concerning depositional and post-depositional remanence acquisition in chapter 3 is to demonstrate that numerical modelling is now able to simulate complex sediment assemblages including particle interactions. The considered models enable the investigation of the influence of external field strength, compaction, particle shape and

particle aggregation on the level of acquired magnetization. The results of these models are in good accordance with experimentally observed behavior. Investigations of the influence of particle aggregation on the level of acquired remanence show that flocculation restricts the perfect alignment of magnetic particles in the water column. In contrast to experimental observations, theoretical models that do not consider particle aggregation predict a perfect alignment of magnetic particles after just a few centimeters in the water column. The numerical models reveal a way of resolving these contradictions.

Inclination error

The DEM provides the opportunity to generate a model sediment with known errors in the recorded inclination, as demonstrated in chapter 4. The model sediment allows also for the investigation of influences like particle shape, compaction and angle of the bedding plane on the recorded inclination. Here, the model results are again in good accordance with formerly observed natural behavior. Numerically modelled shallowed inclination almost perfectly matches non-shallowed inclination of a geomagnetic field with small octupole components. This demonstrates the possibility of mistaking undiscovered inclination error for non-dipole components of the geodynamo.

Future studies

So far, the discrete element models demonstrate the possibility of numerically modelling interacting and realistic sediment assemblages. Although the investigated processes are still basic they lay the base for more realistic future investigations. Moving from two to three dimensions and changing the basic particle shape from spherical to elliptical will improve the model's ability to resemble natural processes. Additionally, there will be the challenge to include fluid coupling in the model sediments. A fully quantitative, three-dimensional model including fluid coupling and realistic particle shapes can eventually lead to predictions concerning magnetic remanence properties of a sediment. Such development of these models will lead to insight into the complicated mechanisms of depositional and post-depositional remanence acquisition and might eventually help to fully understand puzzling magnetization records as found by Bleil and von Dobeneck (1999).

Zusammenfassung

Numerische Modelle in den Geowissenschaften sollten so einfach sein, daß man sie verstehen kann, dem modellierten, komplexen, natürlichen Prozeß aber trotzdem entsprechen. Eine detailgetreue Nachbildung eines natürlichen Prozesses hätte dieselben Nachteile wie ein Stadtplan, der so groß wie die Stadt selbst ist und alle Häuser, Bäume und Einwohner beinhaltet. Ein solcher Stadtplan hätte sein Ziel, zu verallgemeinern und zu abstrahieren verfehlt (Gleick 1987).
In diesem Sinn waren die numerischen Untersuchungen der möglichen Größen von Magnetiteinbereichsteilchen, die hier vorgestellten numerischen Modellierungen des sedimentären Remanenzerwerbs sowie das Modellieren magnetischer Inklinationsfehler erfolgreich. Die Ergebnisse stimmen gut mit experimentell beobachteten Werten überein.

Mikromagnetik

Die in Kapitel 2 durchgeführten mikromagnetischen Modellrechnungen an unregelmäßig geformten Teilchen bestätigen die Formabhängigkeit der Magnetisierungsstruktur in Magnetitteilchen und liefern eine Erklärung für die von Petersen *et al.* (1989) gefundenen Magnetosomengrößen. Mikromagnetische Modelle rechteckiger Teilchen zeigten, daß einige der von Petersen *et al.* (1989) gefundenen Magnetosomen nicht einmal eine metastabile Einbereichsteilchenremanenz tragen können. Die Fähigkeit, stabile Remanenz zu tragen, ist für magnetotaktische Bakterien notwendig, um sich in der Wassersäule orientieren zu können. Funde von Magnetosomen, die größer als metastabile rechteckige Magnetiteinbereichsteilchen sind, lassen verschiedene Interpretationen zu. Wechselwirkungen in der Magnetosomenkette könnten zu einer Stabilisierung der Einbereichsteilchen in der Kette führen. Eine weitere mögliche Erklärung könnte die unregelmäßige Form der Teilchen sein, die ein Ausweiten des metastabilen Bereichs bewirkt. Mikromagnetische Modellrechnungen, welche die Form der Teilchen miteinbeziehen, zeigen, daß Formunregelmäßigkeit eine mögliche Erklärung für eine Ausdehnung des metastabilen Bereichs von Einbereichsteilchen ist. Berücksichtigt man Formunregelmäßigkeit bei den von Petersen *et al.* (1989) gefundenen Teilchen, sind alle großen Magnetosomen zumindest im metastabilen Bereich.
Mikromagnetische Berechnungen für natürlich vorkommenden, oktaedrischen Magnetit zeigen außerdem, daß dieser ebenfalls beträchtlich größer werden kann als kubischer Magnetit ohne als Remanenzträger instabil zu sein.

PDRM und DRM Erwerb

Die hier vorgestellten numerischen Untersuchungen zeigen, daß die Diskrete-Elemente-Methode erfolgreich zur Untersuchung magnetischer Sedimenteigenschaften eingesetzt werden kann. Das hauptsächliche Ziel war die Entwicklung eines ersten Modellsediments zur numerischen Untersuchung des sedimentären Remanenzerwerbs.
Während das Modellieren eines nicht-wechselwirkenden Teilchensystems einfach ist, treten beim Modellieren wechselwirkender Sedimente Schwierigkeiten auf. Die Diskrete-Elemente-Methode bietet eine gute und effektive Möglichkeit, beim Modellieren selbst großer Teilchensysteme Wechselwirkungen zu berücksichtigen.

Der Zweck der sedimentären Remanenzerwerbs-Modelle in Kapitel 3 ist es, ein komplexes Sediment mit Teilchenwechselwirkungen realistisch zu modellieren. Mit dem modellierten Teilchensystem können Einflüsse von Stärke des externen Felds, Teilchenform, Kompaktion und Teilchenaggregation auf den Grad der erworbenen Magnetisierung untersucht werden. Die Ergebnisse dieser Modellrechnungen stimmen gut mit experimentellen Beobachtungen überein. Untersuchungen des Einflusses von Teilchenaggregation auf die erworbene Remanenz zeigen, daß Flockenbildung eine perfekte Ausrichtung der magnetischen Teilchen in der Wassersäule verhindern kann. Theoretischen Modellen zufolge, die Aggregation von Teilchen nicht berücksichtigen, sollten magnetische Teilchen in der Wassersäule schon nach wenigen Zentimetern des Absinkens perfekt ausgerichtet sein. Experimentelle Beobachtungen zeigen allerdings, daß dies nicht der Fall ist. Die numerischen Modelle bieten nun eine Möglichkeit, den Widerspruch zwischen Theorie und experimentellen Daten zu erklären.

Inklinationsfehler

In Kapitel 4 wird gezeigt, daß mit der Diskreten-Elemente-Methode Modellsedimente mit bekannten Inklinationsfehlern in der Magnetisierung erzeugt werden können. Mit dem künstliche Sediment können außerdem Einflüsse von Teilchenform, Kompaktion und Kippwinkel der Ablagerungsebene auf die gespeicherte Inklination untersucht werden. Auch hier decken sich die Modellergebnisse gut mit früheren experimentellen Beobachtungen. Es kann gezeigt werden, daß numerisch modellierte fehlerbehaftete Inklinationsdaten nahezu perfekt mit Oktopolkomponenten des Erdmagnetfelds erklärt werden können. Dies demonstriert, daß nicht erkannte Inklinationsfehler für Komponenten des Paläomagnetfelds, die nicht dipolaren Ursprungs sind, gehalten werden können.

Ausblick

Bis jetzt haben die Diskreten-Elemente-Modelle gezeigt, wie numerisch wechselwirkende und realistische Sedimente modelliert werden können. Obwohl die hier betrachteten Modelle noch sehr einfach sind, bilden sie die Grundlage für detailliertere und realistischere zukünftige Untersuchungen. Der Weg von zwei- zu dreidimensionalen Modellen und ein Wechsel der Teilchengrundform von kugelförmig zu elliptisch wird die Modellierung realitätsgetreuer gestalten. In künftigen Modellen soll auch hydrodynamische Kopplung berücksichtigt werden. Ein quantitatives, dreidimensionales Modell mit hydrodynamischer Kopplung und realistischen Teilchenformen könnte später einmal die Vorhersage Remanenz-magnetischer Eigenschaften eines Sediments ermöglichen. So können in Zukunft Einblicke in die komplizierten Mechanismen des sedimentären Remanenzerwerbs gewonnen werden, mit deren Hilfe vielleicht rätselhafte magnetische Signale wie die von Bleil und von Dobeneck (1999) gefundenen verstanden werden könnten.

Danksagung

Die vorliegende Arbeit wurde in der Arbeitsgruppe Geophysik im Fachbereich Geowissenschaften der Universität Bremen erstellt. Danken möchte ich Herrn Prof. Dr. U. Bleil, Dr. K. Fabian und Prof. Dr. T. von Dobeneck für die Vergabe und Betreuung dieser Arbeit und ihre stete Diskussionsbereitschaft. Bei Herrn Prof. Dr. M. Schulz bedanke ich mich für die bereitwillige Übernahme des Zweitgutachtens. Ein besonderer Dank gilt Dr. D. Heslop als ständigem und geduldigem Ansprechpartner, für die gute Zusammenarbeit und die vielen Diskussionen.

Erklärung

Hiermit versichere ich, daß ich die Arbeit ohne unerlaubte fremde Hilfe angefertigt habe, keine anderen als die von mir angegebenen Quellen und Hilfsmittel benutzt habe und die den benutzten Werken wörtlich entnommenen Stellen als solche kenntlich gemacht habe.

Bremen, den 2.5.2005

Bibliography

1 Amar, H. (1958). Size dependence of the wall characteristics in a two-domain iron particle. *J. Appl. Phys.*, **29**, 542–543.

2 Arason, P. and Levi, S. (1990a). Compaction and inclination shallowing in deep-sea sediments from the pacific ocean. *Journal of Geophysical Research*, **95**, 4501–4510.

3 Arason, P. and Levi, S. (1990b). Models of inclination shallowing during sediment compaction. *Journal of Geophysical Research*, **95**, 4481–4499.

4 Barber, C. B., Dobkin, D. P., and Huhdanpaa, H. T. (1996). The quickhull algorithm for convex hulls. *ACM Trans. Math. Software*, page http://www.geom.umn.edu/locate/qhull.

5 Barton, C. E., McElhinny, M. W., and Edwards, D. J. (1980). Laboratory studies of depositional drm. *Geophysical Journal of the Royal Astronomical Society*, **61**.

6 Bennett, R. H., O'Brien, N. R., and Hulbert, M. H. (1991). Determinants of clay and shale microfabric signatures: Processes and mechanisms. In *Microstructure of Fine-Grained Sediments, From Mud to Shale*.

7 Berkov, D., Ramstöck, K., Leibl, T., and Hubert, A. (1993a). Numerical micromagnetics in low-anisotropy materials. *IEEE Trans. Magn.*, **29**(6), 2548–2550.

8 Berkov, D., Ramstöck, K., Leibl, T., and Hubert, A. (1993b). Solving micromagnetic problems: Towards an optimal numerical method. *Phys. Stat. Sol.*, **A 137**(6), 207–225.

9 Blakemore, R. P. (1975). Magnetotactic bacteria. *Science*, **190**, 377–379.

10 Blakemore, R. P. (1982). Magnetotactic bacteria. *Annual Review of Microbiology*, **36**, 217 – 238.

11 Bleil, U. and von Dobeneck, T. (1999). Geomagnetic events and relative paleointensity records - clues to high-resolution paleomagnetic chronostratigraphies of late quarternary marine sediments? *Use of Proxies in Oceanography: Examples from the South Atlantic*.

12 Blow, R. A. and Hamilton, N. (1978). Effect of compaction on the acquisition of a detrital remanent magnetization in fine-grained sediments. *Geophysical Journal of the Royal Astronomical Society*, **52**, 13–23.

13 Boggs, S. (2000). *Principles of Sedimentology and Stratigraphy*. Prentice Hall.

14 Brown, W. F. (1963). Thermal fluctuations of a single-domain particle. *Phys. Rev.*, **130**, 1677–1686.

15 Butler, R. F. (1998). *PALEOMAGNETISM: Magnetic Domains to Geologic Terranes*. Department of Geosciences, University of Arizona, http://www.earth.rochester.edu/butlerbook/.

16 Butler, R. F. and Banerjee, S. K. (1975). Theoretical single-domain grain size range in magnetite and titanomagnetite. *J. Geophys. Res.*, **80**, 4049 – 4058.

17 Channel, J. and Guyodo, Y. (2004). *Timescales of the Paleomagnetic Field*, volume 145 of *Geophysical Monograph Series*, chapter The Matuyama Chronozone at ODP Site 982 (Rockall Bank): Evidence for Decimeter-Scale Magnetization Lock-in Depths, pages 205–219. American Geophysical Union.

18 Channell, J. (1989). *The Encyclopedia of Solid Earth Geophysics*, chapter Paleomagnetism: Deep-sea sediments, pages 889–891. Van Norstrand, New York.

19 Collinson, D. W. (1965). Depositional remanent magnetization in sediments. *J. Geophys. Res.*, **70**, 4663–4668. IRM library.

20 Cundall, P. A. (1987). *Analytical and Computational Methods in Engineering Rock Mechanics*, chapter Distinct Element Models of Rock and Soil Structure, Chapter 4, pages 129–163. George Allen and Unwin, London.

21 Cundall, P. A. and Strack, O. D. L. (1979). A discrete numerical model for granular assemblies. *Géotechnique*, **29**, 47–69.

22 Currie, I. G. (1974). *Fundamental mechanics of fluids*. McGraw-Hill Book Company.

23 de Sa, J. P. M. (2003). *Applied Statistics using SPSS, Statistica and Matlab*. Springer.

24 Debye, P. (1929). *Polare Molekeln*. Leipzig: Hirzel.

25 deMenocal, P., Ruddiman, F., and Kent, D. (1990). Depth of post-depositional remanence acquisition in deep-sea sediments: a case study of the brunhes-matuyama reversal and oxygen isotope stage 19.1. *Earth Planet. Sci. Lett.*, **99**, 1–13.

26 Deresiewicz, H. (1958). *Advances in Applied Mechanics*, volume 5, chapter Mechanics of Granular Matter, pages 233–306. Academic Press, New York.

27 Dunlop, D. (1973). Superparamagnetic and single-domain threshold sizes in magnetite. *J. Geophys. Res.*, **78**, 1780–1793.

28 Dunlop, D. (1990a). Developments in rock magnetism. *Rep. Prog. Phys.*, **53**, 707–792.

29 Dunlop, D. (1995). Magnetism in rocks. *J. Geophys. Res.*, **100**, 2161–2174.

30 Dunlop, D. J. (1990b). Developments in rock magnetism. *Rep. Prog. Phys.*, **53**, 707–792.

31 Dunlop, D. J. and Argyle, K. S. (1997). Thermoremanence, anhysteretic remanence and susceptibility of submicron magnetites: Nonlinear field dependence and variation with grain size. *J. Geophys. Res.*, **102**(B9), 20199–20210.

32 Dunlop, D. J. and Özdemir, Ö. (1997). *Rock Magnetism, Fundamentals and frontiers*. Cambridge Studies in Magnetism. Cambridge University Press.

33 Dunlop, D. J. and West, G. F. (1969). An experimental evaluation of single domain theories. *Rev. Geophys.*, **7**(4), 709–757.

34 Dyer, K. (1994). *Sediment Transport and Depositional Processes*, chapter Estuarine sediment transport and deposition, pages 193–218. Blackwell Scientific Publications.

35 Eisma, D. (1986). Flocculation and de-flocculation of suspended matter in esturies. *Neth. J. Sea Res.*, **20**, 183–199.

36 Fabian, K. (1998). *Neue Methoden der Modellrechnung im Gesteinsmagnetismus*. Akademischer Verlag, München.

37 Fabian, K. and Hubert, A. (1999). Shape-induced pseudo-single domain remanence. *Geophys. J. Int.*, **138**, 717 – 726.

38 Fabian, K., Kirchner, A., Williams, W., Heider, F., Leibl, T., and Hubert, A. (1996). Three-dimensional micromagnetic calculations for magnetite using fft. *Geophys. J. Int.*, **124**, 89–104.

39 Fannin, P. C., Charles, S. W., and Relihan, T. (1995). On the influence of inertial effects, arising from rotational brownian motion, on the complex susceptibility of ferrofluids. *Journal of Physics D: Applied Physics*, **28**, 1765–1769.

40 Fassbinder, J. W. E., Stanjek, H., and Vali, H. (1990). Occurence of magnetic bacteria in soil. *Nature*, **343**, 161–163.

41 Fidler, J. and Schrefl, T. (2000). Micromagnetic modelling – the current state of the art. *J. Phys. D*, **33**, R135 – R156.

42 Fletcher, E. J. and OReilly, W. (1974). Contribution of Fe_2^+ ions to the magnetocrystalline anisotropy constant K_1 of $Fe_{3-x}Ti_xO_4$ ($0 < x < 0.1$). *J. Phys. C*, **7**, 171–178.

43 Franke, C., Hofmann, D., and von Dobeneck, T. (2004). Does lithology influence relative paleointensity records? a statistical analysis on South Atlantic pelagic sediments. *Physics of the Earth and Planetary Interiors*, **147**, 285–296.

44 Frigo, M. and Johnson, S. G. (1998). FFTW: an adaptive software architecture for the FFT. volume 3, pages 1381–1384.

45 Gerthsen, C. (1995). *Physik*. Springer-Verlag.

46 Gerthsen, C. and Vogel, H. (1993). *Physik*. Springer-Verlag.

47 Gibbons, M. R., Parker, G., Cerjan, C., and Hewett, D. W. (2000). Finite difference micromagnetic simulation with self-consistent currents and smooth surfaces. *Physica B*, **275**(1-3), 11–16.

48 Gilder, S., Chen, Y., Cogné, J.-P., Tan, X., Courtillot, V., Sun, D., and Li, Y. (2003). Paleomagnetism of upper jurassic to lower cretaceous volcanic and sedimentary rocks from the western tarin basin and implications for inclination shallowing and absolute dating of the M-0 (ISEA?) chron. *Journal of Geophysical Research*, **206**, 587–600.

49 Gleick, J. (1987). *CHAOS, THE AMAZING SCIENCE OF THE UNPREDICTABLE.* Vintage.

50 Griffiths, D. H., King, R. F., Rees, A. I., and Wright, A. E. (1960). The remanent magnetization of some recent varved sediments. *Proc. Roy. Soc. London*, pages 359–383.

51 Hahn, H. K., Link, F., and Peitgen, H. O. (2003). Concepts for rapid application prototyping in medical image analysis and visualization. *Proc. SimVis-Simulation & Visualisierung*, pages 283–298.

52 Hamaker, H. C. (1937). The london-van der waals attraction between spherical particles. *Physica*, **4**, 1058.

53 Hanzlik, M. (1999). *Elektronenmikroskopische und magnetomineralogische Untersuchungen an magnetotaktischen Bakterien des Chiemsees und an bakteriellem Magnetit eisenreduzierender Bakterien.* Ph.D. thesis, University of Munich.

54 Hanzlik, M., Winklhofer, M., and Petersen, N. (1996). Spatial arrangement of chains of magnetosomes in magnetotactic bacteria. *Earth Planet. Sci. Lett.*, **145**, 125–134.

55 He, D., Ekere, N. N., and Cai, L. (1999). Computer simulation of random packing of unequal particles. *Physical Review E*, **60**, 7098–7104.

56 Heider, F., Halgedahl, S. L., and Dunlop, D. J. (1988). Temperature dependence of magnetic domains in magnetite crystals. *Geophys. Res. Lett.*, **15**, 499–502.

57 Hofmann, D. I. and Fabian, K. (2005). A stratigraphic network from the subtropical and subantarctic south atlantic: Rock magnetism and oceanography. in preparation.

58 Hubert, A. (1988). The role of "magnetization swirls" in soft magnetic materials. *J. de Phys.*, **49**, 1859–1864.

59 Hubert, A. and Schäfer, R. (1998). *Magnetic Domains.* Springer, Berlin, Heidelberg, New York.

60 Inselberg, A. (1985). The plane with parallel coordinates. *The Visual Computer*, **1**, 69–91.

61 Irving, E. and Major, A. (1964). Post-depositional detrital remanent magnetization in a synthetic sediment. *Sedimentology*, **3**, 135–143.

62 Itasca (2002). *PFC2D Partcile Flow Code in 2 Dimensions User's Guide.* Itasca Consulting Group, Inc., Thresher Square East, 708 South Third Street, Suite 310, Minneapolis, Minnesota 55415 USA, second edition.

63 Johnson, E. A., Murphy, T., and Torreson, O. W. (1948). Pre-history of the earths magnetic field. *Terr. Mag. Atmos. Elec.*, **53**, 349–372.

64 Johnson, H. P., Kinoshita, H., and Merrill, R. T. (1975). Rock magnetism and paleomagnetism of some north pacific deep-sea sediments. *Geol. Soc. of America Bull.*, **86**, 412–420.

65 Joos, G. (1959). *Lehrbuch der theoretischen Physik*. Akademische Verlagsgesellschaft M.B.H. Frankfurt am Main.

66 Karlin, R. and Levi, S. (1985). Geochemical and sedimentological control of the magnetic properties of hemipelagic sediments. *J. Geophys. Res.*, **90**, 10.373–10.392.

67 Katari, K. and Bloxham, J. (2001). Effects of sediment aggregate size on DRM intensity: a new theory. *Earth Planet. Sci. Lett.*, **186**(1), 113–122.

68 Katari, K. and Tauxe, L. (2000). Effects of pH and salinity on the intensity of magnetization in redeposited sediments. *Earth Planet. Sci. Lett.*, **181**, 489–496.

69 Kent, D. and Tauxe, L. (2005). Corrected Late Triassic Latitudes for Continents Adjacent to the North Atlantic. *Science*, **307**, 240–244.

70 Kent, D. V. (1973). Post depositional remanent magnetization in deep sea sediments. *Nature*, **246**, 32–34.

71 King, R. F. (1955). The remanent magnetisation of artifically deposited sediments. *Mon. Nat. Roy. astr. Soc., Geophys. Suppl.*, **7**, 115–134.

72 Kittel, C. (1949). Physical theory of ferromagnetic domains. *Rev. Mod. Phys.*, **21**, 541–583.

73 Kranck, K. (1991). Interparticle grain size relationships resulting from flocculation. In *Microstructure of Fine-Grained Sediments, From Mud to Shale*.

74 Krijgsman, W. and Tauxe, L. (2004). Shallow bias in mediterranean paleomagnetic directions caused by inclination error. *Earth and Planetary Science Letters*, **222**, 685–695.

75 Landau, L. and Lifshitz, E. (1935). On the theory of the dispesion of magnetic permeability in ferromagnetic bodies. *Physik. Z. Sowjetunion*, pages 53–169.

76 Levi, S. and Banerjee, S. (1990). On the origin of inclination shallowing in redeposited sediments. *Journal of Geophysical Research*, **95**, 4383–4389.

77 Levi, S. and Merrill, R. (1976). A comparison of ARM and TRM in magnetite. *Earth Planet. Sci. Lett.*, **32**, 171–184.

78 Levi, S. and Merrill, R. T. (1978). Properties of single domain, pseudo-single domain, and multidomain magnetite. *J. Geophys. Res.*, **83**, 309 – 323.

79 Lovlie, R. (1989). Magnetization of sediments and depositional environment. *Geomagnetism and Paleomagnetism*, pages 243–252.

80 Lu, R., Banerjee, S., and Marvin, J. (1990). Effects of clay mineralogy and the electrical conductivity of water on the acquisition of depositional remanent magnetization in sediments. *Journal of Geophysical Research B: Solid Earth*, **95**, 4531–4538.

81 Mann, S. (1985). Structure, morphology, and crystal growth of bacterial magnetite. In J. L. Kirschvink, D. S. Jones, and B. J. Macfadden, editors, *Magnetite Biomineralization and Magnetoreception in Organisms: A New Biomagnetism*, pages 311–332. Plenum Press, New York.

82 Marco, S., Ron, H., McWilliams, M. O., and Stein, M. (1998). High-resolution record of geomagnetic secular variation from late pleistocene lake lisan sediments (paleo dead sea). *Earth Planet. Sci. Lett.*, **161**(1-4), 145–160.

83 Mardia, K. and Jupp, P. (2000). *Directional Statistics*. John Wiley and Sons, Inc.

84 McCartney, M. R., Lins, U., Farina, M., Buseck, P. R., and Frankel, R. B. (2001). Magnetic microstructure of bacterial magnetite by electron holography. *Eur. J. Mineral.*, **13**, 685–689.

85 Moskowitz, B. and Halgedahl, S. (1987). Theoretical temperature and grain-size dependence of domain state in x=0.6 titanomagnetite. *J. Geophys. Res.*, **92**, 677–682.

86 Muguruma, Y., Tanaka, T., and Tsuji, Y. (2000). Numerical simulation of particulate flow with liquid bridge between particles (simulation of centrifugal tumbling granulator). *Powder Technology*, **109**, 49–57.

87 Muxworthy, A. R., Dunlop, D. J., and Williams, W. (2003). High-temperature magnetic stability of small magnetite particles. *J. Geophys. Res.*, **108**(B5), doi:10.1029/2002JB002195.

88 Nagata, T. (1961). *Rock Magnetism*. Mazuren Company Ltd.

89 Néel, L. (1949). Théorie du traînage magnétique des ferromagnétiques en grains fins avec applications aux terres cuites. *Ann. Geophys.*, **5**, 99–136.

90 Newell, A. J. (2000). The lowrie-fuller test: single-domain and micromagnetic theory. *Earth Planet. Sci. Lett.*, **183**(1), 335–346.

91 Newell, A. J. and Merrill, R. T. (2000). Nucleation and stability of ferromagnetic states. *J. Geophys. Res.*, **105**(B8), 19377–19391.

92 Otofuji, Y. and Sasajima, S. (1981a). A magnetization process of sediments: laboratory experiments on post-depositional remanent magnetization.

93 Otofuji, Y. and Sasajima, S. (1981b). A magnetization process of sediments: laboratory experiments on post-depositional remanent magnetization. *Geophys. J. R. astr. Soc.*, **66**, 241–259.

94 Pan, T.-W., Glowinski, R., and Galdi, G. (2002). Direct simulation of the motion of a settling ellipsoid in newtonian fluid. *Journal of Computational and Applied Mathematics*, **149**, 71–82.

95 Petermann, H. (1994). *Magnetotaktische Bakterien und ihre Magnetosome*. Ph.D. thesis, University of Bremen.

96 Petermann, H. and Bleil, U. (1993). Detection of live magnetotactic bacteria in south atlantic deep-sea sediments. *Earth Planet. Sci. Lett.*, **117**, 223–228.

97 Petersen, N., Dobeneck, T., and Vali, H. (1986). Fossil bacterial magnetite in deep-sea sediments from the south atlantic ocean. *Nature*, **320**, 611–615.

98 Petersen, N., Weiss, D., and Vali, H. (1989). Magnetotactic bacteria in lake sediments. In F. Lowes, editor, *Geomagnetism and Paleomagnetism*, pages 231 – 241. Kluwer Academic Publishers, Dordrecht. BGCM.

99 Press, W. H., Flannery, B. P., Teukolsky, S. A., and Vetterling, W. T. (1992). *Numerical Recipes in C: The Art of Scientific Computing*. Cambridge University Press.

100 Quidelleur, X., Valet, J.-P., LeGoff, M., and Bouldoire, X. (1995). Field dependence on magnetization of laboratory-redeposited deep-sea sediments: first results. *Earth Planet. Sci. Lett.*, **133**, 311–325.

101 Rave, W., Fabian, K., and Hubert, A. (1998). Magnetic states of small cubic particles with uniaxial anisotropy. *J. Magn. Magn. Mater.*, **190**, 332–348.

102 Rees, A. I. (1964). Measurement of the natural remanent magnetism and anisotropy of susceptibility of some swedish glacial silts. *Geophysical Journal*, **8**, 356–369.

103 Reynolds, R. (1979). Comparison of the TRM of the yellowstone group and the DRM of some pearlette ashbeds. *Journal of Geophysical Research*, **84**, 4525–4532.

104 Rhodes, P. and Rowlands, G. (1954). Demagnetising energies of uniformly magnetised rectangular blocks. *Proc. Leeds Phil. and Lit. Soc.*, pages 191–210.

105 Roberts, A. P., Pike, C. R., and Verosub, K. L. (2000). First-order Reversal Curve Diagrams: A new tool for characterizing the magnetic properties of natural samples. *Journal of Geophysical Research*, **105(B12)**, 28461–28475.

106 Schabes, M. E. and Bertram, H. N. (1988). Magnetization processes in ferromagnetic cubes. *J. Appl. Phys.*, **64**, 1347–1357.

107 Schneider, D. A. and Kent, D. V. (1990). The time-averaged paleomagnetic field. *Reviews of Geophysics*, **28**, 71–96.

108 Schrefl, T. (1999). Finite elements in numerical micromagnetics Part I: granular hard magnets. *J. Magn. Magn. Mater.*, **207**, 45–65.

109 Shcherbakov, V. P. and Shcherbakova, V. V. (1977). Calculation of thermoremanence and ideal magnetization of an ensemble of interacting single-domain grains. *Izv. Earth Phys.*, **13**, 413–421.

110 Shcherbakov, V. P. and Shcherbakova, V. V. (1987). On the physics of post-depositional remanent magnetization. *Phys. Earth Planet. Inter.*, **46**, 64–70.

111 Shcherbakov, V. P., Winklhofer, M., Hanzlik, M., and Petersen, N. (1997). Elastic stability of chains of magnetosomes in magnetotactic bacteria. *Eur. Biophys. J.*, **26**, 319–326.

112 Stacey, F. D. (1961). Theory of the magnetic properties of igneous rocks in alternating fields. *Phil. Mag.*, **6**, 1241–1260.

113 Stacey, F. D. (1972). On the role of brownian motion in the control of detrital remanent magnetization in sediments. *Pure and Applied Geophysics*, **98**, 139–145. IRM library.

114 Stacey, F. D. and Banerjee, S. K. (1974). *The physical principles of rock magnetism*. Elsevier, Amsterdam.

115 Tadmor, R. (2001). The London-van der Waals interaction energy between objects of various geometries. *Journal of Physics: Condensed Matter*, **13**, 195–202.

116 Tauxe, L. (1993). Sedimentary records of relative paleointensity: theory and practice. *Rev. Geophys.*, **31**, 319–354. IRMQ3.2.

117 Tauxe, L. (2005). Inclination flattening and the geocentric axial dipole hypothesis. *Earth and Planetary Science Letters*. in press.

118 Tauxe, L. and Kent, D. V. (1984). Properties of detrital remanence carried by hematite from study of modern river deposits and laboratory redeposition experiments. *Geophysical Journal of the Royal Astronomical Society*, **77**, 543–561.

119 Tauxe, L. and Kent, D. V. (2004). *Timescales of the Paleomagnetic Field*, chapter A simplified statistical model for the geomagnetic field and the detection of shallow bias in paleomagnetic inclinations: was the ancient magnetic field dipolar?, pages 101–115. American Geophysical Union.

120 Tauxe, L., Herbert, T., Shackleton, N. J., and Kok, Y. S. (1996). Astronomical calibrationi of the matuyama-brunhes boundary: Consequences for magnetic remanence acquisition in marine carbonates and the asian loess sequences. *Earth and Planetary Science Letters*, **140**, 133–146.

121 Tauxe, L., Bertram, H. N., and Seberino, C. (2002). Physical interpretation of hysteresis loops: Micromagnetic modeling of fine particle magnetite. *Geochemistry Geophysics Geosystems*, **3**, art. no.–1055.

122 Thomas-Keprta, K. L., Bazylinski, D. A., Kirschvink, J. L., Clemett, S. J., McKay, D. S., Wentworth, S. J., Vali, H., Gibson, E. K., J., and Romanek, C. S. (2000). Elongated prismatic magnetite crystals in ALH 84001 carbonate globules: potential martian magnetofossils. *Geochim. Cosmochim. Acta*, **64**(23), 4049–4081.

123 Truckenbrodt, E. (1980). *Fluidmechanik*, volume 1. Springer Verlag.

124 Vali, H., Förster, O., Amarantidis, G., and Petersen, N. (1987). Magnetotactic bacteria and their magnetofossils in sediments. *Earth Planet. Sci. Lett.*, **86**, 389–400.

125 van der Voo, R. and Torsvik, T. H. (2001). Evidence for late paleozoic and mesozoic nondipole fields provides an explaination for the pangea reconstruction problems. *Earth and Planetary Science Letters*, **187**, 71–81.

126 van Vreumingen, M. J. (1993a). The influence of salinity and flocculation upon the acquisition of remanent magnetisation in some artifical sediments. *Geophysical Journal International*, **114**, 607–614.

127 van Vreumingen, M. J. (1993b). The magnetization intensityof some artificial suspension while flocculating in a magnetic field. *Geophysical Journal International*, **114**, 601–606.

128 Verosub, K. (1977). Depositional and postdepositional processes in the magnetization of sediments. *Reviews of Geophysics and Space Physics*, **15**, 129–143.

129 Wagner, M. (1977). *Elemente der Theoretischen Physik 2, Felder und Wellen, Klassische und statistische Thermodynamik*. Rohwolt Taschenbuch Verlag GmbH.

130 Wartel, S., Singh, S. P., and Faas, R. W. (1991). The nature and significance of gas-generated microvoids as secondary microfabric features in modern and pleistocene marine and estuarine sediments. In *Microstructure of Fine-Grained Sediments, From Mud to Shale*.

131 Williams, W. and Dunlop, D. J. (1989). Three-dimensional micromagnetic modelling of ferromagnetic domain structure. *Nature*, **337**, 634–637.

132 Williams, W. and Wright, T. M. (1998). High-resolution micromagnetic models of fine grains of magnetite. *J. Geophys. Res.*, **103**(B12), 30537–30550.

133 Winklhofer, M., Fabian, K., and Heider, F. (1997). Magnetic blocking temperature of magnetite calculated with a three-dimensional micromagnetic model. *J. Geophys. Res.*, **102**, 22695–22709.

134 Witt, A., Heslop, D., von Dobeneck, T., Huhn, K., and Fabian, K. (2005). Discrete element modelling of post-depositional remanent magnetization acquisition in aquatic sediments. *Geophysical Journal International (submitted)*.

135 Wright, T., Williams, W., and Dunlop, D. (1997). An improved algorithm for micromagnetics. *J. Geophys. Res.*, **102**(B6), 12085–12094.

136 Wu, R. and Lee, D. (2001). Hydrodynamic drag on non-spherical floc and free-settling test. *Water Research*, **35**(13), 3226–3234.

137 Yang, R. Y. and Yu, A. B. (2003). Effect of material properties on the packing of fine particles. *Journal of applied physics*, **94**(5), 3025–3033.

138 Yang, R. Y., Zou, R. P., and Yu, A. B. (2000). Computer simulation of the packing of fine particles. *Physical Review E*, **62**(3), 3900–3908.

139 Yoshida, S. and Katsura, I. (1985). Characterization of fine magnetic grains in sediment by the suspension method.